Development of a Dynamic Snowmobile Model for Ride Dynamic Analysis

Paul-André Hébert

A Thesis
in
The Department
of
Mechanical Engineering

Presented in Partial Fulfillment of the Requirements
for the Degree of Master of Applied Science at
Concordia University
Montreal, Quebec, Canada

August 2006

Your file Votre référence
ISBN: 978-0-494-20820-5
Our file Notre référence
ISBN: 978-0-494-20820-5

ABSTRACT

Development of a Dynamic Snowmobile Model for Ride Dynamic Analysis

Paul-André Hébert

Owing to the high magnitudes of vibration transmitted to the snowmobile driver, ride comfort forms a major design requirement. Current development processes are based upon prototyping and sequential field-testing. An analytical model for investigating the dynamic snowmobile behaviour would enhance the designers' efficiency at achieving the desired ride performance. In this respect, only limited efforts have been made thus far. This dissertation research aims at developing a comprehensive, industry-viable ride dynamic model of the snowmobile to help in vehicle development.

A nine degrees-of-freedom model was implemented in the ADAMS software through the integration of nonlinear subsystem models, namely, a lumped frame model, detailed suspension representations, a track model, deformable ground model, trail surface representations, a quasi-steady traction model, and a simplified rider and seat model. Four different trails were measured and analyzed, characterizing their roughness in terms of spatial power spectral density. A field test program, undertaken with Bombardier Recreational Products Inc., provided the vehicle response data. Laboratory measurements were performed to obtain static and dynamic properties of the vehicle and its components. The measurements were compared to the model outputs to evaluate its validity, revealing reasonably good agreements for some of the trails, while considerable differences were observed for others.

The model was then used to perform a parametric analysis on nine ride-related factors. Following the response surface methodology, with seat surface vertical rms acceleration as response variable, lead to the identification of a range of parameter values reducing acceleration by 58%. The process revealed, among else, the model's high sensitivity.

Acknowledgements

The author wishes to express his sincere appreciation to his thesis supervisor Dr. Subhash Rakheja and industrial coordinator René Lemieux for their guidance and timely advice throughout the realization of the project summarized in this thesis.

Thanks are also due to Steve Langlais, snowmobile project leader at Bombardier Recreational Products Inc. (BRP), for accepting to fund the project and for supporting it throughout its many challenging phases.

Special thanks are due to Dr. Marc J. Richard, the author's co-supervisor, and to Bertrand Malette and Sébastien Thibault, engineers at BRP, for sharing their experience and acute insight when facing tough technical problems.

The financial support provided by the Natural Sciences and Engineering Research Council of Canada (NSERC) is also gratefully acknowledged.

This thesis is dedicated to the author's mother and brother for their indefectible support and understanding throughout the course of this project.

Table of Contents

LIST OF FIGURES

LIST OF TABLES

NOMENCLATURE

a	Horizontal distance from ski pivot to CM (mm)
$\overline{a}_w$	Frequency-weighted rms acceleration value (m/s^2)
A_{xl}	Acceleration of the frame CM along its local X axis (m/s^2)
A_{zl}	Acceleration of the frame CM along its local Z axis (m/s^2)
A_{zs}	Acceleration of the seat surface along the frame local Z axis (m/s^2)
$\overline{A}_{Zb}$	rms vertical acceleration at the driver's buttock
D_{cs}	Center spring compression (m)
D_{ct}	Center damper curve scaling
D_f	Front dampers curve scaling
D_{frail}	Friction drag generated at the track to guiding rail interface (N)
D_l	Ski leg displacement (m)
D_{ll}	Left front spring compression (m)
D_{lr}	Right front spring compression (m)
D_p	Displacement of the rear pivot arm head (m)
D_r	Rail bounce displacement relative to frame (m)
D_r	Rear damper curve scaling
D_s	Seat surface vertical displacement relative to frame (m)
D_s	Seat damping curve scaling
F_{lon}	Longitudinal propulsive force generated by the track (N)
K_{ct}	Central coil-over-shock unit stiffness curve scaling
K_f	Front coil-over-shock unit stiffness curve scaling
K_r	Rear suspension stiffness curve scaling
K_s	Seat stiffness curve scaling

I_i	Polar mass moment of inertia of track guiding wheel *i* (kg*m^2)
L	Track perimeter length (m)
N_{dIJ}	Reaction force component *I* at wheel *J* due to transient track tension variations (N)
N_{sI}	Reaction force component at wheel *I* due to the track static tension (N)
r_i	Radius of track guiding wheel *i* (m)
S_Z	Power spectral density of trail profile as a function (m^2/cycle/m)
TA, TB…TH	Instantaneous value of track tension at track segment corner points A,B, …, H (N)
th	Track belt thickness (m)
V_{xl}	Velocity of the frame CM along its local longitudinal axis (m/s)
V_{zl}	Velocity of the frame CM along its local vertical axis (m/s)
X_i,X_g	X coordinate of frame CM relative to the ground inertial reference frame (m)
Z_i,Z_g	Z coordinate of frame center of mass relative to the ground inertial reference frame (m)
γ	Track longitudinal slip ratio
ϕ_b	Drive axle angular rotation angle relative to frame (rad)
ϕ_c	Chassis pitch angle relative to an inertial reference frame (rad)
ϕ_{pb}	Drive axle angular velocity (rad/s)
ϕ_{pc}	Frame pitch velocity (rad/s)
ϕ_s	Ski pitch angle around its revolute joint on the ski leg (rad)
ϕ_r	Rail pitch angle relative frame (rad)
Ω	Spatial frequency (cycle/m)
θ_i	Track wrapping angle around a guiding wheel *i* (rad)
ρ	Track belt linear density (kg/m)

τ_b	Drive axle torque (Nm)

CHAPTER 1

INTRODUCTION AND LITERATURE REVIEW

1.1 Introduction

Snowmobiles are used first and foremost for recreational purposes, and are invariably driven on a variety of trails. The vehicle's interactions with relatively rough snow or ice-covered surface cause comprehensive magnitudes of whole-body type low frequency vibration transmitted to the driver. Although the riders are exposed to such vibration for less than an hour to a few hours on a given day, the driving comfort performance is among the leading criterion of most snowmobile buyers. The assessment of vibration-related discomfort and subsequent enhancement of the performance thus form high priority tasks for the snowmobile manufacturers. The perception of ride comfort, however, is influenced by a large number of factors in a highly complex manner. These include the environmental conditions, like freezing from cold weather and poor visibility, while others are directly related to the design and dynamic performance of snowmobile, such as sound level, seating position and, most of all, the nature of shock and vibration transmitted to the rider through the seat. The particular driver's sensitivity, mood, and personal preferences can also influence the perceived comfort. The development of reliable metrics of comfort performance is thus a highly complex task.

Snowmobile riders are exposed to relatively high levels of whole-body vibration and shock along the longitudinal, lateral and vertical directions [1]. The crest factors of transmitted vibrations can exceed 9, suggesting high shock content. A subjective and objective study of 11 snowmobile drivers over a period of ten years concluded that more

than half of the drivers had back pains. Only a few of them, however, considered shock and vibration as the causal factor. Even so, the objective measurements revealed extremely high values of frequency-weighted rms acceleration, ranging from 1 to 6.1 m/s^2 [2]. Another study in Finland has shown excessive levels of vibration transmitted to the operator's hands through the handle bars [3]. Among the 334 snowmobile drivers considered in the study, 18% reported experiences of white finger attacks and 48% reported numbness of the hands. These studies have suggested control of transmitted vibration through improved engine mounts, steering yoke design and suspension system.

Although considerable efforts have been devoted to snowmobile ride improvement, the assessments and design improvements largely rely upon subjective, iterative and extensive field tests. While the subjective and field evaluations yield vital information for the development process, the simulation-based design methods are desirable as is the case in the automobile industry [4]. These techniques, however, have resulted in noticeable paradigm shift in the snowmobile architecture, as it is evident from the designs initiated by Bombardier Recreational Products (BRP), such as the release of the REV platform in 2002. Its major novelty is that the driver sits closer to the center of gravity (CG) in a more upright position, judged to be more comfortable over rough trails. The simulation tools could effectively complement the conventional design process and improve the consistency and reliability of the end product dynamic behaviour. The simulation tools would also allow for detailed quantitative investigations into the influences of various subsystems and their interactions, while reducing the efforts in developing prototypes and repetitive trials. Eventually, the use of virtual development

tools could result in reductions in the product development time and cost by requiring fewer physical prototypes and measurements [4].

Over the past few years, the applications of several technologies, formerly reserved for research and long time-to-market high-end applications, have grown and become more widely available. Following the author's suggestion, BRP recognized the potential of two such technologies to develop new ride design and calibration tools. The first technology involved the use of magneto-rheological (MR) semi-active suspension to improve vibration attenuation and handling. The second initiative involved the development of a multi-body dynamic model of a snowmobile to serve as a tool for quantitative evaluation of the dynamic behaviour. The tool could also be used for evaluating different control algorithms for the semi-active suspension. More importantly, it would be the first step toward the integration of simulation tools in the snowmobile ride and handling design process. The model tuning would involve characterization of trail roughness and analyses of traction forces developed by the track as well as the ride vibrations.

During the course of the project, it became obvious that the MR dampers, selected primarily for their commercial availability could not be suitably modified for the typical piston velocity range encountered in snowmobiles. Considering the suppliers inability to create dedicated dampers in the available time frame, the entire project was re-focused on the development and validation of a comprehensive in-plane simulation model of a snowmobile, used initially to perform a parametric study on the factors believed to have the greatest influences on the ride comfort.

Thus, the scope of the dissertation research was formulated to analyze the in-plane dynamic behaviour of a snowmobile through multi-body modelling and analyses. A comprehensive 8 degrees of freedom (DOF) model of a BRP MX-Z snowmobile is hence developed. A 1 DOF driver model is also included. The model is formulated and implemented in the ADAMS® (Automatic Dynamic Analysis of Mechanical Systems) platform. Different snowmobile trail profiles are characterized using data from a dedicated field measurement campaign, which also provided the baseline snowmobile behaviour used for model calibration and validation. A simple and efficient track model, reproducing the coupling effect between the applied torque and the rear suspension compression, is derived. Based on the measured data, a quasi-static empirical relation is developed for the longitudinal track force. The simulation results from the various trail profiles are validated using the measured data. A parametric study is then performed to investigate the influences of several suspension parameters on the ride dynamics of the vehicle. For each of the aforementioned major phases of the project, a review of literature was conducted to identify the accepted practice and the associated methods.

1.2 Literature Review

The reported studies on the dynamic analyses of snowmobiles, off-road terrain properties, track and suspension dynamics, and ride comfort are thoroughly reviewed to formulate the scope of the dissertation research and build the essential knowledge on analyses methods. In view of the scarcity of published studies specifically devoted to snowmobiles, the review is extended to tracked vehicles and off-road terrains in-general, which exhibit important similarities with the snowmobiles. The following sections present a brief summary of the state-of-the-art on each relevant subject.

1.2.1 Vehicle Models

The first reported mathematical modeling of a snowmobile is due to Newman et al in 1972 [5]. On the basis of the observed behaviour of a snowmobile suspension and track using high-speed cameras [6], the authors implemented a pitch and bounce plane model of the frame on a hybrid computer, assuming constant forward speed. The two skis, supported by leaf springs, were treated as a single unit, consisting of a linear vertical spring and viscous damping connecting the frame to the undeformable sinusoidal ground profile. The same model was applied to each of the three truck assemblies forming the rear suspension (Figure 1.1). The track was assumed to be perfectly flexible based of the filmed behaviour and was thus excluded from the model. The provision for skis or trucks leaving ground (loss of contact) or bottoming were included through logic circuitry. Additional circuitry enabled the graphical display of the dynamic behaviour on an oscilloscope. Although the results were believed to be reasonable, no attempt was made

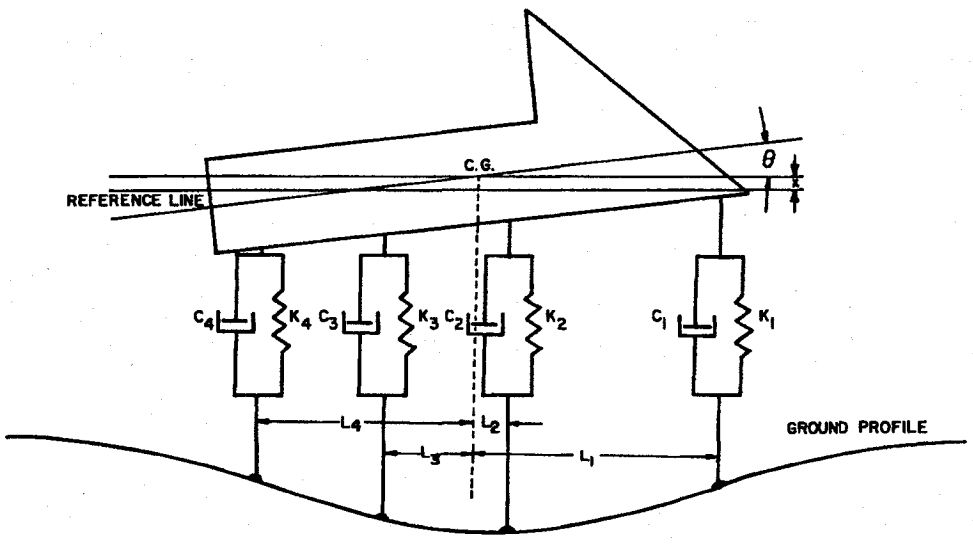

Figure 1.1: The first snowmobile model, developed by Newman et al [5].

to demonstrate their validity against field measurements. One important downside of this model was that any modification to the model topology required a physical rebuilding of the analog circuit performing the actual dynamic simulation.

A large number of studies on various aspects of the snowmobiles were conducted during the seventies and eighties. These included the studies on transmission [7], tracks [8], braking [9], ski suspensions [10], dampers [11] and numerous others about noise emission and motoring safety. It wasn't until 1989 that another study on the simulation of a snowmobile dynamics was published. It presented a multi-body dynamics simulation program incorporating the suspension dynamics [12,13]. The suspension system was characterized by its non-linear force-deflection properties rather than the rigid of flexible bodies to enhance the computational efficiency. For the same reason, the ground was considered rigid, and the skis and track guide rail were represented as straight line segments, which remained in contact with the ground at all times. The path of the ski pivot and those of the rail's two pivots were computed using a kinematic preprocessor. Thus, the forces acting on the chassis-driver subsystem, modeled as a single rigid body, were derived from the relative motion between the chassis and the ground contact points used as inputs to the suspension force-deflection models. The inertial forces due to the entire suspension system were thus neglected in this 2-DOF model. Constant velocity simulation of the passing of a single bump showed good correlation with the test data at a low speed, while the simulation program could not reproduce the loss of contact with ground that occurred at speeds above 30 km/h.

In the early nineties, a more comprehensive multi-body dynamic model of the snowmobile was attempted [14]. This 6-DOF model included 3 rigid bodies, and the

equations of motion were developed based on Kane's formalism. This model permitted computation of the contact forces between the trail profile and the ski and rail through the use of a deformable-ground model. That characteristic allowed the simulation of dynamic responses under moderately high constant speeds, where frequent loss of contact would occur. This model, however, did not include a track model, aerodynamic drag and ground friction. Consequently, it could not reproduce the coupling between the drive-axle torque and the rear suspension compression. Although the passing of a bump was simulated at three different constant speeds, the validity of the results was not demonstrated while the acceleration or deceleration response could not be analyzed most likely due to the lack of the drive torque to rear suspension coupling.

Even though there are no other published studies on the subject of snowmobile dynamics, there has been at least one other effort on the snowmobile modeling. The now defunct Scorpion Recreational Products company of Wisconsin used the Working Model 3D software in the late nineties to simulate various events, such as responses under a vertical drop on a rigid ground [15].

As stated earlier, the dynamic response of other types of tracked vehicle have been studied extensively over the last fifty years. Most of these studies concentrated on heavy vehicles used either for industrial or combat applications. These typically have a much lower power to weight ratio and experience longitudinal accelerations significantly lower than those found in recreational snowmobiles. Using skis and a single rigid rail to guide its track, the snowmobile suspension mechanism is considerably different from that of most other tracked vehicles, which employ several road-wheels, more or less independently sprung, and no skis. Some aspects of the modeling techniques developed

for these vehicles, however, are applicable to snowmobiles. The following sections thus present a brief review of the relevant studies on track-terrain interactions, track modeling and ride comfort assessment with an emphasis toward off-road applications. This constitutes in no means an exhaustive review of the developments n general tracked vehicle models, which can be found in Dhir [16] and Sandu [17] among others.

1.2.2 Terrain properties

Physical properties of soft terrains directly affect their capacity to support the weight and traction force of a vehicle. They also influence the magnitude and type of terrain profile and deformations due to vehicle passage. The softer the terrain, the larger these effects would be. The snow, ice or mixture of the two would mostly represent a soft terrain, which may undergo compaction and shearing. Only a few studies have attempted to characterize the profiles and compaction resistance of snow covered terrains, while a number of studies have focused on the characterization of soft soils.

Although studies on soil penetration tests and measurements of consistency have been performed as early as 1913, a systematic soil trafficability test method was not developed until the World War II. The test method, developed by the Waterways Experiment Station (WES) of the U.S. Army Corps of Engineers, was strictly a "go" or "no go" evaluation technique that was used to plan vehicles deployment. In the fifties, the U.S. Army Tank Automotive Command's Land Locomotion Laboratory, headed by M.G. Bekker, developed the bevameter, an instrument for measuring the compressive and shear stress-strain characteristics of the terrains [18]. It is composed of two devices, where the first device was used to force a pressure plate vertically into the ground surface, and

thereby recording the pressure-sinkage relationship for the soil. The second device employed a shear plate (with grousers) applied on the terrain and forcing it to shear the ground surface while recording the shear force-horizontal displacement curve. Bekker [18] extensively used the bevameter and established empirical relations for both the pressure-sinkage and shear force-shear displacement properties of the different soils. Subsequent refinements of these relations, by different researchers, resulted in relationships that have been used over the last twenty years to study the mobility characteristics of vehicles over soft terrains [19,20]:

The pressure-sinkage relationship for mineral soils is generally given by the Reece equation [20]:

$$p = (ck_c' + \gamma b k_\phi')(z/b)^n \tag{1.1}$$

where p is the normal pressure acting on the ground surface, b is the radius of the circular pressure plate or the smaller dimension of a rectangular plate, z is sinkage of the plate in the ground, c is the cohesion coefficient of the soil, γ is the weight density, and n, k_c' and k_ϕ' are constants identified from the measured data using a least-square error minimization technique.

The shear force-displacement relationship for plastic soils is defined using the Janosi and Hanamoto [20] formulation:

$$s/s_{\max} = 1 - \exp(-j/K) \tag{1.2}$$

where s and s_{max} are the shear stress and maximum shear stress, respectively, j is the displacement, and K is the shear-deformation modulus, a measure of the magnitude of the shear displacement required for the development of the maximum shear stress.

The Reece equation is considered valid for mineral soils, with a grained structure of varying grain size. The Janosi equation, on the other hand, is applicable for terrains displaying a "plastic", as opposed to "brittle" or "elastic", shear behavior. These equations have habitually been used to characterize fresh snow covers, in the absence of ice layers or crusts formations [20,18]. Several other relations have also been proposed to model the behavior of different terrain covers such as muskeg, crusted snow [20] and very soft, high water content mineral soils of coastal shores [17].

The aforementioned researchers also investigated the effects of repetitive loading on track-ground pressure and sinkage. Under the passage of a tracked vehicle having n road wheels, a given terrain segment is typically submitted to n loading-unloading cycles. This yields compaction of the soil and thus influences the normal pressure distribution and the total tractive capacity. Most soft terrains exhibit plastic deformations; each loading cycle increases the sinkage, which directly affects the attitude (pitch) of the chassis. Terrain response to repetitive loading is thus an important factor to consider for the studies in traction and dynamic behaviour of the tracked vehicles [19].

In this regard, a snowmobile constitutes a unique type of tracked vehicle since a given segment of the terrain is loaded and unloaded only once, when the vehicle travels over it. This is due to the fact that the track lies between the skis and is vertically loaded by a single rigid guide rail assembly instead of the multiple independently sprung road-wheels used in typical tracked vehicles. Consequently, the terrain response to repetitive loading could be neglected in snowmobile modelling.

Apart from soil deformation under load, the surface profile of the terrain forms a vital component for the ride vibration response analyses of the vehicle. It constitutes the

major source of excitation for the vehicle ride motion, apart from the inertial forces arising from the driver induced accelerations, and aerodynamic forces and moments.

Bekker [18] recounts that, as was the case for soil load-deformation quantification, the first profile measurements were aimed at determining whether or not vehicles could travel over a given area, based on the relative position, form and occurrence of the surface obstacles it contained. These measurements were mostly performed using the standard land surveying equipment. In the early to mid-sixties, the surface roughness measurements were performed with sufficient resolution to investigate the vehicle vibration and influences of vehicle speed [18]. Although an extensive profiling effort was conducted by the US Army using standard surveying equipment [21], the techniques quickly evolved from rod and level to vehicle-mounted instrumentation with various types of profile height sensing devices. One early such vehicle, from General Motors Corporation, used a small free rolling wheel following the ground surface profile while supporting a mass via a spring as shown in Figure 1.2 [18]. The mass vertical acceleration and distance from the wheel (spring deflection) were measured and used to compute the actual ground profile through integration and summation. Another vehicle, from the U.S. Army's Land Locomotion Laboratory, was intended for off-road applications and towed a two-wheel cart, while its absolute pitch orientation was recorded, using a gyroscope, as a function of the distance travelled [18]. The profile was then computed using the absolute orientation to project the instantaneous distance increment on an earth fixed frame of reference.

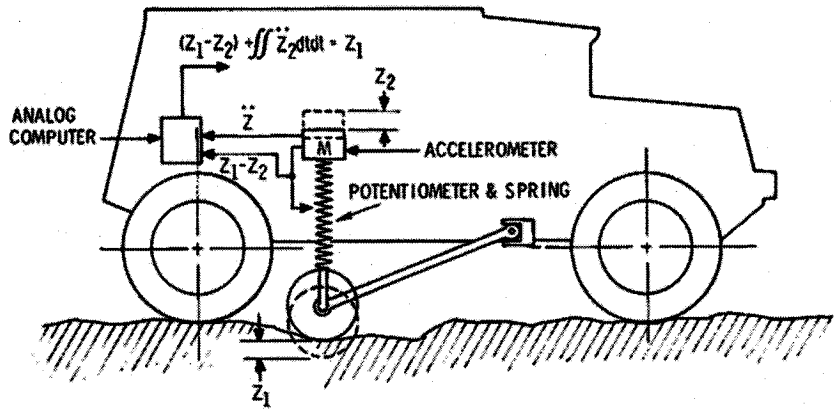

Figure 1.2: General Motors early ground surface profilometer [18].

The surface profile obtained from these vehicles represented very large quantities of data in a form almost unusable for quick and efficient comparisons of different terrain types. Conversion of the elevation signal to its frequency domain equivalent provided a suitable synthesized form, which was rapidly accepted as a standard method for presenting the terrain surface roughness [18]. The road and off-road surface profiles have thus been commonly characterized in terms of the spatial power spectral density (PSD) of the filtered elevation as a function of the spatial frequency or the wavelength [20]. This allows for deriving the temporal roughness, velocity and acceleration from PSD as a function of the vehicle speed.

Although the first instrumented vehicles accelerated the profiling operations compared to the manual surveying methods, the accuracy of the measurement could not be assured while driving at high speeds due to contributions of the vehicle dynamics and inertial effects.

Mimuro et al. [22], of Mitsubishi Motors Corporation, developed a high-speed road profiling vehicle using optical measurement systems. It employs four laser vertical displacement sensors and an optical non-contact speed sensor for accurate measurements

of elevations at speeds up to 200 km/h. The displacement signals are treated as four groups of three signals. The resulting four displacement signals were individually converted to the frequency domain before applying the frequency weighing and phase shifts. The treated signals were then combined to produce the final output signal, which is converted back to the time domain and subsequently to the spatial domain, yielding the ground profile reconstitution. A noticeable feature of this method is that the combination process eliminates the need to monitor chassis ride and pitch, their effects being perfectly negligible on the final output.

Most off-road terrains are considered deformable to some extent when subject to the vehicle passage. Moreover, several terrain types can partly regain their shape after the load removal owing to their elasticity [20]. The characterizations of surface profiles of soft terrains thus pose considerable challenges, since the actual surface profile exciting the vehicle is neither that existing prior to vehicle passage nor that observed after the passage.

Laib [23] investigated this phenomenon for vehicle rolling on tires and described the profiles as natural, effective and deformed to designate the surface profiles prior, during and after vehicle passage, respectively. The effective profile was derived from the measured natural and deformed profiles together with the vertical acceleration of the axle and the vehicle vertical transfer function. A comparison of the elevation PSD of the three profiles obtained from various terrains revealed that the effective profile falls between the natural and deformed profiles, while the natural profile showed highest PSD of the three, confirming that vehicle passage typically has a smoothing effect on the surface roughness.

Recognizing the need for efficient measurements of the effective profiles of roads/terrains, Ashmore and Hodges [24], of the Nevada Automotive Test Center, developed another profiling technique. The profilometer vehicle is based on a standard four-wheel-drive vehicle equipped with live axle suspensions. At each of the four axle ends, the wheel velocity and vertical acceleration were measured using an optical encoder, and an accelerometer, respectively, while a load cell machined within the axle measured the vertical force supported by the hub carrier. Laboratory tests provided the data on the tire's vertical stiffness and damping, and the effective mass attached to the load cell (hub, brake, wheel, tire, etc.) The assembly was thus treated as a single DOF system illustrated in Figure 1.3 with "effective" ground profile (x) being the only unknown. The wheel center displacement (y) was computed through double integration of the accelerometer signal. The system's single equation was then solved, in the frequency domain, for the ground profile. The computed profile was considered valid as long as the tire maintained contact with the ground, which imposed a limit on the maximum vehicle velocity.

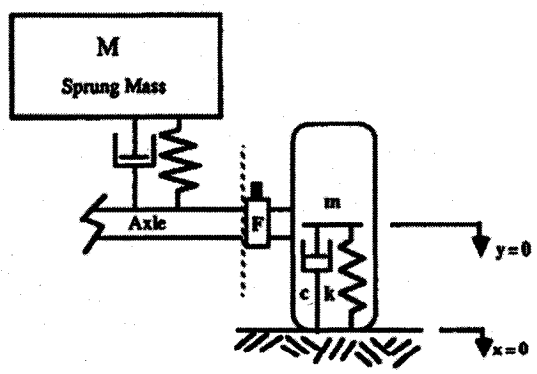

Figure 1.3: Axle end treated as a single spring-mass-damper system [24].

While the above reported systems have been widely applied for characterizing the surface profiles of roads and off-road terrains, only minimal efforts have been made to measure the surface profiles of snow-covered terrains [20].

1.2.3 Track Model

As described earlier, only a few studies on dynamic modelling of snowmobiles have been reported. These models, however, do not incorporate a track model and thus do not permit for analysis of traction properties and do not take into account the coupling between the drive torque and rear suspension compression. The reported studies on track vehicles employed in the military and service sectors have concluded that the addition of the track adversely affects the ride quality [25, 16].

Conceptually, the simplest way to represent a track is probably to model it as a chain of rigid links. In such a multi-body system approach each track link is treated as an independent rigid body with a revolute joint at each end to form a closed loop kinematic chain [26]. Such a model is able to reproduce the various vibration modes of the track, particularly along the direction normal to the motion path. However, the whole system modelling complexity increases greatly since each link adds 6 free body equations of motion, 2 constraint equations and at least as many contact force equations as there are track guiding wheels. Using this approach, Shabana [26] developed an in-plane model on an excavator track as shown in Figure 1.4. Excluding the track, the model comprised 12 bodies (ground, chassis, sprocket, idler, seven road wheels and one upper roller), and forty-two track links are added along with the required constraint and contact equations. A continuous or piecewise continuous track model may be considered adequate when

only low frequency dynamics is concerned as in the case of handling dynamics and dominant ride responses. Moreover, modern tracks employed in lighter vehicles are a continuous elastic belt, which do not require the consideration of excessive number of links.

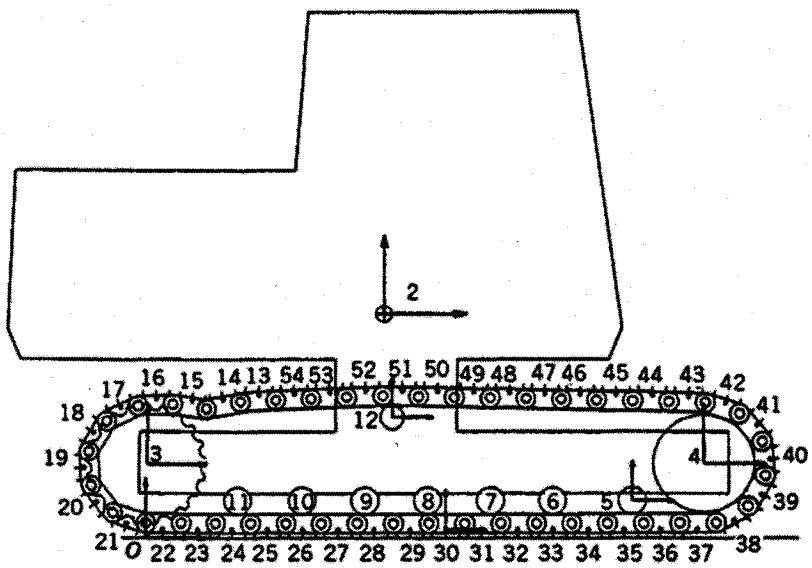

Figure 1.4: Multi-body model of an excavator running gear [26].

Dhir [16] investigated four different track models with a special focus on keeping the computing effort low while neglecting the track vibration modes. The models incorporated the kinematic constraining effects of the track. The first model, strictly kinematic, can be described as a massless continuous elastic belt, transmitting only tensile forces. Two tension components were summed to approximate the overall track tension assumed to be constant over the entire track loop. These included the initial pre-tension and the global overall tension that increased due to track stretching. The second track model included the track sag between the drive sprocket and the idler using a quadratic polynomial approximation of the catenary equation. The pretension due to the sagging effect was inversely related to the amount of slack in the upper track strand. The

model thus permitted for variations in the pretension due to upper track strand length, which was expressed as a function of the track bridging effect on ground. A third model used the ideal catenary equation to model the track sag, which provided results similar to those of the second model. The three models were applied for ride analyses at constant forward speeds and did not include the track rotational degree of freedom. Dhir [16] also proposed a fourth model incorporating the local track tensioning effects instead of the overall track tension. The local tension effects were assumed to be proportional to the relative vertical displacement of the two adjacent wheels but not related to track bridging effect. None of these models considered shear forces between the track and ground assuming their negligible effects for a vehicle traveling on a relatively horizontal ground at constant forward speed.

Ma and Perkins [27] proposed a model based on the equilibrium of an infinitesimal track element for analyzing the vehicle responses under a constant forward speed. A finite element formulation, based on the equilibrium equations of the elastic track element, was developed using the reported normal and shear force constitutive laws to model the track-ground interactions. Tension as well as normal pressure arising from ground and wheel contact, and shear force were computed for each track element. One element per track link could thus be used to represent a rigid link track, while several times more elements would be required to represent a flexible track. The formulation, however, considered the normal pressure as well as the shear stress over the entire loop, even between the wheels, while being far simpler than a full multi-body model.

Sandu [17] used the above methodology but treated the track as a combination number of many complete segments rather than a continuous belt of infinitesimal

elements, which enhanced the computational efficiency. The entire system was again assumed to be in a quasi-steady state, where the longitudinal velocity was held constant. The arc formed by the track around each wheel, limited by the point where track initiates contact with the wheel and the point where it leaves the wheel, was treated as a balanced segment. Similarly, the track section in between the two wheels was also treated as a balanced segment, as seen in Figure 1.5.

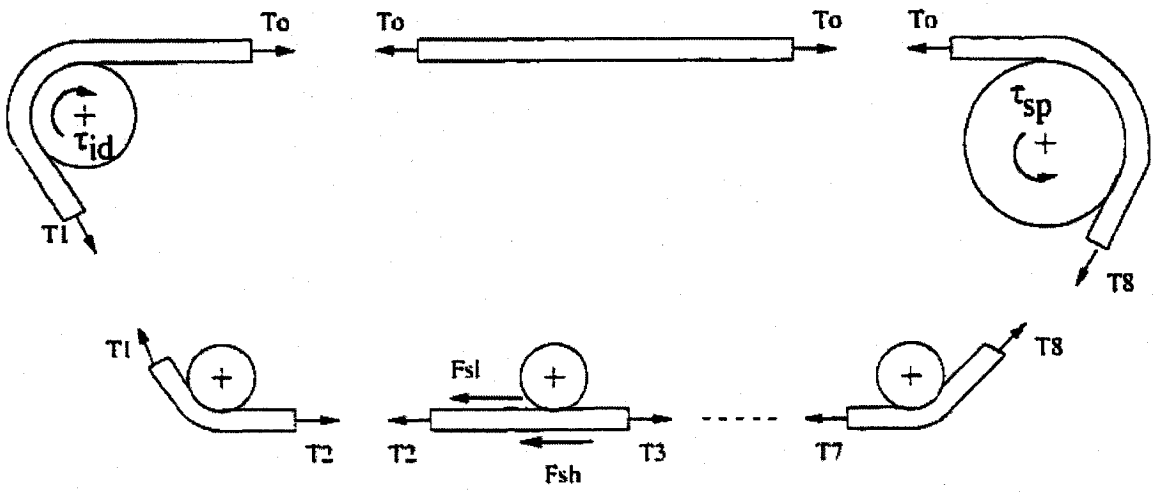

Figure 1.5: Track modeled as balanced segments [17].

The static equilibrium equations generally take into account the track segment weight and external forces, such as track tension, wheel normal reaction and friction force, and the ground normal and shear reaction forces. The inertial forces due to centripetal acceleration, however, were ignored event though they may approach values several times higher than the weight, particularly around the sprocket and the idler. The effects of the track on the vehicle are habitually modeled through applications of the track resultant forces and moments on each road-wheel, sprocket, idler and the roller. The track tension typically decreases with each subsequent segment, being maximal at the sprocket "entry point". Finite longitudinal track stiffness is also generally included in the track tension

computation [27, 17]. A no-slip condition is further assumed between the track segments and the wheels. Such a modelling approach requires only one equilibrium equation per segment and is therefore considered to have high computational efficiency.

1.2.4 Ride Comfort

Although the previously reviewed snowmobile models were intended for analysis of the ride behaviour, the ride dynamic responses and the comfort assessments have not been reported. A few research efforts related to snowmobile ride, however, have been attempted on the driver seat properties and performance. In 1973, Schanhals and Pershing [28] established a dynamic seat cushion performance criteria based on a spinal injury model developed by the US Air Force. The developed test method, resulting in a "pass" or "fail" rating for the tested seat cushion, and became the foundation for the SAE J89 standard – Performance Criteria for Snowmobile Seats [28]. In 1994, Anttonen and Niskanen [2] investigated whole-body vibration induced by 11 different snowmobiles as a possible cause of back pain injuries. Measurements revealed that the frequency-weighted rms acceleration at the seat-driver interface ranged from 1 to 6.1 m/s². According to ISO standard 2631-1, such values are capable of inducing injuries from repeated exposure. Ten years later, Rehn *et al* [1] recorded the three orthogonal components of acceleration at the driver-seat interface of 6 different snowmobiles used by Swedish professional workers in the course of their duty. Application of the ISO 2631-1 (1997) standardized treatment revealed that the frequency-weighted rms acceleration, with x and y components adjusted for sensitivity (relative to the z component) by multiplying them by 1.4, was on average slightly dominant along the longitudinal axis at 1.0 m/s². The crest factor metric exceeded 9 in several cases,

implying that shock and transient vibration effects are possibly important and need investigation. Vibration dose value (VDV) and maximum transient vibration value (MTVV) were found to be dominant along the z-axis at 7.6 $m/s^{-1.75}$ and 7.9 m/s^{-2} respectively. Following the European Union action values and ISO 2631-1 health guidance cautions, these vibration magnitudes are considered high and exposure should be limited to significantly less than 8 hours a day.

The ride properties of various road and off-road vehicles, however, have been studied extensively. These include subjective and objective assessments of ride comfort, and dynamic and field analyses. The subjective methods continue to be desirable ones for relative ride ranking of a group of vehicles or components, and for final tuning of a passenger vehicle ride characteristics prior to its commercial release [29]. Such evaluations are generally performed in the final development stage, when ride is already considered quite good. However, the objective methods are used earlier in the development process as well as for vehicles operating in extreme conditions (e.g. off-road). The international standard ISO 2631-1 (1997) [30] defines the currently recommended methods for whole-body vibration measurement in view of its effects on human health and comfort. The criteria are based on the level and frequency contents of the random vibration acceleration measured along the three orthogonal axes at the points of entry to the human body, which are the feet of a standing person, and the buttock, back and feet of a seated body. Frequency weighting functions are applied to the acceleration signals to account for the differences in the sensitivity of the human body to vibration over different frequencies. Different weighing functions are used for vibration along the different axes. The frequency range considered for evaluations related to health and

comfort is limited to 0.5 to 80 Hz. The basic vibration level metric is the frequency weighed root-mean-square (rms) acceleration value, defined as:

$$\bar{a}_w = \left[\frac{1}{T} \int_0^T a_w^2(t) dt \right]^{\frac{1}{2}} \tag{1.3}$$

where $\bar{a}_w$ is the rms acceleration, $a_w(t)$ is the frequency weighted acceleration and T is the measurement duration. In cases where the crest factor, defined as the ratio of the maximum instantaneous value of the weighted acceleration to its rms value, is greater than 9, the basic metric must be complemented with other assessment methods. When transients are present, the maximum transient vibration value (MTVV) is used to capture their influence. Similarly, the fourth power vibration dose value (VDV) is used to capture the influence of shocks.

There are three other major methods currently used for objective ride comfort evaluations [31]. British Standard BS 6841 [32], released in the late eighties, largely influenced the last revision of ISO 2631-1. It introduced the VDV method and extended the lower frequency limit to 0.5 Hz instead of 1Hz used in earlier version of the ISO-2631 [1974]. The frequency weighting functions are also slightly different than those applied in ISO 2631-1. VDI 2057 [33], developed in Germany in 1963, is the ancestor of all the ride quality standards. It is based on a calculated ride comfort index, designated as the *K-factor*, which is compared to a subjective table indicating the ride quality as perceived by the vibration-exposed humans. The last widely used ride assessment criterion is known as average absorbed power (AAP) and was developed by the US Army Tank Automotive Center (ATAC) [34]. When exposed to vibration, the human body behaves as a damped elastic system, thus dissipating (or "absorbing") the vibration

energy. The time rate of energy dissipation is referred to as absorbed power and its magnitude can be used as a ride quality metric.

In an extensive study using a landmine protected troop carrier vehicle travelling at two different constant speeds on four different terrain types, Els [31] compared the results of all four standards with the passenger's subjective evaluations. It was concluded that, for the vehicles and terrains studied, any standard could be used for ride assessment since they displayed similar levels of correlation with the passengers' perception of comfort. However, only the vertical direction should be used, the other directions revealed poor correlation with the passengers' comfort perception.

When trying to predict ride comfort through simulation, the model should not only correctly reproduce the vehicle behavior but also the seat-passenger system. Owing to the strong coupling between the polyurethane foam seat and the human body damped elastic behavior, the seat surface acceleration is strongly influenced by the human driver biodynamic behaviour [35]. Moreover, both foam and human body are very complex non-linear systems. Tang [35] extensively studied the problem and developed a model of the vertical behaviour of a car polyurethane foam seat. The model was validated using the experimental data, while four different human body models found in the literature where applied. A linear three DOF human body model was then tuned so that the response of the combined seat-human body model agreed well with the laboratory measurements, while that of the human-body model alone agreed with the measured biodynamic response of the subjects seated on a rigid platform. It was concluded that even this combined model was not valid over the whole range of excitation amplitudes, mostly due

to the non-linear biodynamics of the occupant. A valid seat-occupant model under large amplitude excitations, such as those found in snowmobiles, however, does not yet exist.

1.3 Scope of the Thesis

Virtual prototyping has the potential to open new investigations, analyses and design possibilities for the snowmobile design engineer, provided that an "industry viable" simulation model can be built. The snowmobile models developed thus far have not been accepted design tools due to their various limitations described in the previous section. For instance, the reported models have not attempted a track model to account for the track tension. Moreover, the models were too complex for analyses of design modification and hence could hardly be used to investigate alternate mechanisms. The models could only simulate a limited set of maneuvers, unless the user was able and willing to devote a significant programming effort to add functionalities, while a user friendly interface was not at all attempted. The simulation programs offered limited to inexistent flexibility of the output format and post-processing. Most of all, the validity of the models had not been demonstrated. The development of an alternate, more comprehensive model would provide definite advancements towards development of a design tool sought by the snowmobile manufacturers to support their current ride improvement efforts using the quantitative approach.

As evidenced in the literature review, the quality of the track-ground interaction representation is of utmost importance to the model validity. Ground deformation under load must consequently be modeled to reflect the experimentally observed behavior. The chosen representation must also be quick to computational in order to preserve the versatility and general applicability of the model for varying design tasks. Eventual

design work will also require a description of the range of trail profile roughness typically encountered. The measurement efforts for characterizing the roughness profiles of typical snowmobile trails are thus extremely important.

As stated in the literature, a typical tracked-vehicle ride response is adversely influenced by the track tension. Even greater effects are expected for the snowmobiles due to the coupling between the drive-axle torque and the rear suspension deflection, and higher track- to-vehicle weight ratio. The development and integration of a track model that incorporates the track weight, inertia, tension and coupling effect, is thus desirable.

The first intended application of the target snowmobile model concerns the analyses of influences of design and operating parameters on the ride behavior in general and driver comfort in particular. However, owing to the extreme complexities associated with interactions between the polyurethane foam seat and the human body, the development and integration of a validated seat-driver system in the snowmobile model goes beyond the scope of the present research work. A basic seat model and driver representation based of the available information, however, should be included to represent, as a minimum, the vertical degree of freedom of the driver relative to the frame.

The ride dynamic analysis of a snowmobile involves complex challenges attributed to track dynamics, characterization of the surface profile, track-terrain interaction, and track-suspension coupling, to name a few. The quality of the model is thus of utmost importance, which must be demonstrated for a range of operating condition. Unfortunately, the last snowmobile model developed, although being substantially detailed, has never been benchmarked against experimental data. This was

perhaps the major reason for lack of its exploitation by the sponsoring manufacturer. A thorough validation must therefore follow the modeling phase. Extensive measurements of the driver-snowmobile system dynamic behavior are thus required.

The model's potential for analysis and design has to be demonstrated to convince the future users of its benefits and encourage its adoption. A good way to accomplish this while documenting a first quantitative investigation of snowmobile ride comfort would be to perform a parametric analysis of the influence of chosen suspension parameters on the acceleration of the driver body along the vertical axis of the vehicle chassis. The ride quality assessments could be performed using the general recommendations of one of the ride quality assessment standards summarized in the previous section.

1.3.1 Objectives

The overall objective of this dissertation research is to encourage the adoption of quantitative methods for evaluation of the snowmobile dynamic behavior, and for design tasks, by the chassis engineers. An industry viable design and analysis tool based upon the comprehensive in-plane snowmobile ride simulation model is thus attempted. In order to eliminate the limitations of the previously developed models, the goal is here to develop a model including a representative but fast computing track model and ground contact algorithm as well as typical snowmobile trail profiles. These requirements, along with several others, translate in the following specific objectives:

a. Characterize the roughness properties of typical snowmobile trails by developing and implementing an appropriate measurement method.

b. Measure the dynamic behavior of a snowmobile in the field over various typical trails at different speeds.

c. Characterize the track traction potential in the form of a quasi-steady model of the longitudinal force versus the normal load and the slip ratio.

d. Develop an in-plane snowmobile model incorporating a track model, a quasi-static traction model based on the experimental measurements, a representation of the driver and a viable ski and track to ground interaction model, allowing efficient simulation of the steady state as well as transient manoeuvres.

e. Examine the validity of the snowmobile model against the experimental data.

f. Perform a parametric study on the effects of several suspension parameters on the seat surface acceleration, while travelling over typical medium roughness trail profiles.

1.3.2 Layout of the Thesis

In Chapter 2, the experimental protocol is presented along with the data analysis. A general description of the studied vehicle is given first, leading to the elaboration of the model architecture in terms of the required degrees of freedom to completely characterize the vehicle behaviour. A profiling method for snowmobile trails is also presented. The field measurement protocols and instrumentation are then described and sample results are presented for each type of tests, both in the time and the frequency domains, including the rebuilt ground profile and the extracted surface roughness PSD's.

In Chapter 3, the snowmobile model is described in details, beginning with the vehicle itself. The chassis and suspension rigid body subsystem is described first. A track model adapted to snowmobile characteristics is then developed through the empirical traction model based on the experimental data. A description of the basic human body model used to represent the driver ends the vehicle subsystems presentation. The second section of the chapter describes the snow trail representation in the multi-body model. A final section describes the general method of solving the equations of motion used in the ADAMS platform.

Model validation is presented in Chapter 4, which includes the static equilibrium and the dynamic response comparison. The frequency response characteristics of a simplified 2-DOF linear bounce and pitch model, equivalent to the full vehicle model around its operating point, are derived and compared to those of the full model responses, under low amplitude excitations and stabilized drive-axle input torque. The chassis movement and suspension deflection responses are compared with the measured data acquired for different trail profiles.

Chapter 5 presents the results attained from the parametric analysis meant to study the influences of several suspension parameters on the ride quality. In this regard, a performance criterion is formulated and discussed. The results are discussed in view of the desired design modifications for enhanced ride comfort.

Finally, Chapter 6 presents the major conclusions and recommendations for future work.

CHAPTER 2

EXPERIMENTAL METHODS AND DATA ANALYSIS

2.1 Introduction

The ride dynamic response of a vehicle can be effectively assessed through field measurements of transmitted vibration under representative operating conditions. A carefully designed experimental matrix, however, is needed to fully characterize the vehicle's ride dynamic behaviour. This is particularly important for the snowmobile considering the complex track-terrain and ski-terrain interactions and the coupling between the rear suspension deflection and the track tension. The measured data thus acquired is essential for verifying and tuning various aspects of the ride dynamic model.

In this chapter, a field experiment is designed to characterize the ride dynamic behaviour of the snowmobile over different selected terrain. The measured data are analyzed to derive the ride properties in terms of acceleration at the seat, suspension deflections, etc. The data are further used to examine the validity of the snowmobile model, as described in the following chapters.

2.2 Vehicle Description

The studied vehicle, hereafter designated as "candidate vehicle", is Bombardier Recreational Products Incorporated model year 2004 MX Z Adrenaline 800 H.O. X-package, which was the manufacturer's sportiest model of the standard line-up at the inception of this project. In general terms, it can be described as a light, highly manoeuvrable, very high power-to-weight ratio snowmobile intended primarily for natural or groomed trails, at ease in moguls as well as on high speed technical trail

segments. Figure 2.1 is a reproduction of a promotional picture of the vehicle without the X-package option, consisting primarily in higher stiffness and damping suspension [36].

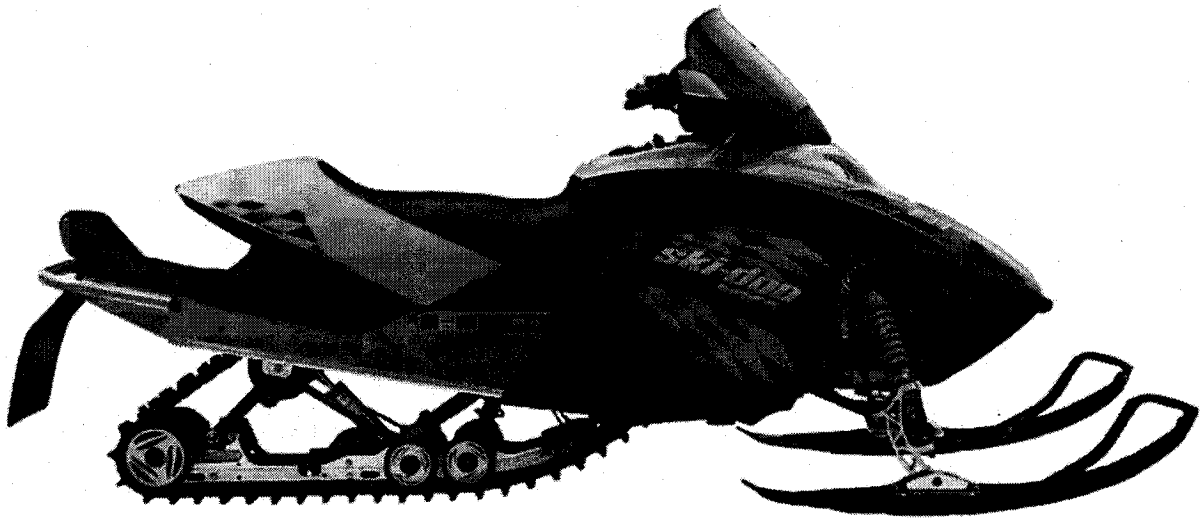

Figure 2.1: A pictorial view of the candidate vehicle, BRP's MX Z Adrenaline 800 H.O. 2004 [36].

An aluminum chassis, made of sheet metal and extrusions, forms the basis for the powertrain, suspension and controls. Aluminum is also extensively used in the two-cylinder, carburated two-cycle 800 cc engine producing around 140 bhp (104 kW). A typical short-long-arm double wishbone independent suspension is used at the front, with both arms inboard pivot axis down-sloped backward about 9 degrees. Coil-over-shock units support the front end, linking the chassis and the outer end of the lower arm so as to maintain a high motion ratio. An anti-roll bar also links the two lower arms together.

The rear suspension employs a complex five bar mechanism allowing the track's rigid guiding rail to bounce and pitch relative to the chassis over a limited range of displacement, while keeping the perimeter of the track path constant so as to spare with any other dynamic track tensioning mechanism. As shown in Figure 2.2, the five bars include the frame, the front arm, the rail, the rear pivot arm and the rear arm. Beyond

certain limits, the pivot axis linking the rear arm to the rear pivot arm comes in contact with rubber stoppers mounted on the rail, thus eliminating one of the two degrees of freedom of the rail relative to the chassis.

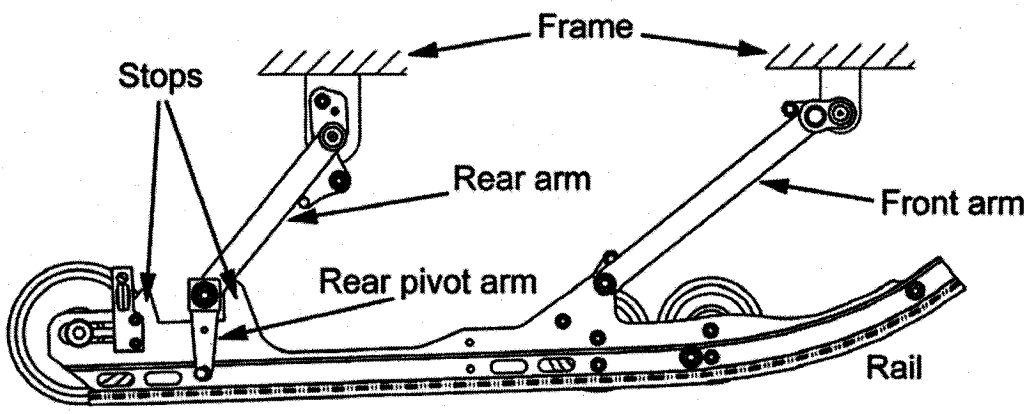

Figure 2.2: The rear suspension mechanism links.

The fuel tank sits over the tunnel (the long box shaped sheet metal part forming the rear of the chassis) and partly supports the driver seat, which is a polyurethane foam (PUF) construction covered with synthetic leather-like material.

Once instrumented and with fuel tank half full, the prototype vehicle had a mass of 259.5 kg, which is about 18 kg more than the production vehicle. Most of the added weight was concentrated in an aluminum box secured to the frame and positioned behind the seat, replacing the stock soft bag luggage space. Inside the box were the data acquisition module, the 12 volts battery powering it and the magneto-rheological (MR) damper controller and power modules. Since this addition was the only modification to the vehicle's general configuration and appearance, the changes in its aerodynamic characteristics compared to the production unit were considered to be minimized. The standard vehicle aerodynamic data were thus considered applicable. The addition of 54

stainless steel spikes to the track, in a staggered arrangement, was the sole other difference between a production unit and the prototype.

2.3 Required Degrees of Freedom for Chassis Behaviour Assessment

The design of an experiment protocol for vehicle response characterization, intended among else for model validation, requires prior knowledge of the general architecture of the simulation model and the target response variables. Considering that the present work represents a first step towards developing a quantitative tool for the designer to assess ride dynamics and perform essential design refinements in a convenient manner, an in-plane model of the vehicle was judged to be sufficient. Owing to the strong coupling between the drive torque and the rear suspension motion, it was considered essential to include the running gear rotational degree-of-freedom. Moreover, the driver-seat was considered as a single-DOF system, resulting in a total of 9 DOF for the in-plane vehicle model, as shown in Figure 2.3. Table 2.1 contains a short description of the included degrees of freedom.

Table 2.1: List of degrees of freedom included in model.

Symbol	Description
ϕ_s	Ski pitch around its revolute joint on the ski leg
D_l	Ski leg displacement
X_i	X coordinate of frame center of mass relative to an inertial reference frame
Z_i	Z coordinate of frame center of mass relative to an inertial reference frame
ϕ_c	Chassis pitch relative to an inertial reference frame
ϕ_b	Drive axle angular rotation relative to frame
D_r	Rail bounce relative to frame
ϕ_r	Rail pitch relative frame
D_s	Seat surface vertical displacement relative to frame

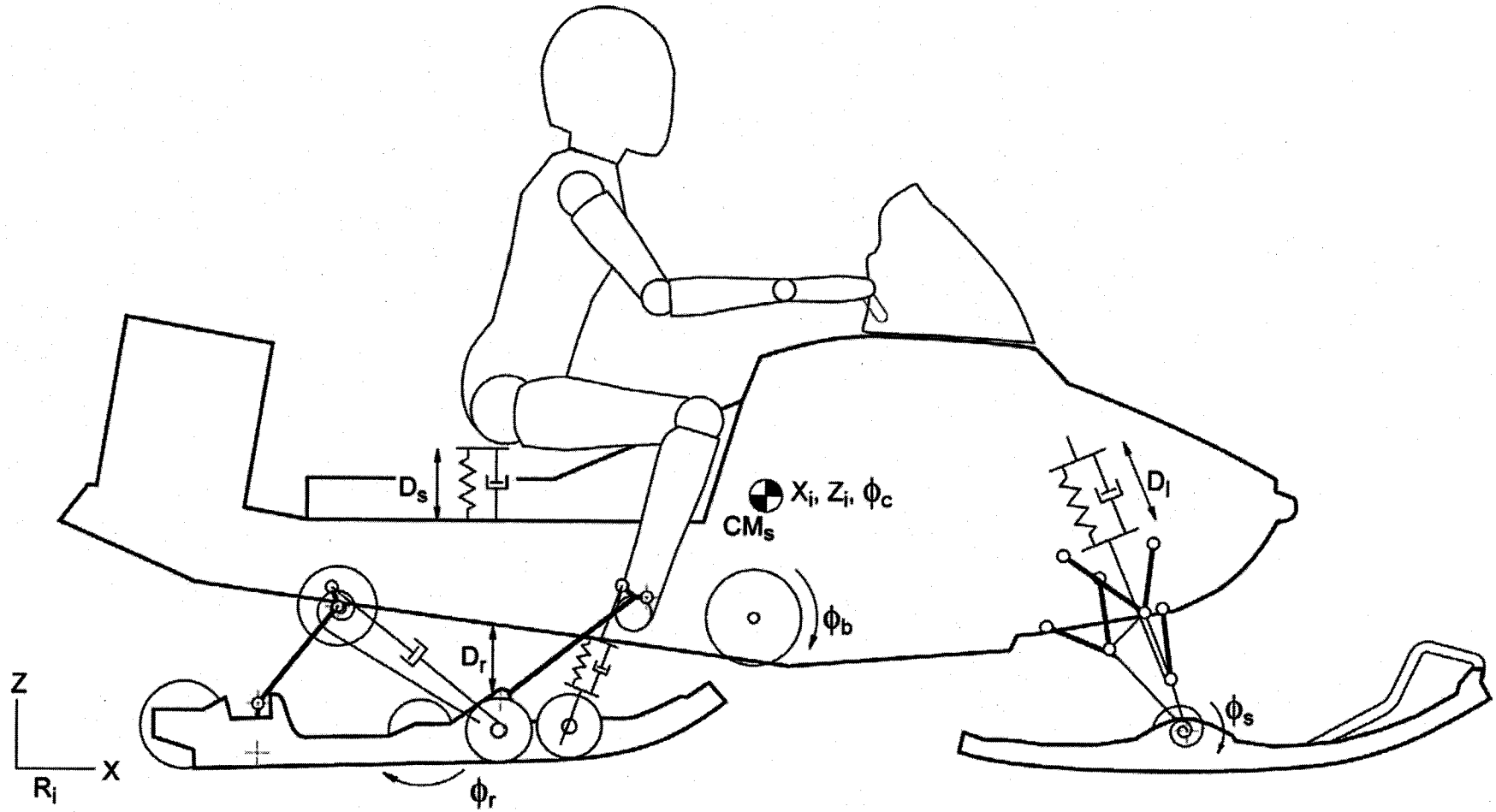

Figure 2.3: A schematic of the in-plane model and the associated DOF.

Considering that the model is primarily intended for ride analysis, all mechanisms along the path of vibration transmission from the ground excitation to the driver are included in the model. This translates in the inclusion of all four suspension DOF (bounce and pitch of skis and rail), bounce and pitch of the chassis and the seat surface deflection. While the contributions due to ski pitch may be relatively small, particularly over smooth trails, its bridging effect may have an influence over very rough mogul trails. Drive axle rotation is further included to enable simulation of transient maneuvers during which track and drive axle rotational inertias induce large forces influencing not only the longitudinal but also the vertical response. This is caused by the rear suspension couplings with the tension in the frontmost and rearmost track segments. By modifying the front arm and rear arm static inclination angle and moving the rear pivot arm stops position, the design engineers can tune the amount of coupling and thus modify the transient response of the vehicle.

2.4 Experimental Methods

This section presents the experimental methods used to obtain the snowmobile responses, over different terrains, required for model validation and tuning. Some other experimental methods were also employed to identify the modal frequencies of the candidate vehicle using equipment available at BRP but the results could not be considered reliable due to limited availability of the measurement systems and relatively poor experimental fixtures. The results attained from these preliminary attempts are thus not presented.

2.4.1 Field test program

The field test program was designed with two main components: (i) the selection of trail segments that form the primary excitation; and (ii) selection of measurands and the instrumentation for recording the excitation as well as the system response.

Four different trail segments were selected so as to cover the typical range of snowmobile trail surface profile found in North America. Trails in Scandinavia and parts of Europe are not maintained and groomed the way North American ones are [37]. The snowmobiles used in those regions possess different calibration and are typically ridden at lower speeds due to higher trail roughness, and thus deform and shape the trail surface differently, leading to further differences in the trail profile.

The four segments can be described as:

Segment 1: low average speed (7 m/s), 91.7 m long, high amplitude moguls trail;

Segment 2: medium average speed (15 m/s), 130 m long, medium-high amplitude bumps stretch;

Segment 3: one discrete mogul, measured over 22 m, forcing the vehicle to jump, loosing contact with the ground surface; and

Segment 4: high average speed (22 m/s), 190 m long, "ripple" bumps segment.

The above 4 segments were chosen among the trails available at BRP's test base in Chibougamau, Quebec, Canada. The limits of each segment were marked with cones such that repetitive trials could be performed over precisely the same segment. As snow eventually melts, no permanent marks were erected, although the exact longitude and latitude of the limits were recorded.

The surface profiles of the selected segments were characterized through measurements. A modular SoMat 2100 data acquisition system was configured to record up to 16 channels simultaneously, each encoded on 12 bits. Different layouts were defined for trail profiling and acquisition of vehicle responses, while the former employed only 8 channels.

The trail profiling method adopted here is simply based on the integration of the ski pivot acceleration along an inertial reference frame. Both longitudinal (X) and vertical (Z) accelerations were measured at the ski using two single axis micro-electro-mechanical-system (MEMS) accelerometers. The obtained signals thus constitute a local acceleration measurement along the ski reference frame, which is not an inertial frame. The pitch velocity of the ski about its lateral (Y) axis was measured using a MEMS angular velocity sensor. The accelerometers used were manufactured by IC Sensors (model 3145-020) and had a range of ±20g (±196.2m/s²) and a passband going from nearly zero to 500 Hz. The angular velocity sensor was from Silicon Sensing Systems (model CRS02) with a range of ±150°/s (±2.62rad/s) and an 85 Hz bandwidth. All three sensors were mounted close to one another in a purposely-designed rigid enclosure bolted to the right ski pivot bracket, called the "bridge", as shown in Figure 2.4. Both gravity and the accelerometers sensing device lever arms to the ski pivot axis were taken into account and their effects were appropriately considered in the profile reconstruction algorithm.

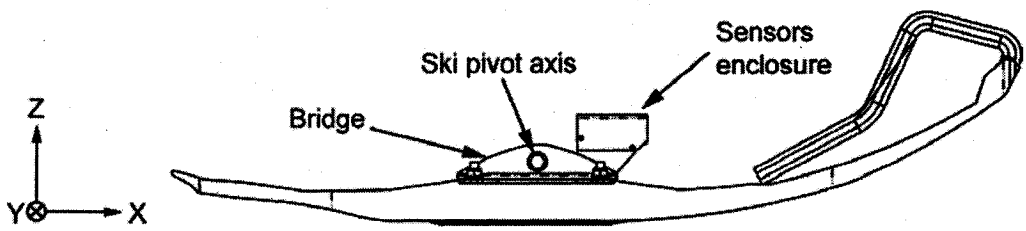

Figure 2.4: Sensors enclosure mounted on the ski bridge.

The experimental method is similar to that employed by the U.S. Army Land Locomotion Laboratory for off-road profile measurement [18] (see section 1.2.2). The present experiment design, however, replaces the cart used in the reported test by the ski. Moreover, the encoder employed in the reported study is replaced by the conventional accelerometers while the gyroscope is replaced by an angular velocity sensor. The other signals recorded while profiling were GPS measurements of ski longitude, latitude, altitude and the ground velocity, all updated once per second by the sensor but sampled at 10 Hz. A switch used to record time flags was recorded on two different channels, one being sampled at 500 Hz and the other at 10 Hz so as to simplify the data treatment. The signals acquired from the three sensors were initially processed through a 6-pole Butterworth low-pass filter with a cutoff frequency of 40 Hz and then sampled at 500 Hz.

Although the GPS recordings were intended to eliminate drifting of the velocity and position signals arising from the integration procedure, the present analysis did not attempt for such corrections due to the high magnitude discontinuities observed in the longitude and latitude data. These discontinuities most probably occurred due to changes in the referenced GPS satellites. The data acquired from the ski-mounted sensors and the switch were thus used for profile characterization. Table 2.2 summarizes the different variables, sensors and the channel numbers for trail profile measurements.

Table 2.2: Data recorder set-up for profile measurements.

Channel no.	Variable	Sensor	Range	Calibration
1	A_z_ski	ICSensor, 3145-020	± 20 g	0 v = -9.81 m/s²
2	A_x_ski	ICSensor, 3145-020	± 20 g	0 v = 0 m/s²
3	Φ_ski	Silicon Sensing, CRS02	± 150°/s	0 v = 0 °/s
4	Lattitude	Motorola HAWK GPS	0-360 °	0 v = 0°
5	Longitude	Motorola HAWK GPS	-90–90°	0 v = 0°
6	V_x_ski	Motorola HAWK GPS	*	0 v = 0 m/s
7	Altitude	Motorola HAWK GPS	*	0 v = 0 m
8	Switch	N.O. switch	-	-

*: essentially unlimited for on-ground measurements.

After acquiring the profile of a particular segment, the field trials were continued for recording the ride dynamic responses of the vehicle. For this purpose, the ski-mounted sensors were disconnected and the data acquisition system layout was changed to record the 16 chassis data channels. A total of eleven sensors were installed on the chassis, as shown in Figure 2.5. Two MEMS accelerometers were mounted near the static mass center of the vehicle-driver system and were oriented along the longitudinal (X) and vertical (Z) axes. An angular velocity sensor (Silicon Sensing Systems, model CRS02) was mounted on the chassis to measured its pitch velocity (ϕ_{pc}). Strain gages were installed on all suspension coil springs (one for each ski, D_{L1} and D_{L2}, and two mounted on the center damper, D_{C1} and D_{C2}) to measure their deflections. A linear potentiometer, mounted with spherical bearings, measured the position of the upper part of the rear pivot arm relative to the rail (D_P). This data, along with D_{C1} and D_{C2}, allow computation of the rail's position and orientation relative to the frame. Both the drive-axle torsional strain and angular velocity relative to the frame (ϕ_{pb}) were measured using strain gages and a timing light, respectively. Drive-axle strain was scaled to obtain the drive torque (τ_b)

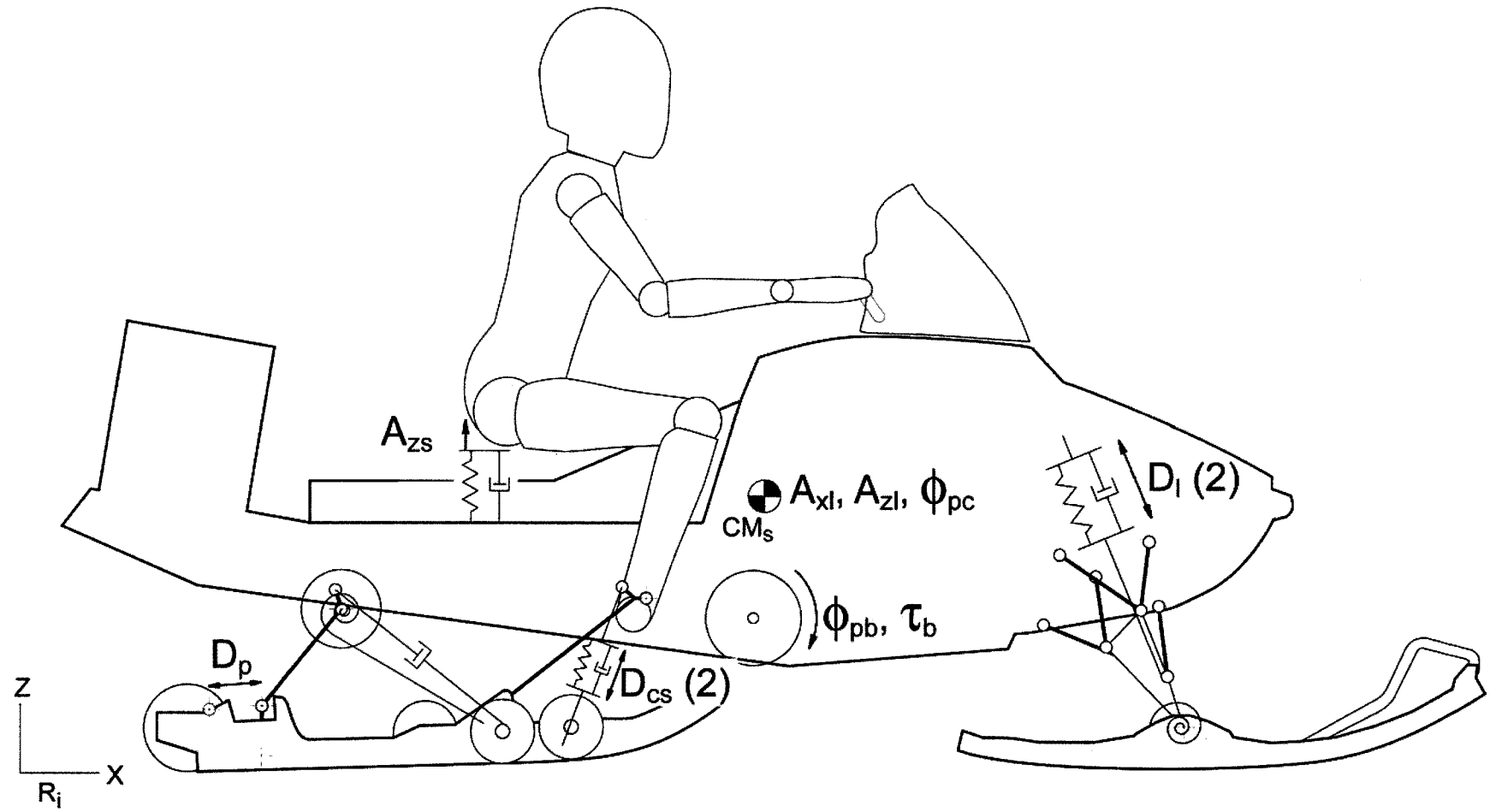

Figure 2.5: Measured variables related to ride dynamics response.

using a calibration table. Lastly, the seat surface vertical acceleration (A_{zs}) was recorded using a PCB Piezotronics 3 axis seat pad ceramic shear ICP accelerometer (model HT356A21) connected to a charge amplifier. Only the vertical acceleration component was recorded due to the limited number of available charge amplifiers. It was also judged unnecessary to measure the ski angular position relative to the ski leg.

The frame accelerations and angular velocity signals were low pass filtered with cut-off frequency of 40 Hz and sampled at 500 Hz, as in the case of the profile measurement. The acceleration signals were measured using Crossbow Technology accelerometers with a range of ± 4 g (± 39.2 m/s^2) and passband of 0-100 Hz. The seat accelerometer signal could not be filtered because of the limited number of SoMat filtering modules available. Although the PCB sensor used had a passband of 0.5-1000 Hz, aliasing was expected to be negligible given that very little energy is typically transmitted through seating devices past 80~100 Hz and that the sampling frequency was set to 500 Hz. The other aforementioned signals from strain gages, potentiometer and timing light were not filtered and were sampled at 100 Hz. As for profiling, a GPS antenna provided longitude, latitude and the ground velocity, all refreshed every second but sampled at 10 Hz. The signal from time flag switch was also recorded during the measurements. Table 2.3 summarizes the different variables, sensors and the channel numbers for vehicle responses measurements.

Table 2.3: Data recorder set-up for vehicle responses measurements.

Channel no.	Variable	Sensor	Range	Calibration
1	A_{zl}	ICSensor, 3145-020	± 20 g	0 v = -9.81 m/s²
2	A_{xl}	Crossbow, cxl04lp1	± 4 g	0 v = 0 m/s²
3	Φ_{pc}	Silicon Sensing, CRS02	± 150°/s	0 v = 0 °/s
4	A_{zs}	PCB 356A21	± 4905 m/s²	0 v = 0 m/s²
5	D_{cs1}	Strain gage	0-42 mm	0 v = 0 mm
6	D_{cs2}	Strain gage	0-48 mm	0 v = 0 mm
7	$D_{l\,r}$	Strain gage	0-177 mm	0 v = 0 mm
8	$D_{l\,l}$	Strain gage	0-177 mm	0 v = 0 mm
9	τ_b	Strain gage	-300-150 Nm	0 v = 0 Nm
10	Φ_{pb}	Timing light	15-4000 rpm	0 v = 0 rpm
11	D_p	Linear potentiometer MLT-005-N-7500-B5C	0-125 mm	0.5 v = 0 mm
12	Latitude	Motorola HAWK GPS	-90-90°	0 m = 0v
13	Switch	N.O. switch	–	–
14	Longitude	Motorola HAWK GPS	0-360°	0 m = 0v
15	Ground Speed	Motorola HAWK GPS	*	0 m = 0v
16	Altitude	Motorola HAWK GPS	*	0 m = 0v

*: essentially unlimited for on-ground measurements.

2.4.2 Test Protocol

For each of the four trail profiles, the test procedure was started with the choice of the exact segment limits. Following visual inspections, the pilot executed a trial pass for selecting the exact limits on the basis of the particular features of the terrain, namely, bends and very severe bumps or dips. The trail profile was then measured manually, at half its width. Using a long 12.7 mm diameter vinyl tubing as a water level, the height differences were recorded for successive 10 m intervals over the entire segment. The profile of segment 3, consisting in a single severe bump, was measured using an alternate

method, employing a taut string between points above the short discrete mogul. Vertical distances between the string and ground were manually measured at every 10 cm interval. A qualitative description of the snow texture was also recorded.

For acquisition of the surface profile, the snowmobile ski pivot was aligned with the first segment limit, while the absolute inclination of the ski sensor enclosure was precisely measured using a Mitutoyo digital protractor. The data acquisition was started as the pilot smoothly accelerated the vehicle up to 5 to 7 km/h, and subsequently maintained the speed constant. The pilot was also instructed to ride the vehicle in "mid-path" of the trail up to slightly past the second limit where the snowmobile was stopped and the sensors enclosure inclination was again measured. The recorded data were then visually checked for any obvious problem (angular velocity sensor momentary saturation, broken wire/disconnected sensor, etc.), which completed that segment profile measurement run. Typically, one or two trials were required to get one "clean" recording, which was considered sufficient for the profiling needs.

The vehicle ride response measurement layout was then loaded in the SoMat data acquisition system and the snowmobile ski was again aligned with the first segment limit. Similar to the profiling run, the frame absolute inclination, instead of the ski sensor's enclosure, was measured prior to starting the data acquisition. Following a fast acceleration the pilot maintained a constant velocity, close to the maximum endurable over each specific trail roughness, up to the segment's end and then braked so as to stop as soon as possible. Frame inclination angle was also recorded at the end of each run followed by the visual data verification. The tests were repeated until three successful

runs were obtained under similar average velocity. The trials were then repeated for the other segments.

Some modifications to this protocol, however, were required for the last two segments. All tests were conducted at BRP's Chibougamau test site over a three days period. Segment 4 was measured before dawn on the third day and, hence, had to be processed quickly. Therefore, its vertical rise was not manually surveyed although its length was correctly measured and marked with cones. Moreover, to save the time required to switch data acquisition layouts, the profile was measured using the chassis sensors while traveling very slowly so as to minimize the contributions due to the suspension displacement. For segment 3, the recording of the takeoff and landing points along the segment were added to the protocol.

2.5 Data Analysis and Experimental Results

This section presents the data analysis methodologies and samples of the acquired data. The analysis of the trail roughness data is presented first, followed by the vehicle response data analysis in the time and the frequency domains.

2.5.1 Roughness Characterization of the Trails

The actual profile of the trail roughness was re-constructed from the acquired elevation data. This involved a combination of the manual survey data, the manually measured ski inclination data and the digital recordings. The survey data was used to correct for the drifts in the surface elevation to obtain a high resolution profile reconstitution with large wavelength content limited at the low end by the ski length bridging effect and at the high end by half the segment length. The resulting

reconstruction of the experimental profile thus included the DC component as well as the actual vertical rise of the end limit relative to the first. The reconstructed profile data were thus pre-processed to eliminate the DC components due to overall slopes in the terrain [18,19,24] before deriving the power spectral density (PSD) of the roughness profile. The PSD's were then further analyzed to derive a power regression function relating the spatial PSD and the spatial spectral component of the profile. The data acquired during all measurement passes were further evaluated to determine the mean, and lower and upper bounds of the roughness profile. The three resulting spectral densities were represented by power regression functions.

Reconstitution of the roughness profile involved seven steps, which are briefly described below:

1) The ski longitudinal acceleration and angular velocity signals together with the initial inclination of the sensors enclosure and the relative coordinates of the segment limits are loaded in memory.

2) The pitch angular acceleration of the ski is approximated through differentiation of the angular velocity and the instantaneous acceleration of the ski pivot axis is computed using the known lever arms between the accelerometers and the ski pivot axis.

3) The instantaneous inclination of the ski at each time step is computed through integration of the angular velocity signal starting from the manually measured initial inclination.

4) The gravity component is then subtracted from the accelerometers signals using the above instantaneous inclination data.

5) At this point, it was possible to compute the local displacement increment of the ski over the current time step through simple numerical integration of the velocity signal. The current local velocity

is also computed by integrating the instantaneous longitudinal acceleration and adding it to the previous step velocity, projected along the current ski reference frame orientation.

6) The actual trail profile was then reconstructed by summing all local displacement increments projected on the inertial frame of reference. On most segments, the resulting profile results in some drifting, spanning either too much or not enough of the X and Z axes, compared to the manual measurements.

7) Based on the assumption that these drifts primarily arise from the accumulation of minute integration errors, the computed X and Z coordinates were linearly scaled such that the coordinates of the initial and final points corresponded well with the measured coordinates.

In Figure 2.6 and Figure 2.7, the vertical elevations of the rebuilt profiles of segments 2 and 3, respectively, are compared with those obtained through manual measurements. The rebuilt profiles are seen to be quite close to the manually measured ones, although some deviations are evident. This is attributed in part to the ski's bridging effect, which tends to smoothen the effects of small bumps and in part to the aforementioned drifting of the rebuilding procedure that cannot be entirely compensated for. The roughness profile was resampled to ensure constant resolution of 0.05 m between the successive data points.

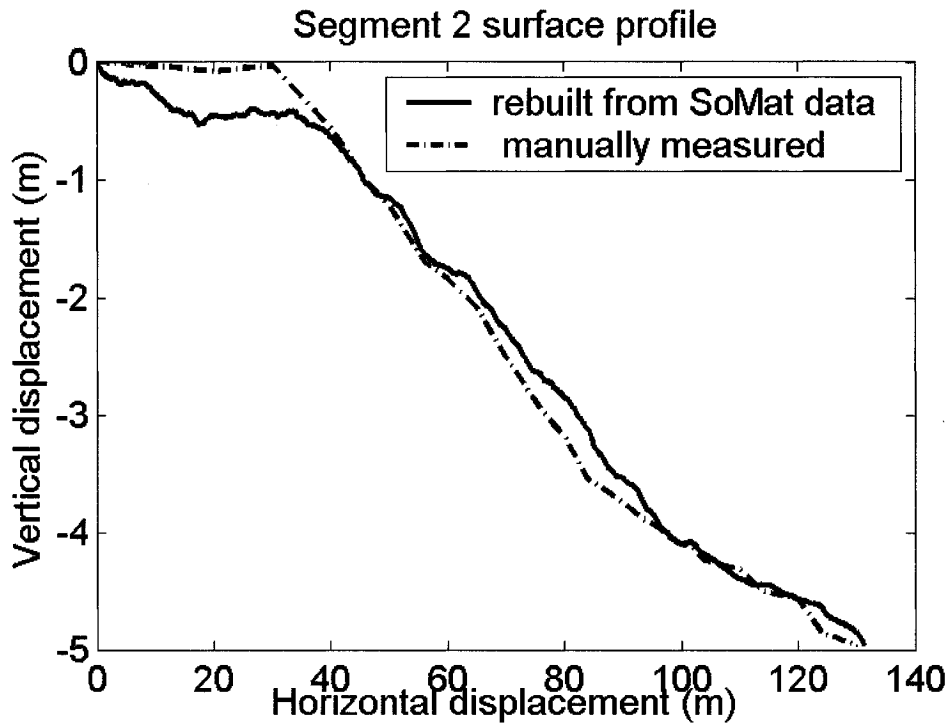

Figure 2.6: Comparison of the profile of segment 2 reconstructed from the SoMat acquisiton system recordings with manual measurements.

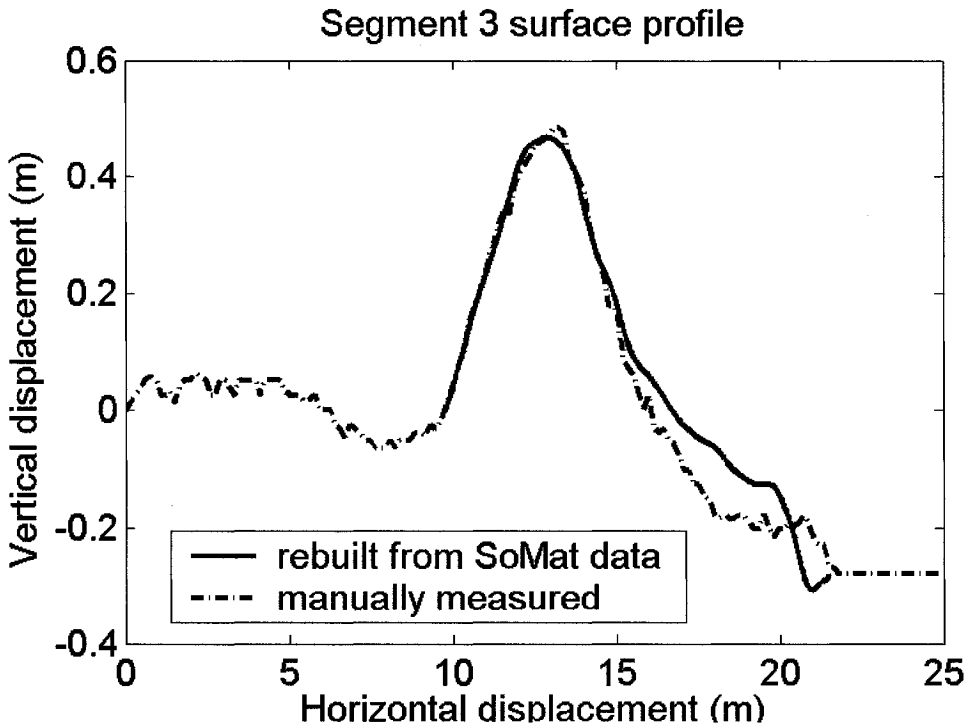

Figure 2.7: Comparison of the profile of segment 3 reconstructed from the SoMat acquisiton system recordings with manual measurements.

The resulting displacement signals were filtered through a high-pass filter to eliminate the contributions due to local gradients of the trail and to determine the roughness properties about the local mean values. Each filtered signal was then split into partially overlapping (75%) 256 or 2048 samples blocks, depending on the original length of the data. A Hanning window, with normalized amplitude, was then applied to each block and the PSD of the roughness was computed for each. Finally, the PSD's of all blocks were averaged to obtain the mean trail segment PSD.

The upper and lower bounds, and the mean values of the surface roughness PSD's were computed from the PSD's of the four segments profiles. Figure 2.8 illustrates the mean, and lower and upper bounds of spatial PSD of the terrain elevation versus the spatial frequency. Simple piecewise exponential functions are then fitted to the bounds as well as the mean using the Simplex unconstrained optimization algorithm [38,39] implemented in the Matlab *fminsearch* function, by minimizing the sum of absolute errors (SAE). Such an approach has been widely used to determine the PSD of road elevations [18,19]. The spatial PSD of the resulting spectra can be described by the power function:

$$S_Z(\Omega) = \begin{cases} C_0 \cdot \Omega^{-S1} \Rightarrow \Omega < \Omega_1 \\ C_1 \cdot \Omega^{-S2} \Rightarrow \Omega \geq \Omega_1 \end{cases} \tag{2.1}$$

where $S_Z(\Omega)$ is the spatial PSD of the trail elevation as a function of the spatial frequency Ω in cycles/m, C_0 and C_1 are the constants, and S_1 and S_2 are the exponents adjusted to the envelope mean, respectively, for $\Omega < \Omega_1$, and $\Omega \geq \Omega_1$, and Ω_1 defines the frequency corresponding to the transition of the two functions.

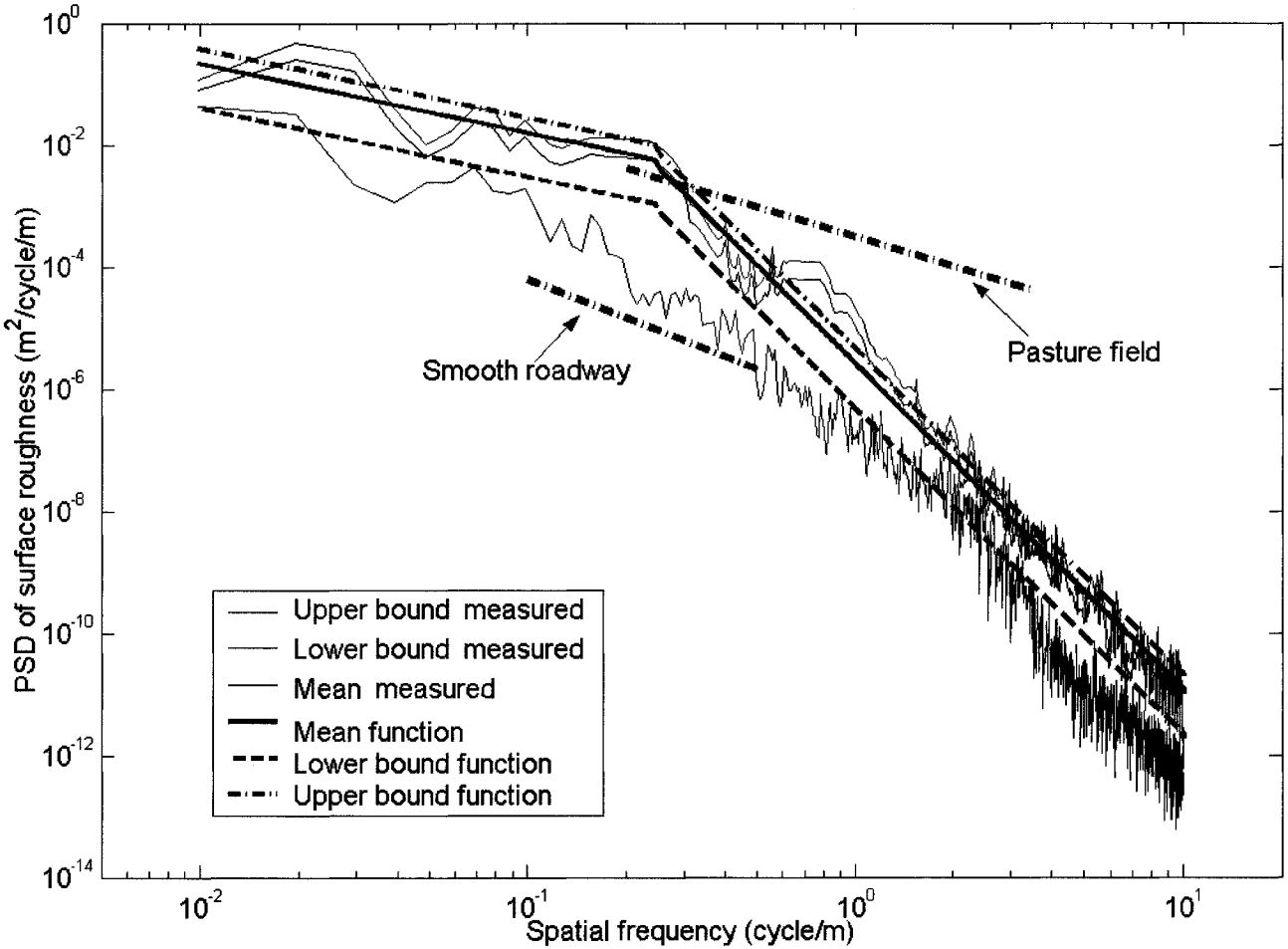

Figure 2.8: Upper and lower bounds, and mean values of the spatial PSD of trails elevations, and comparisons with the power functions and roughness spectra of selected terrains.

The continuity between the two functions at Ω_1 is ensured by:

$$C_1 = C_0 \ \Omega_1^{(-S1+S2)}$$

From the PSD of the processed experimental elevation data, Ω_1 was set as 0.25 cycle/m.

Since the range of PSD values spans almost twelve orders of magnitude, a direct minimization of the SAE would yield a curve fitted solely to the high amplitude corresponding to lower frequencies. Three weighting regions were thus defined over the spatial frequency range of interest to ensure adequate contributions of errors in the entire range.

Table 2.4 summarizes the weightings applied in the three ranges of the spatial frequency. Table 2.5 lists the coefficients and weighted SAE of each fitted curve.

Table 2.4: Weighting parameters used in fitting the roughness PSD envelope.

Weight	1	$10^{2.5}$	10^{7}
Ω (cycle/m)	$\Omega \leq 0.25$	$0.25 < \Omega \leq 2$	$2 < \Omega \leq 10$

Table 2.5: Parameters of the power functions formulated to describe the roughness PSD bounds and mean values, together with the SAE.

Function	*c0*	*s1*	*s2*	Weighted SAE
Lower bound	2.0815E-4	1.13884	5.3273	11.1
Mean	0.0011273	1.13884	5.3273	29.8
Upper bound	0.0019641	1.13884	5.3273	57.5

The comparisons of predicted and measured spectra, illustrated in Figure 2.8, suggest that the proposed power function can be applied to predict the range of spatial PSD of elevations of the selected trails. Figure 2.8 also illustrates comparisons of the

measured roughness PSD with those of typical smooth roadways and pasture, reported in [19]. The results suggest that the snow trails are slightly rougher than the pasture fields for $\Omega \leq 0.25$, and significantly rougher than a smooth roadway. A pasture field, however, exhibits significantly higher roughness PSD than the snow covered trails at frequencies above 0.25 cycle/m. This is coherent with the fact that snow is typically much softer and easier to smooth out than the other "dry" ground covers. The results also suggest that the snowmobiles encounter a relatively larger range of surface roughness in the frequency range of interest than the automobiles and farm tractors do.

2.5.2 Analysis of vehicle ride response data in the time domain

As an example, Figure 2.9 to Figure 2.11 illustrate the variations in the raw signals acquired on segment 2. Both the trigger and the GPS data were not used for model building or validation. The vertical (A_{zl}) and longitudinal (A_{xl}) acceleration measured on the frame, pitch velocity of the frame (ϕ_{pc}) and the seat vertical acceleration (A_{zs}) are presented in Figure 2.9. Figure 2.10 illustrates the deflection responses of center (D_{cs}), left-front ($D_{l\,l}$) and right-front ($D_{l\,r}$) springs, and rear pivot arm (D_p), respectively, while the drive-axle torque (τ_b) and angular velocity (ϕ_{pb}) signals are shown in Figure 2.11. Both the longitudinal acceleration (A_{xl}) and the drive torque (τ_b) point to high initial acceleration while lower magnitudes of both variables suggest nearly constant speed for $1 \leq t \leq 4.5$ s. Moreover, A_{xl} displays negative values for $t \geq 5$ s, suggesting braking. Clearly, the deceleration magnitude is considerably lower than the acceleration magnitude. This is believed to be caused by the packing of the grainy spring snow in the track's grousers, which led to the snowmobile stoppage primarily due to the viscous drag

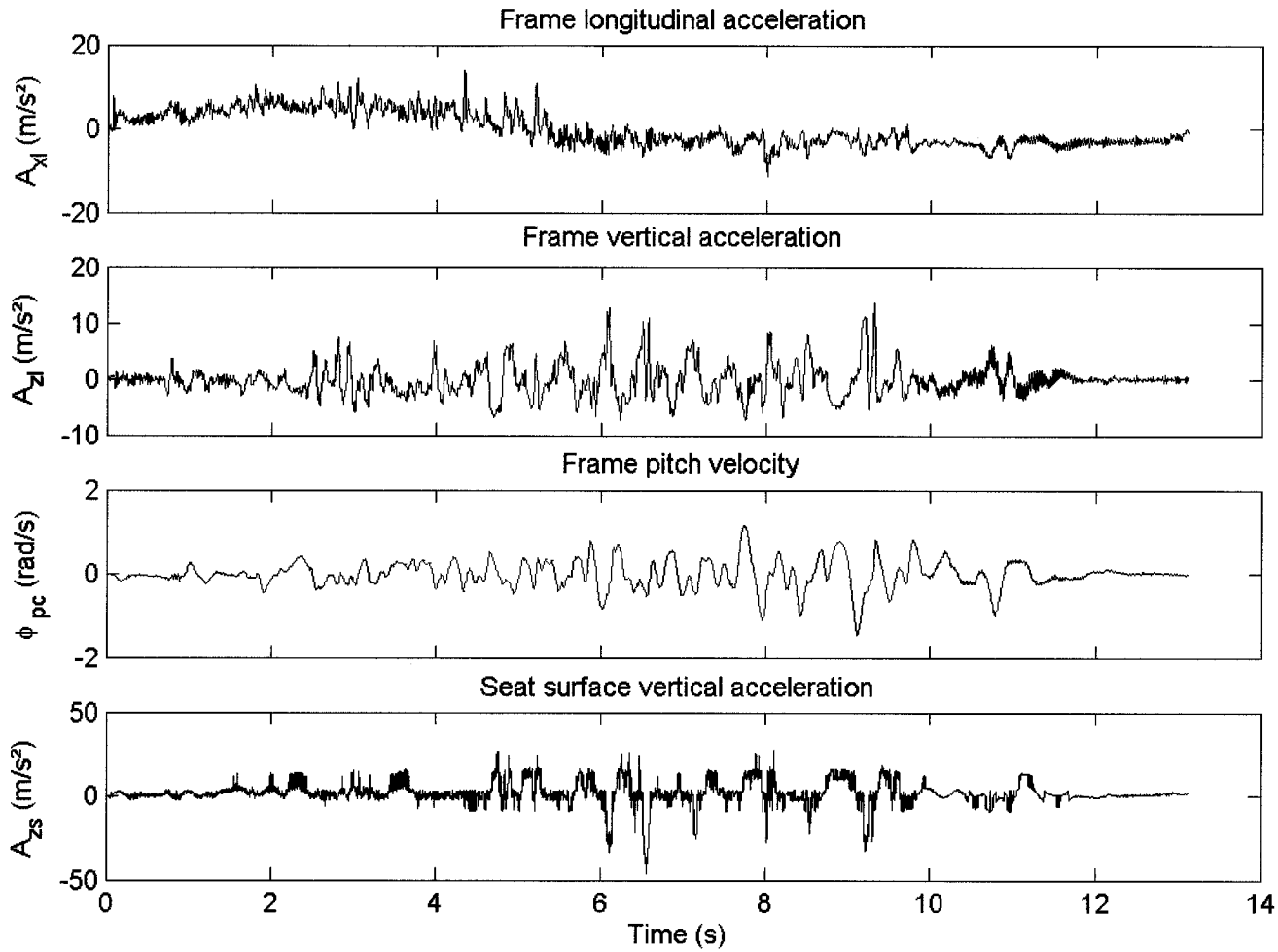

Figure 2.9: The raw signals of the frame longitudinal and vertical acceleration, frame pitch velocity and seat surface acceleration (Trail: segment 2).

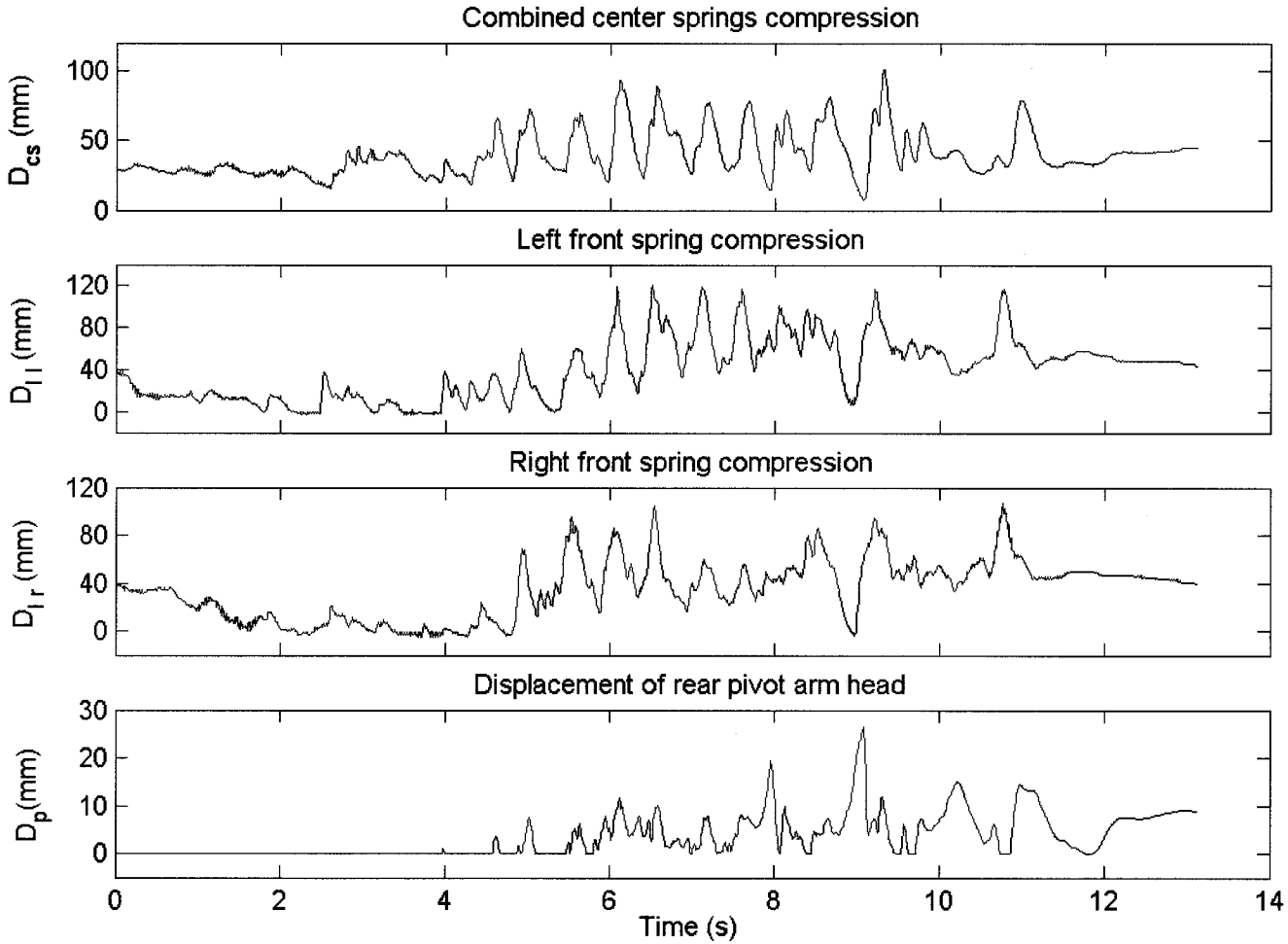

Figure 2.10: The raw signals of the center, left-front and right-front springs compression, and rear pivot arm displacement (Trail: segment 2).

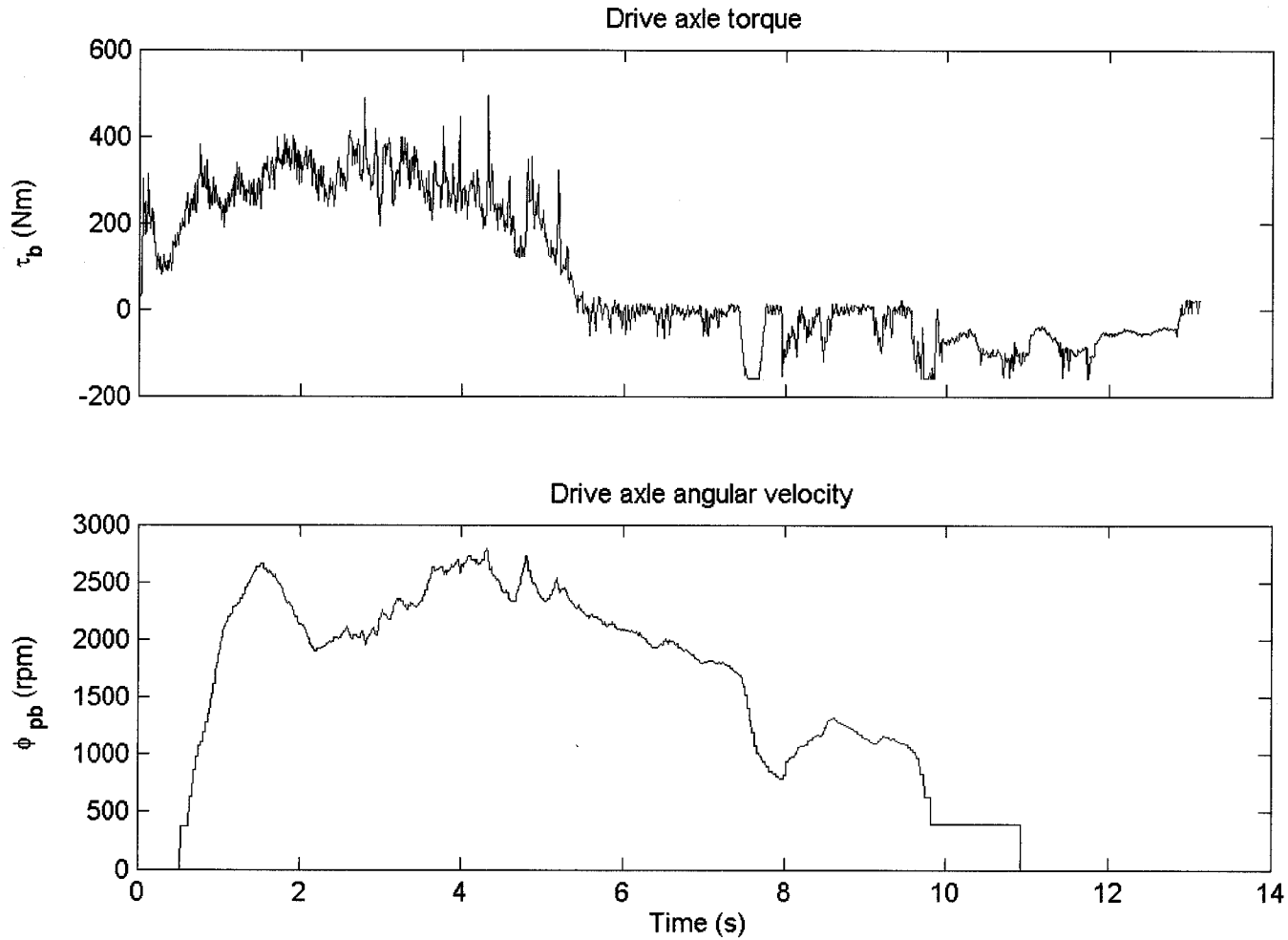

Figure 2.11: The raw signals of the drive axle torque and angular velocity (Trail: segment 2).

in the planar shear flow of snow created between the filled-track and the ground. The results also show that the seat acceleration peaks approach considerably higher values than the frame acceleration peaks.

Adopting an algorithm similar to that developed for the track profile rebuilding, the signals presented above were used to compute the vehicle's center of mass (CM) velocity and position as well as pitch angle responses. Plotting the CM global Z coordinate against the horizontal axis (X) yields the CM course. Figure 2.12 illustrates a comparison of the computed course with the vertical coordinates of the ground profile of the corresponding trail segment. The results show that the measurement and data treatment procedure are accurate enough to capture the general tendency as well as major bumps and dips, although the CM vertical oscillation amplitude seems to be amplified somewhat. The initial difference in the two elevations (i.e. at X=0m) is the static CM height. The apparent reduction of suspension compression between 80 and 110 m clearly illustrates that drifting from the integration procedure is not entirely compensated by the linear scaling correction. The ground profile rebuilding in general generated higher level of drifting than vehicle CM path rebuilding, mostly due to relatively longer duration of its raw signals.

Figure 2.13 illustrates the time-histories of the X and Z coordinates of the mass center together with the pitch angle. The initial acceleration and final deceleration events are clearly apparent in the pitch angle response, which assumes negative values at the beginning of the run and mostly positive values near the end. This in turn directly influences the vertical (Z) velocity response (Figure 2.14), which is the summation of the vertical excitation due to bumps and the projection of the forward velocity along the

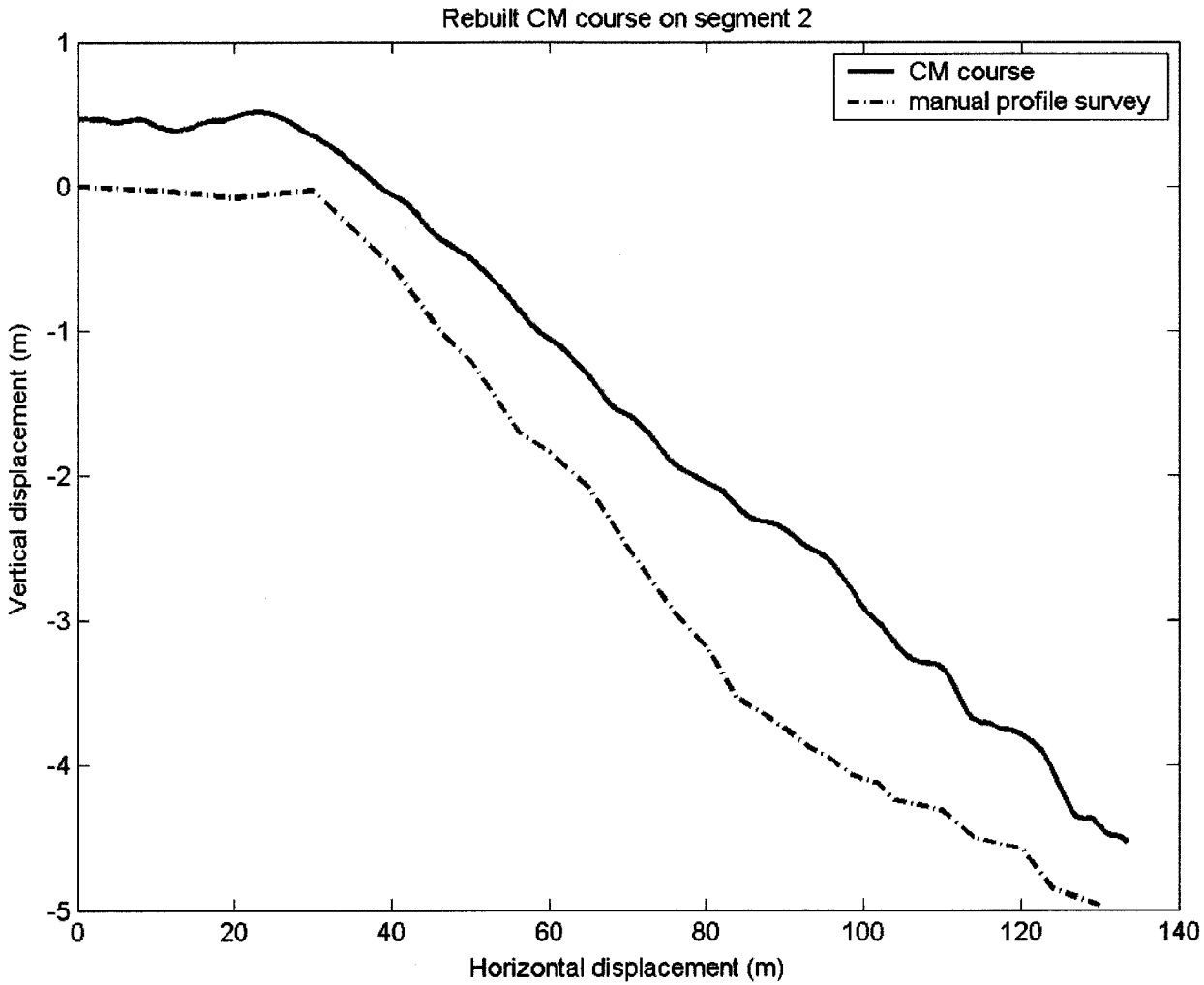

Figure 2.12: Comparisons of the measured frame center of mass course with the trail profile of segment 2.

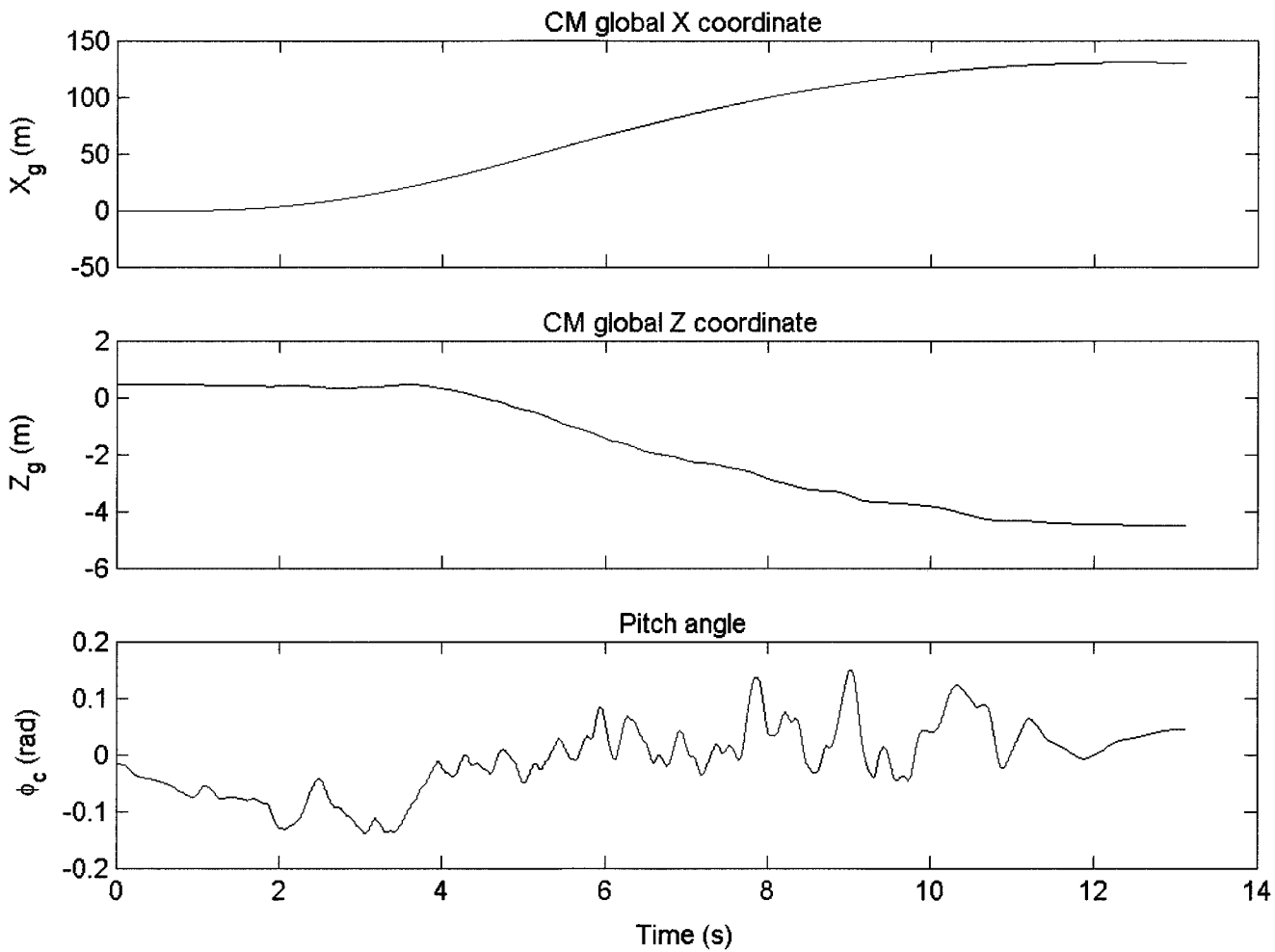

Figure 2.13: Time histories of the frame center of mass global coordinates measured on segment 2.

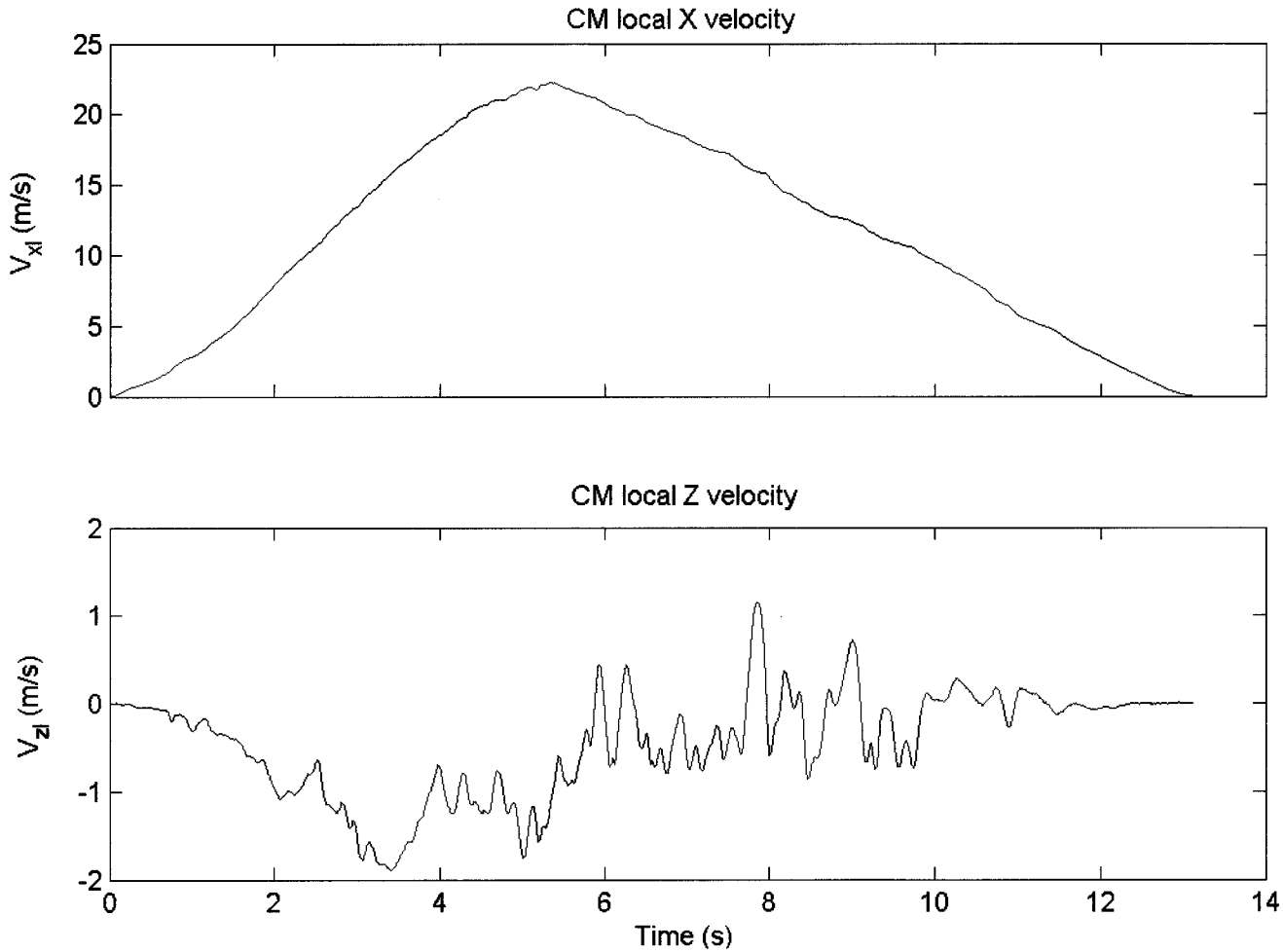

Figure 2.14: Time histories of longitudinal and vertical velocities of the frame mass center along the frame coordinate system (Trial: segment 2).

pitched frame coordinate system. Indeed, the mean value of the local vertical velocity approaches zero in the interval $6 \leq t \leq 10$ s, whereas it is clearly negative before and slightly positive past that interval. From the results, it is evident that in this particular run, the steady state condition was never achieved since longitudinal velocity never stabilized, as evidenced in Figure 2.14. The configuration of most trails around the Bombardier Chibougamau test site did not allow for acquisition under constant speeds. Moreover, the soft spring snow provided only one segment that could be considered as a "medium rough" profile, which however immediately preceded a tight turn with moguls. This forced the pilot to slow down before the end of the segment of interest. The acceleration zone of the test segments, however, was sufficiently long to reach the desired velocity at the beginning of the part of the segment presenting the desired roughness, which helped to reduce the signals length and thus the drifting induced by the integration procedure.

Characteristics and highlights of the measured signals are summarized below.

Drive torque (τ_b): The variations in the drive torque (τ_b), presented in Figure 2.11, are typical of those observed while riding segments 2 and 4. The torque attained on segment 1, however, was reasonably constant over a major part of the test run.

Drive axle angular velocity (ϕ_b): The variations in the angular velocity, shown in Figure 2.11, are typical of those observed on segments 2 and 4 although the data attained for segment 4 provided a very short section with nearly constant speed. The data acquired on segment 3 was of purely transient nature, while that on segment 1 was quite stable for almost 8 seconds.

Longitudinal acceleration (A_{xl}): The variations are generally very similar to those observed in the torque signal, while higher frequency oscillations are evident (Figure 2.9, first).

Vertical acceleration (A_{zl}): The initial and final portions revealed very low magnitudes of vertical acceleration with low frequency oscillations (Figure 2.9, second)

due to low longitudinal speeds at both segment ends. This signal is mostly uncorrelated with the longitudinal acceleration and torque signals except for the fact that amplitude peaks did not appear until acceleration had almost ceased. This may be partly due to the coupling of the rear suspension and track tension but probably more to the fact that the segments start points were chosen so that acceleration takes place on relatively smooth profile before the actual section of interest begins. The data acquired on segment 3 revealed liftoff of the vehicle, while the magnitude approached nearly –1 g.

Seat vertical acceleration (A_{zs}): The measured data, invariably, revealed flapping of the accelerometer pad against the seat cover surface adding to an already noticeable signal noise (Figure 2.9, fourth). The signals revealed variations from –10 to 16 m/s², except for segment 3 where the magnitude of seat acceleration varied from –15 to 75m/s².

Frame pitch velocity (ϕ_{pc}): The graph shown (Figure 2.9, third) is typical of most segments except segment 4, which presents the lowest range of all, going from -0.8 to 0.6 rad/s.

Frame CM longitudinal velocity (V_{xl}): As the signal shown in Figure 2.14, those from segment 3 never stabilize. In signals from segment 4, however, the acceleration steadily diminishes up to the beginning of the breaking zone, thus creating a short section usable to approximate a steady state condition. The signals from segment 1 are almost perfectly stable over a major central section.

Frame CM vertical velocity (V_{zl}): This signal typically goes negative under acceleration and comes back to slightly positive values under hard braking (Figure 2.14). It is most stable over segment 1, where it oscillates around –0.5 m/s for most of the test run. This directly results from the fact that the profile drops about 3.5 m over the segment's central 75m, which are covered in about 7s (-3.5m / 7s = -0.5m/s). Segment 3 presents the lowest peak at –2.9 m/s.

Frame pitch angle (ϕ_c): The central tendency of the measured data goes negative under acceleration and positive only under hard braking, as observed over segment 4 and, to a lesser extent, over segment 2 (Figure 2.13, third). Signals from segment 4 present the smallest range of all, going from -0.08 to 0.08 rad/s. Data from segment 1 are the most stable, oscillating by ±0.1 rad around the central tendency over the interval $2.5 \leq t \leq 10$ s. This constitutes the most intense and continuous pitching motion encountered in this study. Indeed, the driver's tolerance to pitch exciation is the velocity-limiting factor over segment 1. Segment 2 presents the largest range of pitch angle due to the large excursions of its central tendency. However, over that segment, the pitch angle oscillations around central tendency are the smallest.

Center spring deflection (D_{cs}): Static compression ranges from 38 to 42 mm all runs considered. Segment 2 (Figure 2.10, first) presents the largest deflection range, going from 8 to 100 mm. Over segment 3, the suspension extends up to it end stops while the vehicle is airborne.

Front springs deflection ($D_{l\,l}$, $D_{l\,r}$): As evidenced in the second and third plots of Figure 2.10, there are significant differences between the right and left signals over all segments, except over segment 3. Although it does not stand out in the figure, the high compression observed in the braking zone typically persists after full stop, showing that there is noticeable hysteresis in the suspension.

Rear pivot arm position (D_p): The arm typically sits against its "zero" stop (i.e. rear stop) during acceleration and moves when the vehicle gets in the bumps and forward acceleration has stopped (Figure 2.10, fourth). Segment 1 signals best approximate the steady state condition. Over segment 3, the arm hit its front stop while the vehicle was airborne.

CM global position (X_g, Z_g): The first and second plots of Figure 2.13 present typical position signals in that they vary smoothly and monotonically, without noticeable oscillations. Over most segments, the vertical position decreases from start to finish, indicating that trails are either flat or slightly descending. They have been so chosen because it is very difficult to maintain a constant low velocity while going uphill, which is mandatory for trail profiling. This difficulty originates from the engagement of the continuous variation transmission (CVT) around 3500 rpm and its disengagement around 2000 rpm. Segment 3, consisting of a single snow bank used as a jump, is the sole exception to this rule.

The spectral components of the measured responses were computed using FFT techniques. For this purpose, the data segments free from occasional transient events and approximating the steady state responses fairly well were extracted from the measured data series. The data acquired from segment 3, however, formed an exception to this as the entire data series was considered for analysis. The measured frame CM accelerations and pitch velocity, and the seat surface vertical acceleration signals were high pass filtered to eliminate their DC component. As illustrated in Figure 2.15, the filtered signals exhibit mean values near zero. The suspension deflections and drive-axle torque signals, as well as their derivatives, however, were computed directly without prior filtering, as

shown in Figure 2.16 and Figure 2.17, respectively. The data are analyzed to compute the mean, rms value, the crest factor and the peak magnitude with 99% probability (peak@99%).

Analysis of the computed responses for all the runs revealed several interesting characteristics. The responses measured over segments 1 and 4 showed a slight attenuation of the rms vertical acceleration from the frame to the seat surface, whereas the data for the other two segments revealed amplification of the frame vibration transmitted to the seat. No attempt are made to conclude on the seat properties based on these data since the latter two segments cause vibration of transient nature and high crest factors. The highest rms values of the frame and seat surface vertical acceleration, of 6.7 and 8.5 m/s^2 respectively, were attained over segment 2, while the response for segment 1 resulted in the lowest values, at 4.2 and 3.7 m/s^2 respectively. The rms values of longitudinal acceleration were quite comparable for all the runs as its minimum value of 1.8 m/s^2, attained on segment 1, is nearly 65% of its maximum value of 2.8 m/s^2, attained on segments 2 and 4. Unexpectedly, segment 2 produced the highest rms pitch velocity, closely followed by segments 1 and 3, even though these last two segments revealed higher surface roughest in the entire spatial frequency range, except between 0.33 and 0.6 cycle/m, where segment 2 surface was rougher. Crest factors due to vibration responses approached a maximum value of 4.6 for the seat vertical acceleration over segment 3, as should be expected when landing a jump.

Both the mean and rms values of the front and center spring compressions were observed to be highest on segment 2. The mean and rms values of the potentiometer movement and the axle torque were lowest over segment 1 and highest over segment 3,

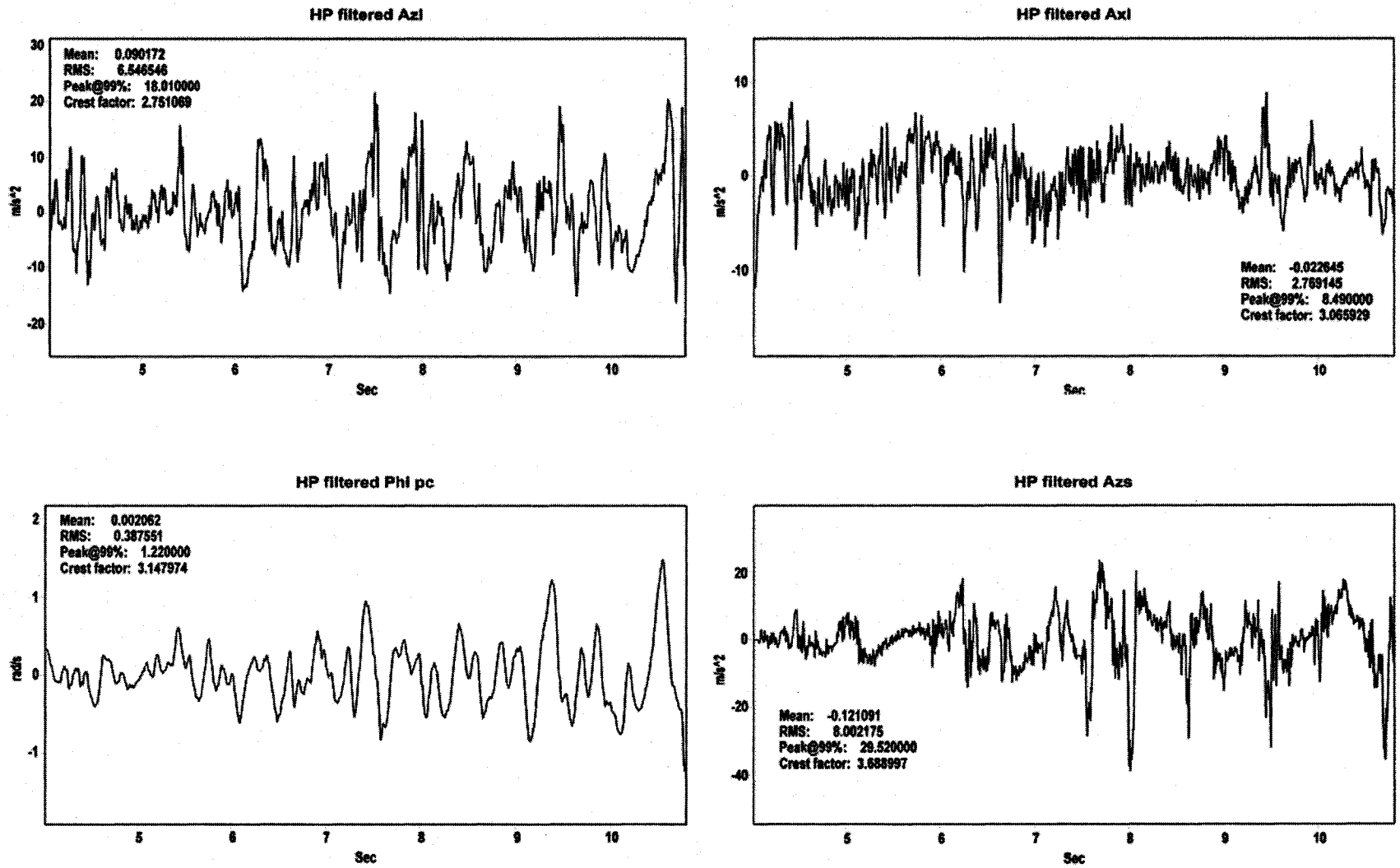

Figure 2.15: Time histories of high-pass filtered acceleration and pitch velocity signals.

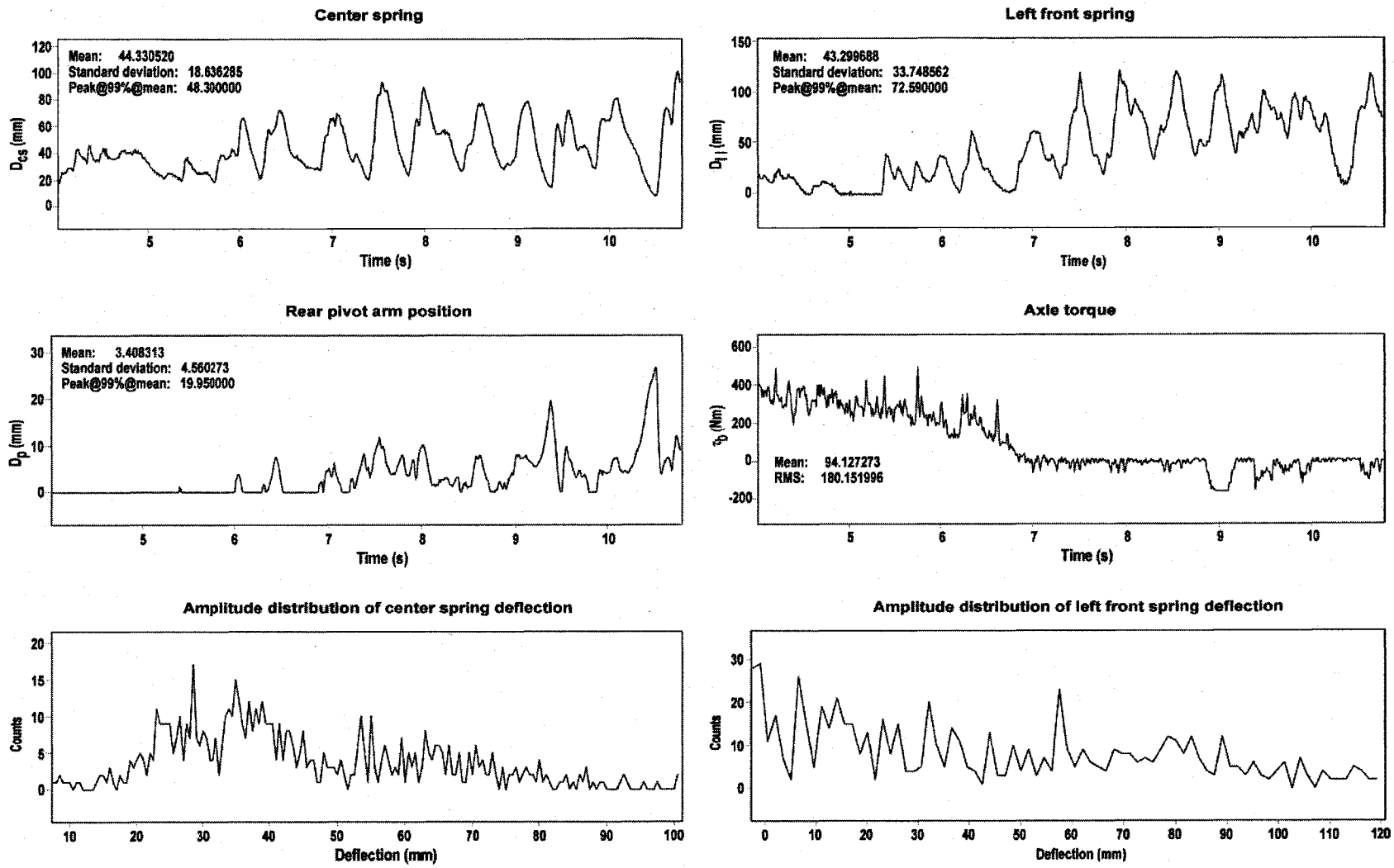

Figure 2.16: Time histories of suspension spring deflections and axle torque, and suspension spring deflection histograms.

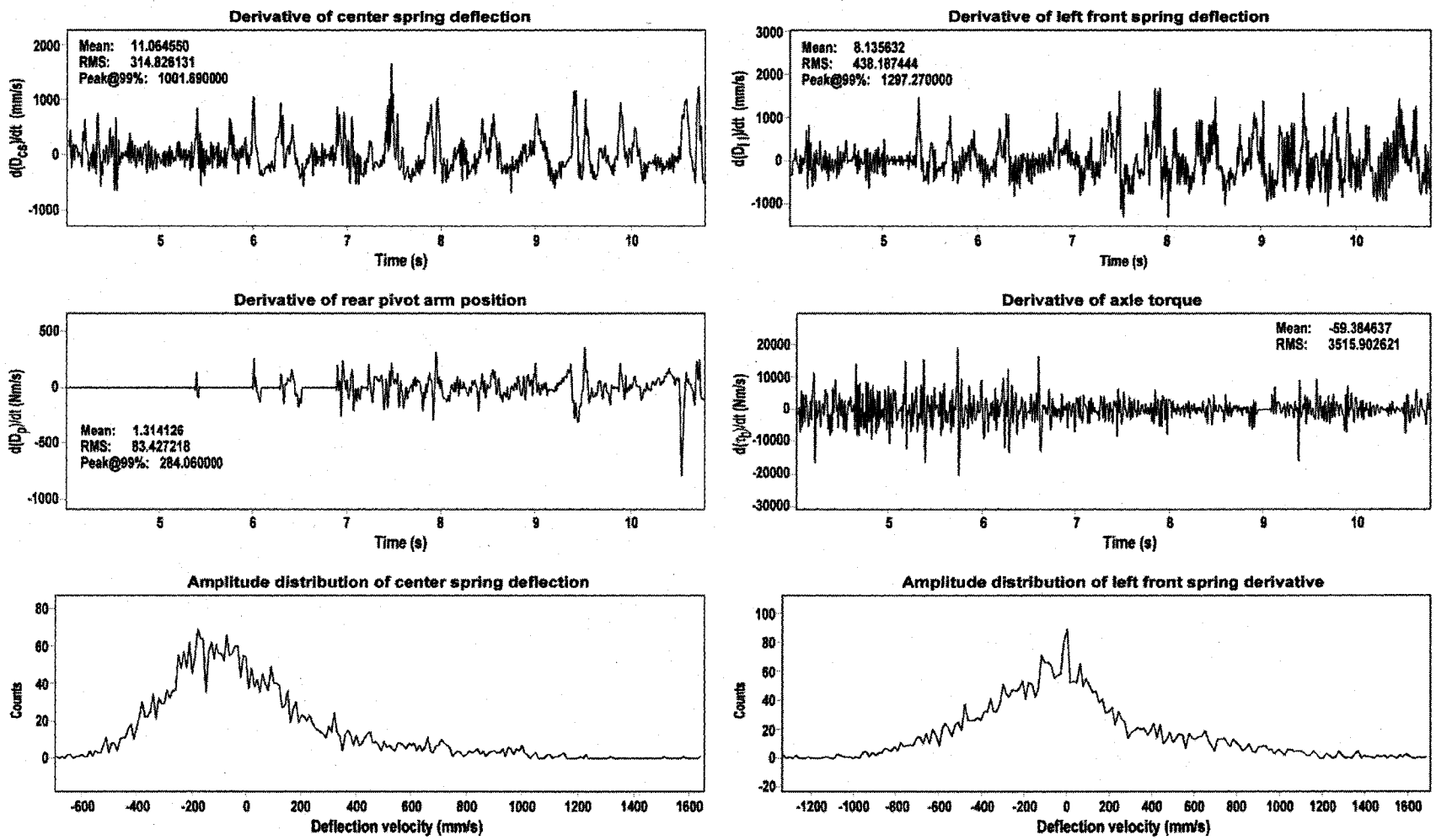

Figure 2.17: Time histories of the derivatives of suspension spring deflections and axle torque, and histograms of the derivatives of the suspension spring deflections.

confirming that response over segment 1 constitutes the best approximation of a steady state condition while response over segment 3 is purely transient. The histograms of the suspension deflections (Figure 2.16, third row) further revealed that the lowest mean tendency for the center spring compression and the highest mean tendency for the left front spring compression occur over segment 1, as expected on a trail for which the velocity is limited by the pitch motion intensity, not by the vertical vibration intensity. Similar trends were also observed in the time derivatives (velocities) of the suspension springs compression (Figure 2.17, third row). The mean relative velocity of the center spring remained negative for the majority of the test run, which is attributed to high rebound damping

The major highlights of the rate of change graphs (Figure 2.17) are very similar to those of the positions graphs just reviewed. Segment 2 clearly generates the highest suspension deflection velocities while minimums are distributed throughout the other segments. The mean tendency of the center spring compression velocity is negative in most runs, its histograms being slightly skewed to the left. This is due to the center damper having a higher damping constant in extension than in compression. This remark also applies to the left front shock although it does not stand out as clearly in the presented graphs.

2.5.3 Frequency Analysis

The measured ride responses are finally evaluated in the frequency domain in terms of power spectral densities of the vertical, longitudinal and pitch acceleration

signals. The results are particularly important to identifying the dominant spectral components of ride vibration and thereby the dominant modes and natural frequencies.

As an example, Figure 2.18 presents the PSD of longitudinal and vertical accelerations of the frame, seat surface vertical acceleration and frame pitch velocity, obtained from a typical run over segment 2. For each of the four signals, the combination of all runs from a given trail segment typically revealed 4 to 6 clearly discernable peaks occurring mostly at frequencies below 20 Hz. Most of these are common to two or more trail segments as only 3 of the 16 condensed graphs so obtained did present one orphan peak of unknown origin. The PSD's of the measured signals acquired for each trail segment were combined to identify the frequencies corresponding to the peak magnitudes observed in all the signals.

Table 2.6: Frequencies of PSD peaks for each trail segments.

Segment	Frequency ranges corresponds to peaks (Hz)							
1	0.5~0.7		1.7~2			3.9~4.3	4.7~5.1	
2	0.5		1.8~2	2.3~2.7	2.7~3.4	4~4.6		5.8~6.3
3	0.5	1~1.2	1.7~2.1		2.7~3.3	4~4.2	4.9~5.2	6~6.1
4	0.5	1.3~1.4		2.3~2.7		3.7~4	4.8~5.2	5.7~6.1
Overall range	0.5~0.7	1~1.4	1.7~2.1	2.3~2.7	2.7~3.4	3.7~4.3	4.7~5.2	5.7~6.3

Table 2.6 summarizes the observed frequencies corresponding to the PSD peaks for all the signals over each segments, and also presents the overall ranges resulting from a combination of all four segments results. Table 2.7 lists the ranges of frequencies observed in the spectrum of individual acceleration and velocity signals. Both the tables show similar ranges of frequencies, while a total of eight narrow frequency bands can be observes as common ones, which are indicated by thick-bordered cells. These frequencies

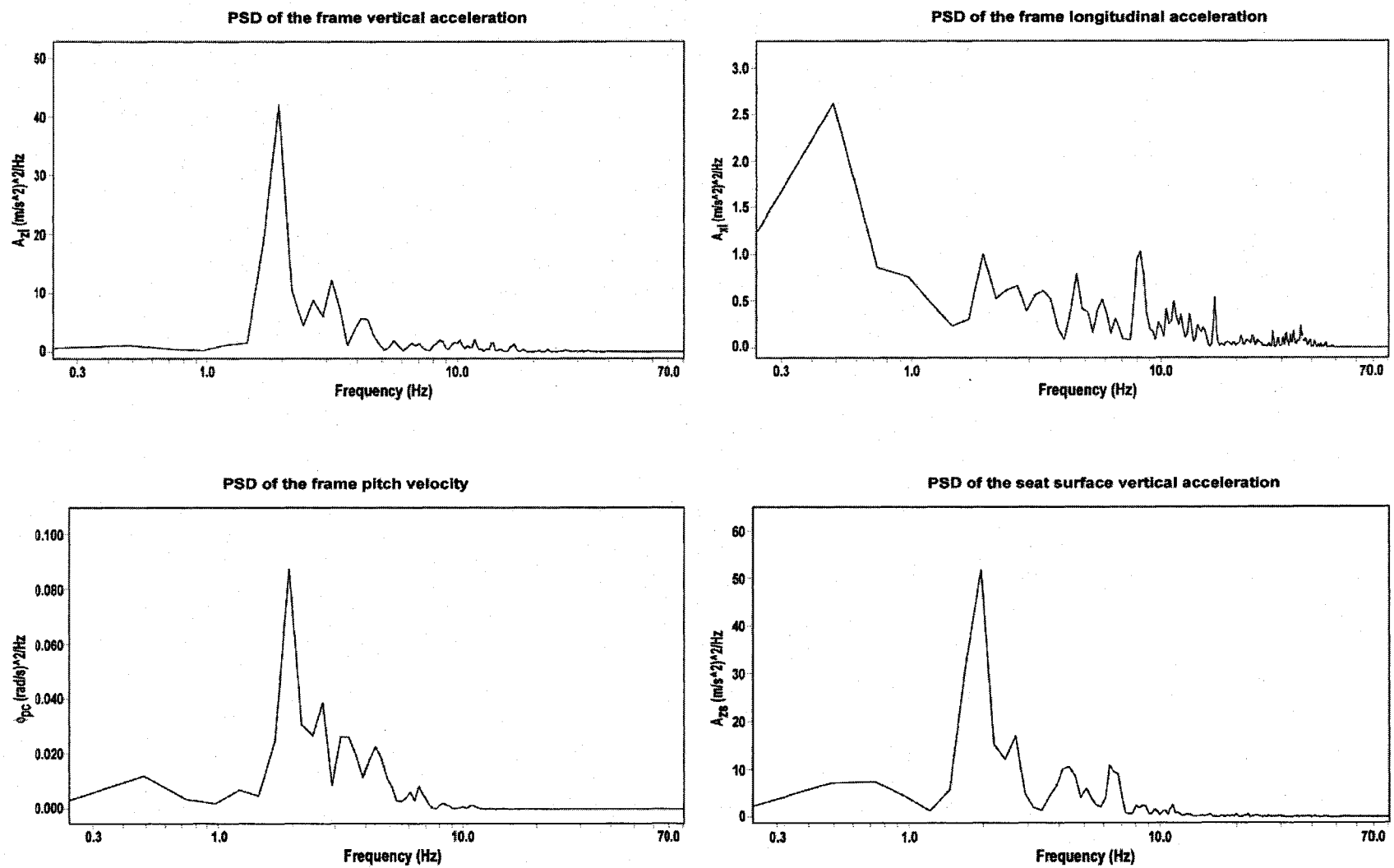

Figure 2.18: Power spectral densities of the frame and seat responses for a typical run on segment 2.

can thus be considered to represent the ranges of natural frequencies of the candidate vehicle corresponding to eight dominant deflection modes. It should be noted that the frequency ranges are identified, instead of the discrete frequencies, due to strong system non linearities and significant variations in the speed and the trail segment roughness.

Table 2.7: Frequencies of PSD peaks for each signal with all trail segments considered.

PSD	Frequency ranges corresponding to peaks (Hz)							
Azl	0.7~1		1.7~2	2.3~2.7	3~3.2	3.7~4.2	4.7~5.1	5.7~6.1
Axl	0.5		1.7~2	2.3~2.7		3.7~4.1	4.9~5.2	5.8~6.1
ϕ pc	0.5~0.7	1.2~1.4	1.7~2	2.3~2.7	3~3.3	3.8~4.3	4.9~5.2	
Azs	0.5~0.7	1~1.4	1.8~2.1	2.3~2.7		3.7~4.3	4.8~5.2	6~6.3
Overall ranges	0.5~0.8	1~1.4	1.7~2.1	2.3~2.7	3~3.3	3.7~4.3	4.7~5.2	5.7~6.3

For a given signal, the frequencies corresponding to the PSD peaks are mostly comparable for all the trail segments, while the peak magnitudes differ on different segments. The frame responses (A_{xl}, A_{zl}, ϕ_{pc}) revealed dominance near the lowest frequencies (0.5-1 Hz) when operating on the slow segment (segment 1). When operating over the medium and high speed segments, the magnitudes of second, third or fourth peaks were observed to be dominant. For instance, the dominant peaks in vertical acceleration and pitch velocity responses occurred near 0.7 Hz over segment 1, in the 1.8~2 Hz range over segment 2, and in the 3.7~4 Hz range over segment 4. This was mostly attributed to the higher speeds used on segment 2 and 4, which caused trail profile excitations at a higher frequency. The results revealed comparable frequencies of the discernable peaks, while more energy could be transmitted to the modes closest to the dominant excitation frequency. The PSD of the seat vertical acceleration response

revealed similar tendencies, although to a lesser extent. This can be attributed to the single-DOF response behaviour of the seat along the vertical axis and its tendency to attenuate higher frequency vibration. The frequency of dominant seat vibration was observed in the 2.3~2.7 Hz range, which was higher than the 1.8~2 Hz range observed for the frame vertical vibration.

The measured vibration responses are also strongly related to the braking and acceleration inputs, which tend to alter the pitch attitude and thus the suspension walking space. The frequency analyses of the data acquired over the braking and acceleration sections of the data series revealed shifts in the frequencies corresponding to the peak PSD responses. Comparison of the PSD plots of the responses preceding to the onset of braking and after it shows that, below 3 Hz, the peaks are not affected and come out at the same frequency. Above 3 Hz, however, braking induced a downward shift of the peaks in the order of 0.4 Hz.

Another interesting feature of the pure braking results is that the dominant peaks move down in frequency with an increase in mean velocity, whereas the opposite was observed in the original and pure acceleration results. Actually, this shift is not attributable to the increase in mean velocity but rather to the increase in mean deceleration. Although this had not been specified in the test protocol, the pilot instinctively adopted higher decelerations rates on faster segments, resulting in an average braking decelerations of 2.1, 2.4 and 4.3 m/s^2 over segments 1, 2 and 4, respectively. The higher decelerations caused larger pitch angle and tension in the track bottom and front strands, while the upper strand became almost "loose". The corresponding increase in the front suspension compression alone is not expected to

contribute to the decrease in the dominant peak frequency considering its relatively small rising rate. Consequently, the rear suspension deflection was believed to affect the dominant frequencies since its extension tends to alter the orientation of the rail relative to the frame allowing the rear pivot arm to come off its rear stop. The rail thus regains its full two degrees of freedom motion relative to the frame, which allows the rear suspension to follow the trail surface much better and seems to improve its ability to attenuate the higher frequency content. Accordingly, during pure braking, the mean position of the rear pivot arm relative to its rear stop was observed to be 2.05 mm over segment 1, 5.5 mm over segment 2, and 6.5 mm over segment 4. Over the same segments, the range of movement of the rear pivot arm did not increase significantly, as shown by the standard deviations of 3.2, 5.2 and 3.2 mm for segment 1, 2 and 4 respectively. As the mean distance between the rear pivot arm head and its rear stop increased from segment 1 to segment 4 while its range of motion stayed constant, the rear pivot arm must have spent less time in contact with its rear stop over segment 4 than it did over segment 1.

2.6 Summary

This second chapter presented the physical experimental work undertaken during this project. The first step consisted in defining the architecture of the simulation model to be developed in order to guide instrumentation choices and test protocol design. Collected data and results relative to trail profile measurement and characterization were then presented, including figures of some rebuilt surface profiles and a figure presenting the envelope of the spatial PSD's of the measured snowmobile trails. Data and results relative to vehicle responses over the different trail segments were finally reviewed,

looking at the time domain signals and their statistics before examining the frequency domain results.

CHAPTER 3

SYSTEM MODELING

3.1 Introduction

Following the model architecture definition and the attendant field measurements, as presented in the previous chapter, Chapter 3 details the structure of the model forming the virtual prototype. This is achieved by presenting, in sequence, all the components of the simulator. The two major components are the snowmobile model, which is the system being excited, and the snow trail model, which is the primary excitation. First reviewed is the snowmobile model, which is further divided into four subcomponents. These are the chassis and suspension model, the track model, the traction model and the driver model. The snow trail model is presented next. Lastly, the system of equations and the algorithms used within ADAMS to solve it are briefly described and explained.

3.2 Development of a Snowmobile Model

A multi-body dynamic model of the candidate vehicle is developed with the objective of assessing the ride properties and the influences of various suspension and track design parameters. The model is formulated upon development and integration of four sub-models, namely the chassis comprising the frame with suspensions, seat and drive axle, the track model and its companion the traction model, and the driver model. The sub-models and the total vehicle model are formulated in the ADAMS (Automatic Dynamic Analysis of Mechanical Systems) platform, from MSC Software Corporation. The ADAMS software is composed of several modules, where each module is dedicated to a specific type of system and/or analysis. For instance, the "Rail" module targets

guided vehicles, whereas the "Flex" module is dedicated to the analysis of flexible bodies. The development of the candidate vehicle model employed four different modules. The ADAMS/View module is the default graphical user interface that was employed for defining the different bodies and the joints for model building. This module writes the required analysis files comprising a non-linear system of equations, which are subsequently solved in the ADAMS/Solver module. The solutions are sent-back in the ADAMS/View module to compute the desired measures, while the ADAMS/Solver intervention remains transparent to the user. The user's inputs defining the connected bodies and the desired responses are thus limited to the ADAMS/View module. The ADAMS/PostProcessor module is employed for the generation of results graphs and data series using a graphical interface. Finally, ADAMS/Insight is used in chapter 5 to partly automate the creation of designed experiments and execution of their numerous simulation runs.

Various sub-models of the candidate vehicle formulated in the ADAMS/View module are described in the following subsections.

3.2.1 Chassis Model

The chassis sub-model comprises the frame, suspension, drive-axle and the seat components. All the components including links and joints of the suspension and the drive axle were modeled in CAD and exported to ADAMS/View as rigid bodies. The model included every tiny part of the suspensions, down to the screws and the washers to obtain accurate masses and mass moments of inertia of the assembled rail, linkages and skis. Figure 3.1 shows the purpose-built CAD model of the chassis and its components.

The model mass, center of mass coordinate and mass moments of inertia were adjusted such that the resulting values agreed well with those measured by BRP during development of the REV platform. The tuning of the model mass was achieved by subtracting the mass of the whole suspension, as computed in CAD, from the measured vehicle mass and also by adjusting the engine mass. A ballast was introduced to compensate for the masses due to components that were not modeled, such as body panels and lights. Tuning of the pitch mass moment of inertia was based on the available

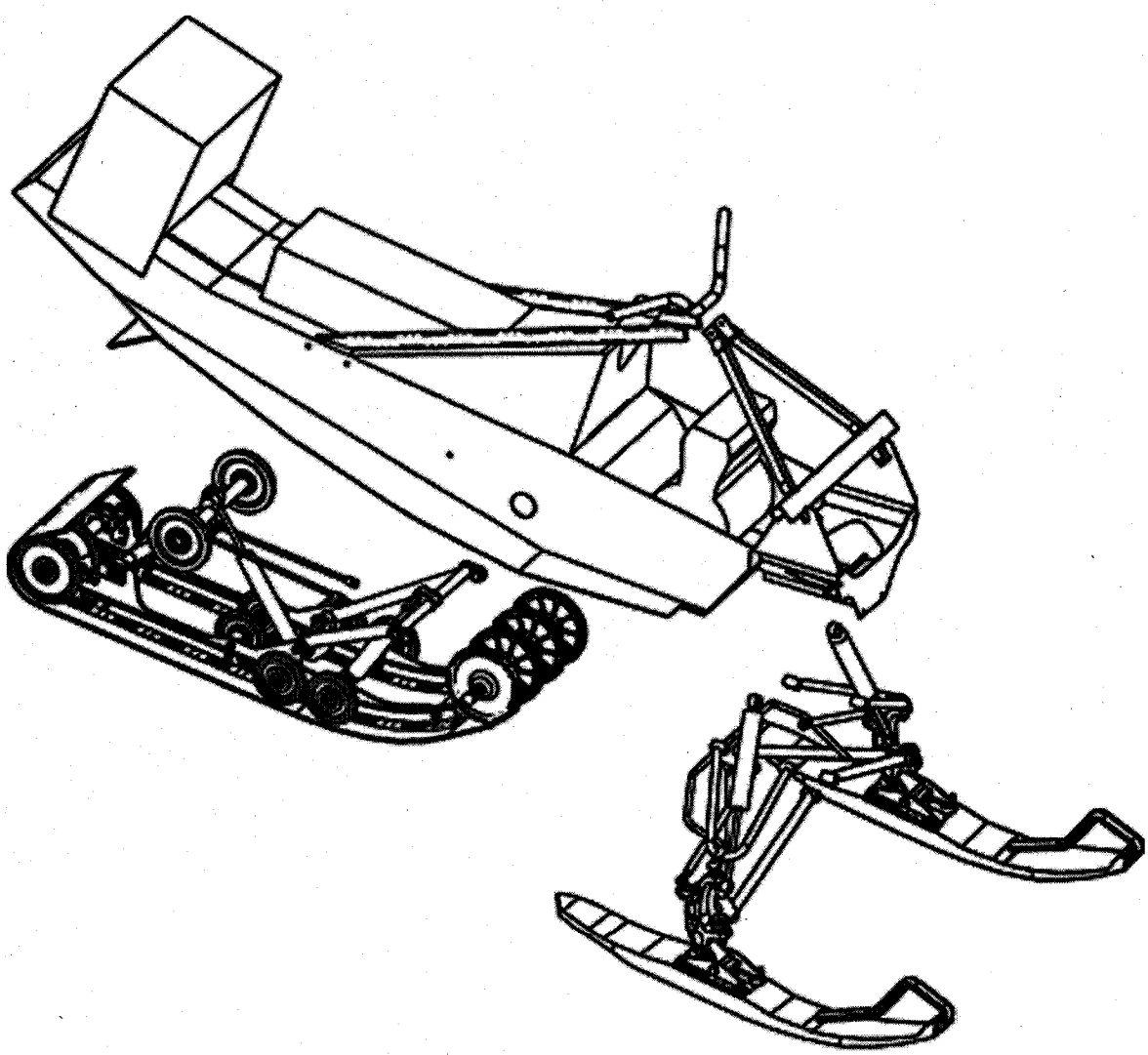

Figure 3.1: Partially exploded view of the CAD model of the snowmobile.

experimental measures of the yaw inertia, while the data on the pitch mass moment of inertia was not available. For typical snowmobiles, pitch and yaw inertia are considered to be quite comparable.

The seat is modeled as a non-linear spring damper system based on the force-deflection properties measured by BRP. Five different vertical force-deflection curves were acquired under different constant compression speeds (triangular waves) ranging from 15 to 120 mm/min. BRP originally divided the measured curves in three vertical load zones: 0 to 625 N; 625 to 1250 N; and 1250 to 1875 N in order to describe piecewise linear properties. Linear regression functions were derived to characterize the stiffness in each zone. Of the five curves, the 45 mm/min curve was chosen for inclusion in the simulation model since, in two of the three zones, it revealed stiffness values close to the average stiffness of the five curves. Moreover, the hysteresis was almost identical for the five curves. Only the mean curve, however, is used in the ADAMS model, assuming negligible hysteresis, as shown in Figure 3.2.

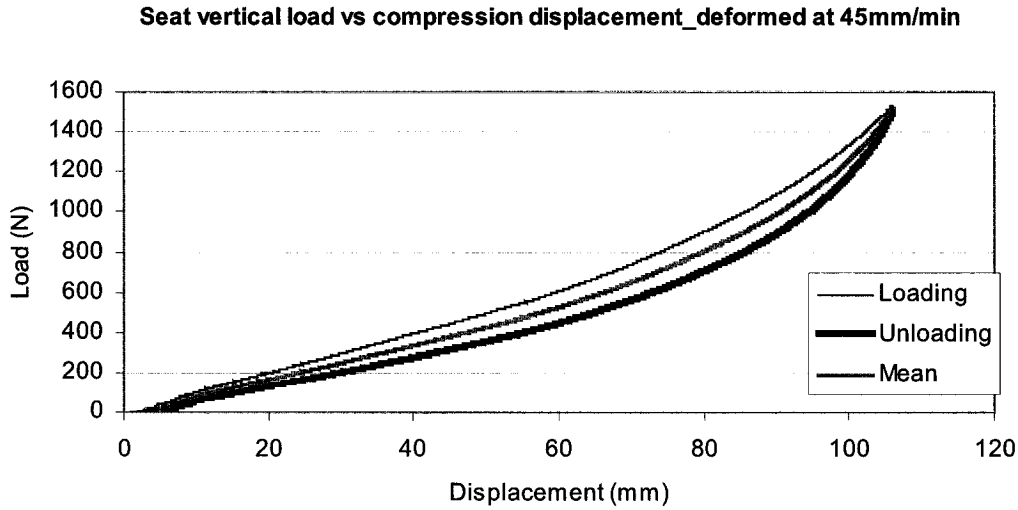

Figure 3.2: Force-deflection properties of the seat cushion.

The damping constant of a polyurethane seat is known to vary with displacement, velocity, preload, delay between the stabilization of the deformation under static compression and the onset of cycling, and with the number of cycles preceding the one used to compute damping [35, 40]. Owing to the extreme complexity of PUF behaviour, the detailed modeling of which would constitute a major project in itself, a single equivalent damping constant was selected for inclusion in the model, which was computed on the basis of energy dissipated during a loading/unloading cycle [41]. For this purpose, the force-velocity characteristics were measured under a sinusoidal excitation, and the area bounded by the hysteresis loop was computed to represent the dissipated energy E. The equivalent viscous damping C constant is then computed from:

$$C = \frac{E}{A^2 \pi \omega} \tag{3.1}$$

where A is the amplitude of cushion deflection and ω is the angular frequency of excitation.

The analysis of the data acquired by BRP under a 63.2 mm static compression, arising from a 576 N load corresponding to 70 percent of the body weight of a 83.9 kg driver, and excitations at different frequencies and amplitudes, revealed that the damping constant varied between 900 and 1000 Ns/m. The lower bound of the damping constants is used in the vehicle model.

3.2.2 Track Model

In the model development, the track mass and pitch inertia are added directly to the rail and the frame rigid bodies by associating the upper half of the track to the frame

and the lower half to the rail. This is done directly in the CAD model by splitting the track in two equal length parts, with the rear suspension in its static configuration. The upper half is then assembled in the CAD frame model and the lower half in the CAD rail model, which are then used for mass and inertia computation. This way of including the track pitch inertia in the simulation model thus neglects the variations in the geometry of the belt spans joining the drive axle to the rail and the rail to the frame; these variations are simply due to the motion of the rail relative to the frame. This approximation is justified by the significant reduction in computation effort it offers compared to a thorough inclusion of the inertial effect of each individual belt span. Only the forces and moments associated with the track rotational degree of freedom, namely the reaction forces on the guiding wheels, still need to be added.

Considering that the vehicle model is developed solely for design and assessment work with particular focus on ride characteristics, its computational efficiency is considered to be of primary importance. This justifies the use of a relatively simple piecewise track model. Models requiring intensive computational efforts, while enabling the analysis of track vibration modes, would slow down the simulation process without bringing real benefits.

Consequently, a track model inspired by that of Sandu [17] and augmented to include the tangential transient dynamics has been developed. The belt is assumed to possess infinite tangential stiffness, thereby resulting in insignificant changes in its length. In practice, the snowmobile rear suspension is designed to ensure that the belt length does not vary by more than 1% over the full suspension displacement. Consideration of an inextensible track belt, however, does not permit for computation of

the belt's radial dynamics and of the centripetal acceleration effect, as will be discussed later. This simplification, however, greatly reduces the number of model equations while including all other major phenomenon influencing suspension motion and track angular acceleration.

The track loop is divided into different segments, either straight line or circular arcs segments, as illustrated in Figure 3.3. The track tension at the ends of each segment is computed from the inertial forces generated by the considered segment and from the external forces. Assuming static equilibrium along the radial direction, the track tensions are used to compute the reaction forces applied by each arc segment to the associated supporting wheel(s). This formulation, thus, allows for consideration of the track effects without addition of rigid bodies. The ADAMS model does not include any "material" representation of the track belt itself, except for a massless extrusion covering the rail's bottom and used exclusively for ground contact computation.

Two wheels, the rail's curved leading edge and the drive axle constitute the four corners of the polygon described by the track belt and shown in Figure 3.3. For each

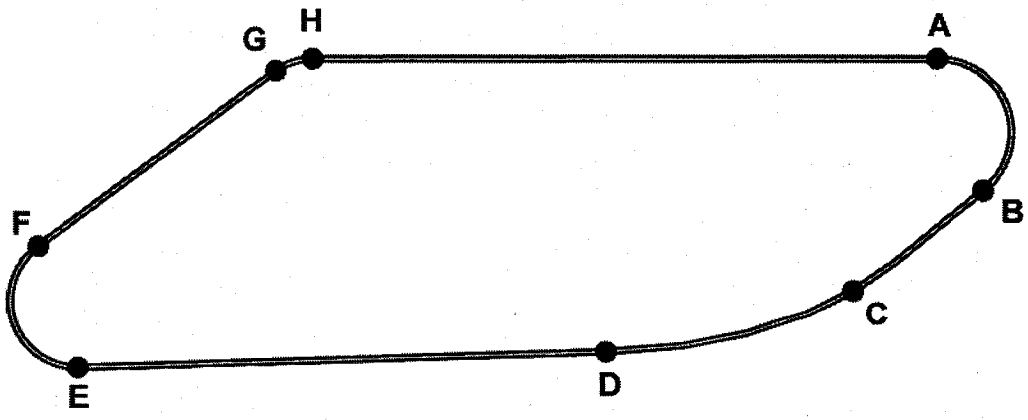

Figure 3.3: Tangency points defining the limits of the 8 track belt segments.

corner, the point of belt entry and exit delimit the corresponding arc segment. Four circular arc segments (HG, FE, DC, and BA) and four straight-line segments (AH, GF, ED, and CB) are thus defined.

The entire track model is implemented in Fortran subroutines compiled using Compaq Visual Fortran 6.0 and linked using the dedicated ADAMS command line interface, as user-defined functions. The subroutines involve the following sequence of computations for deriving the instantaneous track orientation and forces in response to the rail's position and ground contact forces:

1) compute the position of each tangency point (A to H) given the instantaneous position of the rail and express the coordinates in the frame local coordinate system.

2) compute the wrap angle of each circular arc segment, as shown in Figure 3.4.

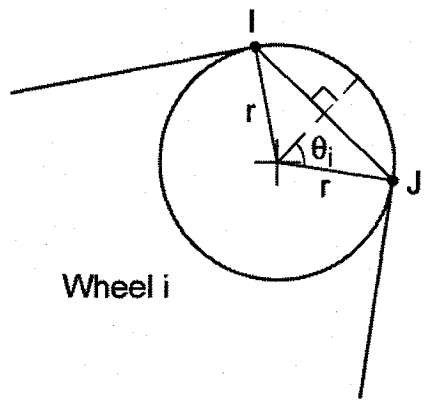

Figure 3.4: Belt wrap angle around a guiding wheel.

The wrap angle θ_i of an arc segment IJ is computed from the arc radius in the following manner:

$$\theta_i = \arcsin\left(\frac{\|IJ\|/2}{r}\right) \tag{3.2}$$

3) compute the track's instantaneous slip ratio, as described in section 3.2.3.

4) compute the traction force developed at the track-ground interface as a function of the slip ratio and normal load using the formulation described in section 3.2.3.

5) compute the friction force induced on the rail by the track rubbing action using a combination of Coulomb (μ=0.02) and velocity dependent friction components. The drag force acting on the rail was described by the following function based on the measured data and on trial and errors:

$$Df\_rail = \left[\mu + \left(c \times (1 - split) \times (\phi_{pb} \times r_b)^{D\_exp}\right)\right] \times N \tag{3.3}$$

where *Df_rail* is the drag force applied to the rail bottom by the track, *c* is the coefficient specifying the magnitude of the velocity dependent friction component, *split* designates the fraction of the friction component applied between the skis and the ground, ϕ_{pb} is the drive axle angular velocity relative to frame, r_b is the drive axle radius, *th* is the track belt thickness, *D_exp* is the velocity exponent and *N* is the ground reaction load acting normal to the rail bottom.

6) having all external forces applied along the track tangential direction, compute the drive axle angular acceleration from the following:

$$\ddot{\phi}_b = \frac{T - (Flon \times (r_b + th/2) - Df\_rail \times r_b)}{I_b + \rho \times (r_b + th/2)^2 \times L + I_4 \left(\frac{r_b}{r_4}\right)^2 + I_5 \left(\frac{r_b}{r_5}\right)^2 + I_{rail} \left(\frac{r_b}{r_{rail}}\right)^2} \tag{3.4}$$

where $\ddot{\phi}_b$ is the drive axle angular acceleration, *T* is the torque applied to the drive axle (which can be either positive or negative), *Flon* is the traction force generated by the track on ground, I_b is the polar mass moment of inertia of the drive axle alone, ρ is the track belt linear density, *L* is the belt length (assumed constant), I_4, I_5 and I_{rail} are the polar mass moments of inertia of the group of wheels number 4 (EF on Figure 3.3) and 5 (GH on Figure 3.3) and of the wheels of the rail's central section (see Figure 2.5), respectively. Similarly, r_4, r_5 and r_{rail} are the radii of the wheels 4, 5, and that of the rail's central section, respectively.

7) compute the tension components due to track rotational dynamics at each tangency point (A to H) from the external and inertial forces. As an example, the equations for the tensions at points H and G can be derived from:

$$T_h = T_a - \rho \|AH\| (r_b + th/2) \ddot{\phi}_b \tag{3.5}$$

$$T_g = T_h - 2\rho(r_5 + th/2)\theta_5(r_b + th/2)\ddot{\phi}_b + I_5\left(\frac{r_b}{r_5^2}\right)\ddot{\phi}_b \qquad (3.6)$$

where T_a, T_h and T_g are the transient components of the tangential forces acting at points A, H and G, respectively. $||AH||$ is the length of segment AH. From the above equation, it is apparent that computation of the tangential force at one end of a given segment requires that the tension at the other end be known. For instance, T_a is required to compute T_h. Computing T_a in turn requires knowledge of T_b. Since $\ddot{\phi}_b$ is computed by dividing the sum of all applied torques by the sum of the polar moments of inertia of all rotating parts, only one of T_a or T_b can be positive at any given time, the other necessarily being nil. This is evidenced by rearranging equation 3.4 as follows:

$$T - (Flon \times (r_b + th/2) - Df\_rail \times r_b)$$
$$-\ddot{\phi}_b\left(I_b + \rho \times (r_b + th/2)^2 \times L + I_4\left(\frac{r_b}{r_4}\right)^2 + I_5\left(\frac{r_b}{r_5}\right)^2 + I_{rail}\left(\frac{r_b}{r_{rail}}\right)^2\right) = 0 \qquad (3.7)$$

Equation 3.7 says that the drive torque T is first consumed by the rail friction (*Df_rail*) and the propulsive force (*Flon*) and that whatever torque is left is then *entirely* consumed in accelerating the rotating parts. Since the drive torque is applied to the belt over the arc defined by points AB *exclusively*, the infinitesimally long element of belt at one of these two points is the "last pulled belt element". The term $\rho(r_b+th/2)^2L$ being the equivalent polar moment of inertia at the drive axle of the *entire* belt, all the torque has been consumed once the "last pulled belt element" is reached. Tension at that point is therefore necessarily nil. As the starting point can be either A or B, two equation sets are used to compute the tensions, one starting with $T_b = 0$ and going toward T_a, T_h and so on and the other set starting with $T_a=0$ and going the other way around. Only one set is active at a time, according to the sign of the following "switch" variable:

$$Tswitch = \left(|T| - |Flon(r_b + th/2) - Df\_rail \times r_b|\right) \times sign\left(\ddot{\phi}_b\right) \qquad (3.8)$$

which is positive whenever the track upper span (AH) is being pulled toward point A and negative whenever it is being pulled toward point H. Considering that the right hand side of equation 3.8 is made up of two terms, the first one being $(|T|-|Flon(r_b+th/2)-Df\_rail*r_b|)$, hereafter called the "torque balance", four different combinations are possible. When both terms are positive, the driver is obviously asking for forward acceleration. The opposite is just as easily understood; both terms are negative under braking. The combination of negative torque balance and positive angular acceleration arises when the vehicle lands (after jumping over a small bump, for example) while trying to

brake at high longitudinal velocity. While airborne, the track rotation is slowed down by the applied braking torque and, upon ground contact, the slip ratio adopts a high negative value, which generates a high braking force that in turn accelerates the track's rotation. Lastly, the combination of positive torque balance and negative angular acceleration arises when the vehicle lands with the throttle significantly opened. Upon ground contact, the slip ratio adopts a very high value, inducing a high propulsive force that can slow down the track rotation even though the drive-torque remained positive.

8) compute the normal reaction forces applied to each circular arc segment in that arc's local frame of reference.

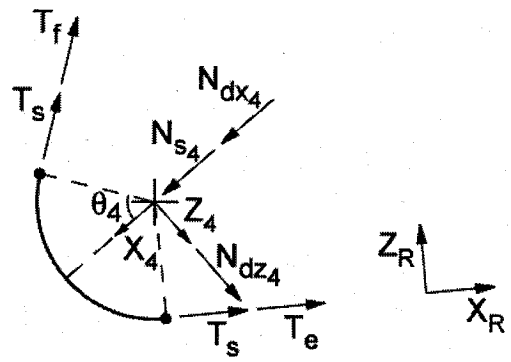

Figure 3.5: Free body diagram depicting forces acting on wheel 4

As an example, Figure 3.5 shows the free body diagram of the belt arc wrapped around wheel 4. The local X-axis points outward from the axle and passes through the arc's center. Following right hand rule, the Y-axis points toward the left side of the vehicle. T_s is the static tension (pretension) and N_{s4} is the radial force it generates. N_{dx4} and N_{dz4} are the reaction force components due to transient tension components T_e and T_f. The frame (X_R,Z_R) defines the rail local coordinate system. The equations of equilibrium are as follows:

$$N_{s4} = 2 \times T_s \times \sin(\theta_4) \tag{3.9}$$

$$N_{dz4} = (T_f - T_e)\cos(\theta_4) \tag{3.10}$$

$$N_{dx4} = \left|T_e + T_f\right| \sin(\theta_4) \tag{3.11}$$

9) compute the total wheel reaction forces (F_{ix}, F_{iz}) acting on wheel i using equations (3.9) to (3.11), or corresponding ones for the three other arcs. Then project the result along the coordinate system of the body on which the arc segment acts; it is either the rail (as for wheel 4) or the frame. Given that belt segments AH and DE are respectively parallel to the X-axis of the frame and of

the guide rail (Figure 3.5), the projections can be made directly using the wrapping angles θ_i. Again, using wheel 4 as an example, one gets:

$$F_{4x} = (N_{s4} + N_{dx4})\sin(\theta_4) - N_{dz4} \times \cos(\theta_4) \tag{3.12}$$

$$F_{4z} = (N_{s4} + N_{dx4})\cos(\theta_4) + N_{dz4} \times \sin(\theta_4) \tag{3.13}$$

The above equations define the forces associated with wheels 4. The force components developed at the other wheels are computed in a similar manner and different subroutines are developed for each wheel and arc segment. Each subroutine returns three components of a force vector, where the Y component is zero.

This procedure was initially carried out within the ADAMS/View module using "state variable expressions". That, however, made the solver suffer from occasional instabilities most likely due to difficulties in sequencing the various computational stages. The MSC software support and users-forum were not able to identify the cause of this instability problem and thus could not recommend a precise solution. Defining the track model by an independent subroutine not only solved the issue but also provided full control over the exact computation sequence, although at the cost of increasing the modeler's workload.

The above algorithms and corresponding subroutines yield the belt arc segments reaction forces only. Additional subroutines are developed to pilot the ADAMS force generating elements applying the track drag friction force on the rail's bottom and the resistive torque load on the drive axle. This resistive torque comes from the traction and track friction forces. The drag is computed using equation (3.3) and is applied along the X-axis in the rail bottom plane, thus pointing forward. The Y and Z force components are considered as nil.

An independent subroutine is further developed to compute the torque load applied directly to the drive axle using a torque generating element. It is computed from the following equation:

$$T\_ext = -Flon(r_b + th/2) + Df\_rail \times r_b \tag{3.14}$$

where T_ext is the torque load due to the external resistive forces applied to the track belt. It should be noted that the inertial forces due to track belt and supporting wheels angular accelerations have already been accounted for in the ADAMS model. As mentioned earlier, the equivalent polar mass moment of inertia of the track belt is lumped with that of the drive axle, while the different wheels are connected to the drive axle using "connector elements". This no-slip condition is assumed by ensuring that the various wheels peripheral velocity remains identical to that of the drive axle. This no-slip assumption is not verified for wheels 5 at very high speeds and for rail wheels while airborne. These wheels, however, represent only 4% of the total drive train rotational inertia, and the slippage is believed to occur only under the aforementioned conditions. The no-slip assumption is thus considered to be reasonable and is not expected to yield significant discrepancies between the simulated and measured behaviour.

Owing to the assumed infinite tangential stiffness of the track, a segment between any two arcs remains straight, while the wrapping angles remain constant for a given suspension deflection, irrespective of the track belt velocity. In practice, however, the centrifugal force developed at each corner causes elongation of the belt due to its finite stiffness. This causes the track to sag and assume an arched shape over the initially straight segments, and thus generate a centrifugal force. Moreover, the belt also possesses finite bending stiffness, which further enhances the curvature and reduces the wrapping

angles around their adjacent wheels. The reduction in wrapping angle at a given corner directly reduces the tension induced at the corresponding tangency points by the centrifugal acceleration. The belt tension then tends to equalize over the loop, which hence tends to adopt a circular shape. It is thus observed that the consideration of centrifugal acceleration is incompatible with the assumption of infinite tangential stiffness of the track. In fact, computing centrifugal acceleration while maintaining belt length constant, thereby forcing the belt segments between two successive wheels to remain straight, the arcs AB and EF (see Figure 3.3) are found to induce significantly more tension than do the two others. This causes the track segment AH to accelerate toward point A, while segment FG accelerates in the opposite direction, i.e. toward point F. This is, of course, impossible unless the belt has finite tangential stiffness, which directly contradicts the initial assumption. It is thus concluded that the centrifugal acceleration of the various track belt spans cannot be considered when the track length is assumed to remain constant.

3.2.3 Traction Model

The traction forces developed at the track-ground interface are defined as a function of the slip ratio and the normal load acting on the rail, resulting in a quasi-steady type of model. The slip ratio, also referred to as longitudinal slip, has been generally defined for tires [42,19]. The track slip ratio is defined as [42]:

$$\gamma = \frac{\phi_{pb} * r_b - Vx}{Vx} \tag{3.15}$$

where γ is the non-dimensional slip ratio, ϕ_{pb} is the angular velocity of the drive axle, r_b is the drive axle radius measured from the center line of the track (along its thickness) wrapped around the drive axle and Vx is the instantaneous frame velocity along its local X-axis.

Six of the eight tire models available within the ADAMS/Tire module, version 2005, also utilize the above definition for the slip ratio [43]. The slip ratio may approach an infinite value when the throttle is opened suddenly, while the vehicle is stationary. The ADAMS tire models thus impose a limiting value of +1. This limiting value is based on the fact that, for typical tires, the longitudinal force is nearly stabilized before γ reaches a unity value and remains almost constant for $\gamma>1$. For the track, however, the value of γ past which the longitudinal force stabilizes is unknown. The field measured data revealed frequent occurrences of high track slip ratio. During the first tenths of a second of high acceleration from standstill, the slip ratio exceeded +7.0 several times, but stayed under that value for the rest of the run. A limiting value of +7 was thus selected in this study. Under hard braking with track lock-up, equation (3.15) returns a value of –1 for the slip ratio. The value, however, is indeterminate under zero longitudinal and angular velocities. Since the vehicle is considered to be stationary when both angular and longitudinal velocities are zero, the slip ratio is set to zero in such cases.

The longitudinal thrust applied to the vehicle by the track's ground reaction force is approximated from the field-measured drive axle torque and the effective track radius, which yields the tangential tension force in the track belt. An inertial correction is applied by subtracting the approximate track inertial force from the tangential force to compute the thrust force. The inertial force is computed using an approximation of the drive axle

angular acceleration obtained by differentiating the angular velocity signal and filtering it using a 40 points moving average kernel.

The normal reaction force applied by the ground to the rail is also approximated using the ADAMS model, with the springs and dampers adjusted to the experimentally measured stiffness and damping constants. For this purpose, the frame is fixed in space, high above ground, and the field-recorded displacement responses of the center damper and rear pivot arm potentiometer are used as inputs to the motion generators, installed in parallel to the center damper and rear potentiometer, respectively. A kinematic analysis is then performed to reproduce the experimental movement of the rail with respect to the frame, thus enabling the recording of the rail movement (vertical rail CM displacement and rail pitch) relative to the ground. These displacement responses are then used as inputs to two additional motion generators, acting at the rail CM, while the motion generators used in the previous step are deactivated, that is, they are no longer included in the system of DAE equations to be solved. The rail motion is then reproduced once more, this time by the forces imposed on the rail by the new ground-supported motion generators. The projection of the force applied by the vertical (global Z) motion generator along the rail local Z axis is then taken as the approximate rail normal load to be used in the traction model.

The longitudinal force, slip ratio and the rail normal force responses are analyzed to derive a relationship among the three signals. Figure 3.6 illustrated the variations in the longitudinal force with slip ratio and normal load. A similar surface plot was generated for each recorded run and the surfaces obtained from different runs were combined to derive an overall traction model. This approach, however, required the sampling of all the

runs for the slip ratio and the normal load signals using the same "bins". The outliers in the normal force signal were removed by saturating the signal's domain to 10000 N before dividing it into 80 bins. The –1 to 7 slip ratio domain was divided into 40 bins in a similar manner. The thrust force surface was then created for each run. These were subsequently merged together by considering the means of the non-zero values of the 3200 longitudinal force cells (80 x 40 = 3200). A regression equation was then fitted to the resulting combined surface using a trial and error approach. Two different equations relating the longitudinal force to the slip ratio and the normal load were derived corresponding to the positive and negative slip ratio. These relationship are expressed as:

$$Flon = \begin{cases} 0.5\left(\frac{5000}{1+e^{-6\gamma}} - 2500 - 111.5\gamma\right) \times \left(1 - e^{\frac{-Nl}{150}}\right) \Rightarrow \gamma < 0 \\ 1.4\left(\frac{5200}{1+e^{-9\gamma}} - 2600 - 111.5\gamma\right) \times \left(\frac{1}{1+e^{-0.005(Nl-800)}}\right) \Rightarrow \gamma \geq 0 \end{cases} \quad (3.16)$$

where the longitudinal force, *Flon*, is in N, γ is the non dimensional slip-ratio and *Nl* is the normal load in N.

Figure 3.6 illustrates the surface plots of the measured and modelled longitudinal forces developed as a function of the slip ratio and the normal load. The variations in the force with slip ratio and those with the normal load are presented separately in Figure 3.7.

The derived function ensures continuity in the longitudinal force near zero slip ratio; the corresponding longitudinal force approaches zero, irrespective of the normal load. On the other hand, the equation returns a small residual longitudinal force under zero normal load when the slip ratio is positive. This value approaches its maximum of 63 N at γ=0.75. It was judged that this small discrepancy did not mandate the use of a

more complex equation since the normal load rarely approaches zero and, when it does, it is only for very short periods of time. Moreover, when the track is airborne the slip ratio tends to vary smoothly and not jump between positive and negative values, which minimizes the risk of inducing longitudinal thrust impulses arising from the small residual force under positive slip ratio.

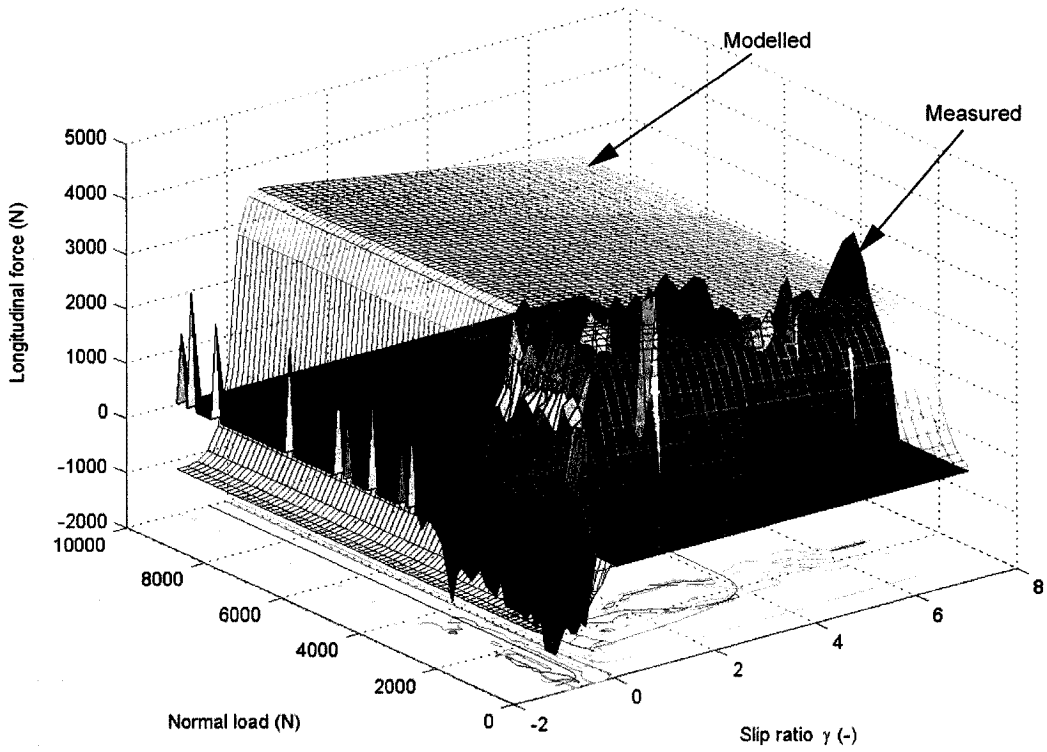

Figure 3.6: Comparison of the measured and modelled longitudinal force of the track as a function of the normal load and the slip ratio.

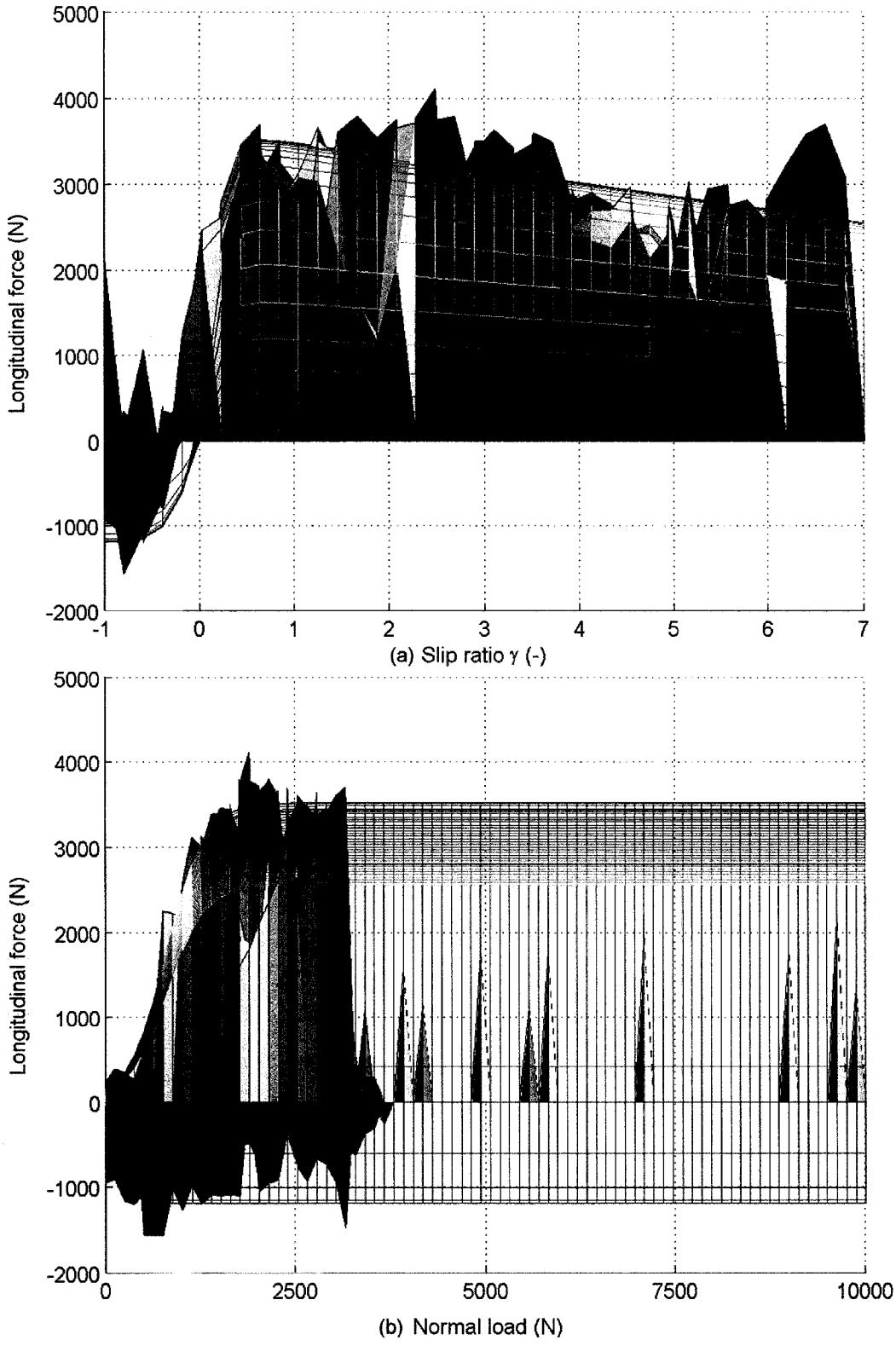

Figure 3.7: Variation in the track longitudinal force with (a) slip ratio; and (b) normal force.

3.2.4 Driver Model

Starting with a commercially available human body CAD library, a 50th percentile male dummy was tuned to have the same mass as the test driver. Upon tuning for the mass properties, the dummy was assembled in a riding position within the complete system model. For this purpose, the different limbs were exported to and reassembled in ADAMS/View using a combination of revolute, planar, universal (Hooke) and spherical joints. Joints were arranged so that the torso is free to translate along the frame's local X and Z- axes and to rotate about its Y-axis, while preventing other translation and rotations. Achieving this without creating redundant constraints required using different types of joint for the right and the left forearms, resulting in the arrangement presented in Figure 3.8. The joints between wrists and ankles are connected to the vehicle frame, which is not shown on the figure for clarity.

A force element was then added between the driver's buttock and the frame rigid body to represent the dynamic interactions between the two. This element was made up of three discernable components: (i) the seat stiffness and damping elements along the Z-axis of the frame; (ii) the friction between the driver suit and the seat cover; and (iii) the seat cover longitudinal elasticity. The last two components were configured to act along the frame X-axis. The friction coefficient and the longitudinal elasticity were adjusted by trial and error to attain reasonable driver motion in a qualitative manner, while the seat stiffness and damping constants were obtained from the measured data, as described in section 3.2.1. A slider-type joint was then added between the torso and the frame so that the former may move only along the latter's Z-axis. This joint can be turned off whenever the torso's longitudinal and pitch motions are desired. The chosen values of seat

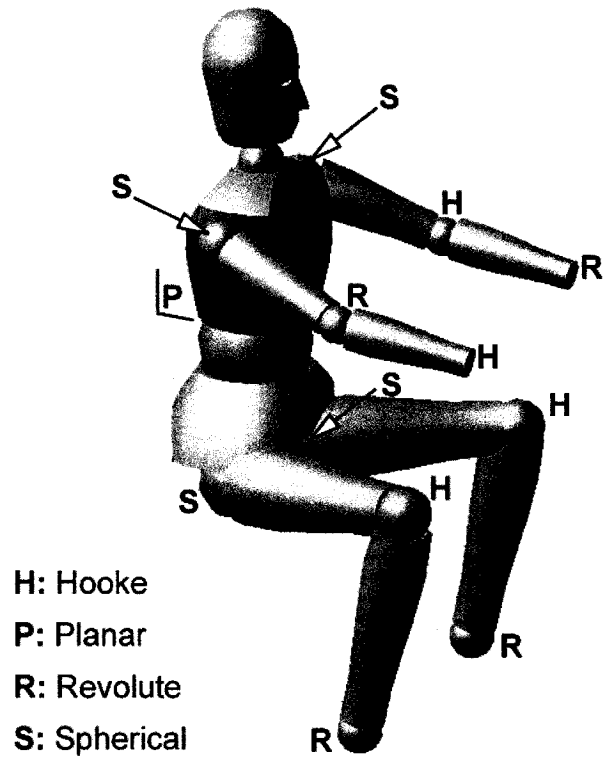

Figure 3.8: Arrangement of the driver body joints allowing longitudinal, bounce and pitch motion of the torso relative to the vehicle frame.

longitudinal stiffness and friction allow only little fore-aft movement of the driver's buttock, just enough for the torso's vertical motion to look natural and not severely over constrained.

3.3 Snow Trail Model

The dynamic responses of the snowmobile strongly depend upon the dynamic interactions between the track and the snow trail, and the skis and the snow trail. A realistic simulation model must incorporate the loss of contact between the skis and the ground, and the rail and ground, which occur quite frequently in normal operation. A contact detection and force computation algorithm is thus required to simulate the ski-to-ground and rail-to-ground interfaces. In a multi-body system simulation environment, such as ADAMS, the easiest way to accomplish this is to represent both contacting parts

as rigid bodies and link them through a so-called "contact element", which is an object oriented implementation of a contact detection and force computation algorithm. The surface profiles of each of the four measured trail segments were therefore imported in ADAMS and used as a sweeping path along which a rectangular section was extruded, resulting in 2 meters wide and 30 cm thick strips. The upper surface of these strips replicates the four measured trail segment profile. As contact management involves intensive computation, it is essential to use a highly efficient algorithm in the iterative development process. Therefore, instead of applying the dedicated algorithm used by Khan *et al* [14] on the basis of Bekker's empirical formulations, the contact element available within ADAMS was tried. This approach provided reasonably good results, although the simulation of 1s of vehicle operation could take up to several hours. The chosen algorithm, called the "Impact function model" is based on a penalty function approach. The boundary constraints are enforced by applying forces along the constraint gradient, where the magnitude of the forces are computed as a function of the constrain violation [44]. With g being the gap between the contacting bodies (g>0 when penetration occurs) and F_n being the contact force (F_n>0 when the bodies tend to separate), the constraint equation is expressed as:

$$F_n = k(g^e) + Step(g,0,0,d_{\max},c_{\max})\frac{dg}{dt} \tag{3.17}$$

where the first term relates to the contribution due to the stiffness and the second term relates to the damping properties of the contact. The constant k represents the overall contact stiffness while e is an exponent of the gap g. The term $Step(g, 0, 0, d_{max}, c_{max})$ is a call to an internal ADAMS/Solver function, having syntax $Step(x, x_0, h_0, x_1, h_1)$, creating

a smoothened approximation of the Heaviside step. In this syntax, x is the independent variable passed to the *Step* function for evaluation at runtime. As long as the value of x is lower than x_0, the function returns value h_0. When x is greater than x_1, *Step* returns h_1; for $x_0 < x < x_1$, the output is computed using the smoothened step approximation. Consequently, d_{max} is the penetration value past which the maximum damping c_{max} is applied. Referring to equation (1.1) in section 1.2.2, it can be seen that the stiffness term has the same form as the Reece pressure-sinkage equation. However, the energy dissipation associated with the plastic deformation of the snow/ice is not considered, while a viscous damping coefficient is assumed.

In an effort to enhance the speed of computation, several values of contact stiffness and non-linear damping constants were attempted starting with the baseline values chosen to provide static sinkages of 6mm at the track and 12 mm at the skis. Moreover, the baseline values were chosen to yield an overdamped behaviour upon passing over a bump. Using a similar iterative process, the resolution of the trail profile, and the number of facets within the ski and the track bottom plates were identified to minimize the computation time, while keeping sufficient shape accuracy. The process resulted in the adoption of a 10 cm pitch for the trail profile points and non-uniform spacing of contact points at the track and ski bottoms. Eventually, the model was migrated from ADAMS version 12.0 to version 2003 with its significantly improved contact algorithm, which resulted in considerable reduction of computation time, by up to 20 fold, and also increased numerical stability. These further motivated the usage of the available contact algorithm instead of using a custom-defined algorithm based on Bekker's equations.

3.4 Method of Solution

The multibody dynamic model of the snowmobile is solved in the ADAMS platform, which yields the position and orientation of each of its rigid body as a function of time. The position and orientation are computed in terms of variables, referred to as "generalized coordinates". The position coordinate of a rigid body is defined by a column vector of three global Cartesian coordinates [45]:

$$\mathbf{p} = \begin{bmatrix} x \\ y \\ z \end{bmatrix} \tag{3.18}$$

Similarly, orientation of the body-fixed (or local) coordinate frame is defined by three Euler angles corresponding to the 3-1-3 sequence, that is first rotation (ψ) about the Z-axis (3rd axis), second rotation (θ) around the X-axis (1st axis) and third rotation (ϕ) around the Z-axis (3rd axis) [46], hence the 3-1-3 designation. Orientation is thus given by the following column array [45]:

$$\boldsymbol{\varepsilon} = \begin{bmatrix} \psi \\ \phi \\ \theta \end{bmatrix} \tag{3.19}$$

Note that this being an array and not a vector, the relative order of the angles within it does not matter as long as it is kept constant throughout the whole process. The ADAMS/Solver utilizes Euler angles despite their singular configuration at θ=0 [45] and hence does not revert to singularity free four-terms representations (quaternions, Rodriguez parameters, etc.) [26]. Instead, upon approaching a singular configuration, the affected local coordinate frame is reoriented relative to its rigid body.

The motion of a rigid body i is thus defined by the following set of generalized coordinates:

$$\mathbf{q}_i = \begin{bmatrix} \mathbf{p}_i \\ \boldsymbol{\varepsilon}_i \end{bmatrix} \tag{3.20}$$

The time derivatives of the motion array defines the translation and rotation velocities such that:

$$\mathbf{u} = \dot{\mathbf{p}} \tag{3.21}$$

$$\overline{\boldsymbol{\omega}} = \mathbf{B}\dot{\boldsymbol{\varepsilon}} = \mathbf{B}\boldsymbol{\zeta} \tag{3.22}$$

where $\overline{\boldsymbol{\omega}}$ is the angular velocity vector in the body-fixed coordinate system and **B** is the transformation matrix [26] projecting the local frame along the axes of the inertial coordinate system .

In mechanisms, the relative positions and orientations of various bodies are constrained by the use of joints. These are mathematically represented by simple algebraic functions of the generalized coordinates, namely the "constraint equations". The constrain equations are generally expressed in the form [45]:

$$\boldsymbol{\Phi}(\mathbf{q}) = 0 \tag{3.23}$$

The joints also induce dependence among the velocities and accelerations of the bodies, which are simply represented by the first and second time derivatives of equation (3.23) resulting in two additional constraint equations:

$$\boldsymbol{\Phi}_{\mathbf{q}}\dot{\mathbf{q}} = 0 \tag{3.24}$$

$$\boldsymbol{\Phi}_{\mathbf{q}}\ddot{\mathbf{q}} = -(\boldsymbol{\Phi}_{\mathbf{q}}\dot{\mathbf{q}})_{\mathbf{q}}\dot{\mathbf{q}} \tag{3.25}$$

where $\mathbf{\Phi_q}$ is the matrix of partial derivatives of equation (3.23) relative to the generalized coordinates, also known as the constraint Jacobian matrix.

Some constraints may also impose a prescribed motion (change of configuration over time) of the mechanism resulting in the position vector becoming a function of time:

$$\mathbf{\Phi}(\mathbf{q},t) = 0 \tag{3.26}$$

The velocity and acceleration constraint equations can thus be expressed as:

$$\mathbf{\Phi}_\mathbf{q}(\mathbf{q},t)\cdot\dot{\mathbf{q}} = -\mathbf{\Phi}_t(\mathbf{q},t) \tag{3.27}$$

$$\mathbf{\Phi}_\mathbf{q}(\mathbf{q},t)\cdot\ddot{\mathbf{q}} = -(\mathbf{\Phi}_\mathbf{q}\dot{\mathbf{q}})_\mathbf{q}\dot{\mathbf{q}} - 2\mathbf{\Phi}_{\mathbf{q}t}\dot{\mathbf{q}} - \mathbf{\Phi}_{tt}(\mathbf{q},t) \tag{3.28}$$

The equations of motion are obtained using the Euler-Lagrange formulation instead of the Newton's second law of motion and Euler's equations for rotation because the former method yields more systematic formulation for development of a generalized algorithm applicable to any mechanism. The Euler-Lagrange formulation is based upon the change in kinetic energy resulting from the applied constraints and external forces [46], such that:

$$\frac{d}{dt}\left[\left(\frac{\partial K}{\partial \dot{\mathbf{q}}}\right)^T\right] - \left(\frac{\partial K}{\partial \mathbf{q}}\right)^T + \mathbf{\Phi}_\mathbf{q}^T\boldsymbol{\lambda} = \mathbf{Q} \tag{3.29}$$

where K is the kinetic energy, $\mathbf{Q}$ is the vector of generalized forces, including any field forces (i.e. potential energy), which are the projection of the external forces and moments along the generalized coordinates, superscript "T" is the transpose operator and $\boldsymbol{\lambda}$ is the array of Lagrange multipliers. The kinetic energy of the system is derived as:

$$K = \frac{1}{2}\mathbf{u}^T\mathbf{M}\mathbf{u} + \frac{1}{2}\bar{\boldsymbol{\omega}}^T\bar{\mathbf{J}}\bar{\boldsymbol{\omega}} \tag{3.30}$$

where $\mathbf{M}$ is the generalized mass matrix (apparent mass along the translation generalized coordinates) and $\bar{\mathbf{J}}$ is the generalized inertia matrix expressed in the body-fixed coordinate system.

The first two terms in equation (3.29) represent the inertia forces due to accelerations along the generalized coordinates, as well as to the velocity cross terms, such as Corriolis acceleration. The third term comprising the product of the constraint Jacobian matrix and the Lagrange multipliers constitutes the constraint forces. Using the translation and rotation partitioning, equation (3.29) is rewritten as:

$$\frac{d}{dt}\begin{bmatrix}\left(\frac{\partial K}{\partial \mathbf{u}}\right)^T \\ \left(\frac{\partial K}{\partial \boldsymbol{\zeta}}\right)^T\end{bmatrix} - \begin{bmatrix}\left(\frac{\partial K}{\partial \mathbf{p}}\right)^T \\ \left(\frac{\partial K}{\partial \boldsymbol{\varepsilon}}\right)^T\end{bmatrix} + \begin{bmatrix}\boldsymbol{\Phi}_{\mathbf{p}}^T\boldsymbol{\lambda} \\ \boldsymbol{\Phi}_{\boldsymbol{\varepsilon}}^T\boldsymbol{\lambda}\end{bmatrix} = \begin{bmatrix}\left(\prod^{\mathbf{P}}\right)^T\mathbf{f} \\ \left(\prod^{\mathbf{R}}\right)^T\bar{\mathbf{n}}\end{bmatrix} \tag{3.31}$$

where the right hand side is simply the partitioned equivalent of $\mathbf{Q}$. Nothing that:

$$\frac{d}{dt}\left(\frac{\partial K}{\partial \mathbf{u}}\right)^T = \mathbf{M}\dot{\mathbf{u}} \tag{3.32}$$

$$\left(\frac{\partial K}{\partial \mathbf{p}}\right)^T = \mathbf{0} \tag{3.33}$$

and naming angular momentum as follows:

$$\Gamma \equiv \frac{\partial K}{\partial \boldsymbol{\zeta}} = \mathbf{B}^T\bar{\mathbf{J}}\mathbf{B}\boldsymbol{\zeta} \tag{3.34}$$

Equation (3.31) reduces to yield the equations of motion in the following form:

$$\begin{aligned} \mathbf{M}\dot{\mathbf{u}} + \boldsymbol{\Phi}_{\mathbf{p}}^{T}\boldsymbol{\lambda} &= \left(\prod^{\mathbf{P}}\right)^{T}\mathbf{f} \\ \dot{\boldsymbol{\Gamma}} - \frac{\partial K}{\partial \boldsymbol{\varepsilon}} + \boldsymbol{\Phi}_{\boldsymbol{\varepsilon}}^{T}\boldsymbol{\lambda} &= \left(\prod^{\mathbf{R}}\right)^{T}\bar{\mathbf{n}} \end{aligned} \tag{3.35}$$

Equation (3.35) along with equations (3.21), (3.22) and (3.34) forms a system of first order differential equations to which the algebraic equations (3.26) to (3.28) must be added to enforce the constraints, resulting in a set of differential-algebraic equations (DAE). The system of equations is solved to simulate the dynamic responses of the system.

3.5 Summary

The snowmobile model is developed, through integration of four sub-models involving the chassis, the track, the traction force and the driver representation. Representation of the ground profile as well as ski-to-ground and track-to-ground contact characteristics were described and their mathematical formulations are presented in details. The method of solution is described on the basis of the ADAMS/Solver module internal workings. In the next chapter, the dynamic response characteristics of the model under different operating conditions are compared to the recorded responses of the candidate vehicle so as to evaluate the model's validity.

CHAPTER 4

MODEL VALIDATION

4.1 Introduction

With the model fully assembled, its ability to accurately reproduce the physical behaviour of the system must be assessed before any analysis or design work can be conducted through simulation. The model validity is thus examined under both static and dynamic conditions using the laboratory as well as field measured data.

The static response characteristics of the model can be conveniently examined prior to the dynamic response analyses, thus providing a first level validation of the model. This involves comparisons of model outputs with the laboratory measured data in terms of suspension deflection and weight distribution when the vehicle rests on level ground. Consequently, the laboratory test protocols and measurement methods are presented together with the static simulation results.

The validity of the dynamic response characteristics of the model may be examined under different excitation conditions using various response measures. The model validity could be best examined in terms of absolute motions of the sprung and unsprung masses, and relative deflections of the two masses. In the case of a snowmobile, these would translate to frame motions and suspension deflections. The fundamental bounce and pitch frequencies would form other vital measures for demonstrating the model validity.

In this chapter, the field measured data are used to examine the validity of the dynamic responses of the model in terms of frame motions, suspension deflections,

natural frequencies and frequency response characteristics. The results show that the model outputs follow the trends that are evident in the measured data, while considerable deviations exist in the magnitudes of the response variables. Such deviations are attributed in-part to the lack of controlled experimental conditions and in-part to the various modeling simplifications.

4.2 Static Response Characteristics

A laboratory test program was undertaken to measure the static responses of the vehicle placed on level ground. The weight distribution of the candidate vehicle was measured in the laboratory using a test rig developed by BRP to aid in damper calibration. The test rig comprises a rigid steel platform. Two rails, each made of two parallel linear bearing guides, are mounted on the platform perpendicular to each other in a "T" configuration. Each rail supports two sliding blocks, each equipped with a shear type load cell. The snowmobile was positioned on the platform such that a load cell supported each ski. The track spanned the two other load cells, one positioned between the first and second set of wheels and the other positioned under the rear pivot arm joint to the rail. With fuel tank half full, the weight distribution was recorded with and without the driver, who was dressed in full riding gear.

Owing to the significant hysteresis in the suspension mechanism, the laboratory measurements of suspension deflections showed considerable variability. The field measured data were thus analyzed to determine the mean suspension deflection, which was considered to be representative of the static deflection. The mean values also revealed considerable variations, which were mostly attributed to the hysteresis effects. Moreover, the suspension hysteresis was believed to be significantly influenced by

temperature changes due to differences in thermal expansion coefficients of various components and to grease thickening effects. The suspension deflection just prior to and immediately after each run were thus extracted and averaged to derive the static deflections response. The resulting mean values for various runs revealed two clear outliers, which were believed to be caused by local bumps or dips in the snow, and excluded from the analyses.

In the simulator, the corresponding measurements were obtained by supporting the vehicle on four motion generators, representing the four load cells. The motion generators imposed a vertical rounded step displacement of small amplitude and the simulations were conducted until the vehicle approached its equilibrium. The resulting weights on the motion generators (acting as virtual load cells) and the displacements were then derived and compared with the experimental measurements to examine the model validity in terms of static response characteristics.

Table 4.1 presents comparisons of the measured suspension deflections with those attained from the model, together with the differences. The differences are also expressed as percentages of the maximum travel. The results show very good agreements between the model and measured results in terms of static suspension displacements. The largest relative error of -4% is observed for the center spring. It should be noted that the front and center spring stiffness values, and the gas charge pressure were adequately tuned to achieve such good agreements. The tuning however was performed within the manufacturing tolerances. The front coils stiffness was set to its lower tolerance limit of -10 %, resulting in 14185 N/m (81 lbf/in) and their gas pressure was reduced from the default 2.068 Mpa (300psi) value to 1.379 Mpa (200psi). The stiffness constant of the

Table 4.1: Comparison of the measured static suspension deflections with the model results.

Suspension deflection (mm)	Model	Measured	Error	Full travel	% Error vs full travel
Front right (D_{lr})	38.6	35	3.6	176.9	2.0
Front left (D_{ll})	38.1	35	3.1	176.9	1.8
Center (D_{cs})	24.7	28.3	-3.6	90	-4
Rear pivot arm (D_p)	1.1	0.98	0.12	48.8	0.25

center coil, made of two coils in series, was set to its upper tolerance limit of +10%, resulting in 21574 N/m (123.2 lbf/in) while the damper gas charge was kept to its nominal value of 2.068 Mpa (300 psi). The resulting stiffness of each coil-over-shock unit is non-linear due to the gas charge stiffness being an exponential function of damper piston displacement. It should also be noted that although the relative errors are quite low, the front springs undergo slightly excessive compression while the center spring lacks some. Table 4.2 illustrates a comparison of the measured weight distribution with the model data, along with the corresponding error. The results again show reasonably good agreement between the measured data and the model results. The relatively larger error of 5.9% in the rear pivot arm was attributed to excessive preload and/or stiffness of the rear torsion springs, even though the nominal values were used.

Table 4.2: Comparison of measured weight distribution with the model results.

Supported weight (N)	Simulator	Prototype	Error	% Error vs prototype
Front right	592.5	572.1	20.4	3.6
Front left	592.5	607.4	-14.9	-2.5
Center front wheels	1360.9	1390	-29.1	-2.1
Rear pivot arm	887	837.8	49.2	5.9
Total:	3432.9	3407.3	25.6	0.75

Since the rear of the vehicle and the skis support relatively larger proportion of the vehicle weight, the center spring becomes slightly unloaded. It is believed that a small reduction in the rear torsion spring load could yield weight distribution close to the measured values. Slightly lowering the skis, by 2~3mm, with respect to the track would also yield the same effect, that is, reducing the load on the skis and rear pivot arm while increasing that on the center spring. The relative errors are also close to the precision of the laboratory measurement system, primarily because the front load cells were equipped with "one-fits-all" support blocks entering the ski's central channel without an adequate fit, which resulted in somewhat uncertain vertical position of the skis relative to track plane.

It should be noted that the simulator's overall weight was increased very slightly (+0.7%) in an attempt to mimic the snow accumulation on the prototype vehicle, which had a beneficial effect on the weight distribution. Finally, the asymmetry in the simulator's front springs loads is attributed to a small difference in the shock tower positioning discovered late in the modelling process. This is considered to be tolerable since the model's roll DOF is locked.

The results presented in the above tables suggest that the static configuration of the model is acceptably close to that of the prototype vehicle. It should also be noted that no attempt was made to accurately identify the driver position, since it tends to vary continuously about its static configuration.

4.3 Dynamic Response Characteristics

The validity of the model in view of its dynamic behaviour is evaluated using four different response characteristics: (i) the frame responses; (ii) the suspension deflections;

(iii) the fundamental bounce and pitch frequencies; and (iv) the forced excitation transmissibility. The first measure is examined both in time and frequency domain, while the second measure (suspension deflections) is examined solely in the time domain. The last two measures were explored solely in the frequency domain. The comparisons of these measures are described in the following sections.

4.3.1 Frame Responses

As described in section 2.4.1, the prototype vehicle frame responses were measured using five sensors, thus recording the CM longitudinal and vertical accelerations, pitch velocity, seat surface vertical acceleration and the drive axle angular velocity relative to the frame. The pitch deflection of the frame was evaluated through time integration of the frame pitch velocity signal. The longitudinal and vertical velocities of the frame along its fixed axis system were evaluated from the measured local accelerations and the angular velocities. The coordinates of the frame CM in the global axis system were also evaluated in a similar manner. A total of ten response signals were thus considered to characterize the frame responses.

While the measurements involved three passes for each of the four trail segments, the comparisons and discussions are initially limited to the data obtained from a typical run. The similarities and differences observed for the other datasets, however, are discussed. The data acquired on the third pass of the Chibougamau trail segment 2 (labeled C2P3) is taken as the typical run, since it presents the system's response to an "average roughness" trail like those most frequently encountered. The braking part of each run was excluded, since the first intended model use focuses on relatively constant

speed coasting. The application of brakes prior to entering a curve, a situation encountered at the end of most studied segments, did not permit for acquisition of constant speed behaviour.

The four vital responses characterizing the frame and seat surface motion are examined first, since these provide the essential responses of the system, namely the longitudinal and vertical accelerations at the CM, the driver seat vertical acceleration and the frame pitch velocity.

Figure 4.1 illustrates the comparisons of time histories of measured vertical and longitudinal acceleration at the frame CM, seat surface vertical acceleration and frame pitch velocity responses with the corresponding model results. The model validity in general is assessed by a qualitative comparison of the time responses and the shape of the central tendency. Moreover, peaks observed in the simulation results (which may in part be caused by numerical noise) are used to rate the "quality" of the simulator's outputs, which further yields a perspective on the amplitude of oscillations about the central tendency.

The results presented in Figure 4.1 show that the central tendencies for the frame and seat vertical accelerations (A_{zl} and A_{zb}) and pitch velocity (ϕ_{pc}) signals match the experimental ones. The results obtained for the other segments revealed similar agreement. The simulated longitudinal acceleration response (A_{xl}) over segment 2, however, reveals considerably too high central tendency, although it was observed to better match the measures over segment 1 and even more so over segments 3 and 4.

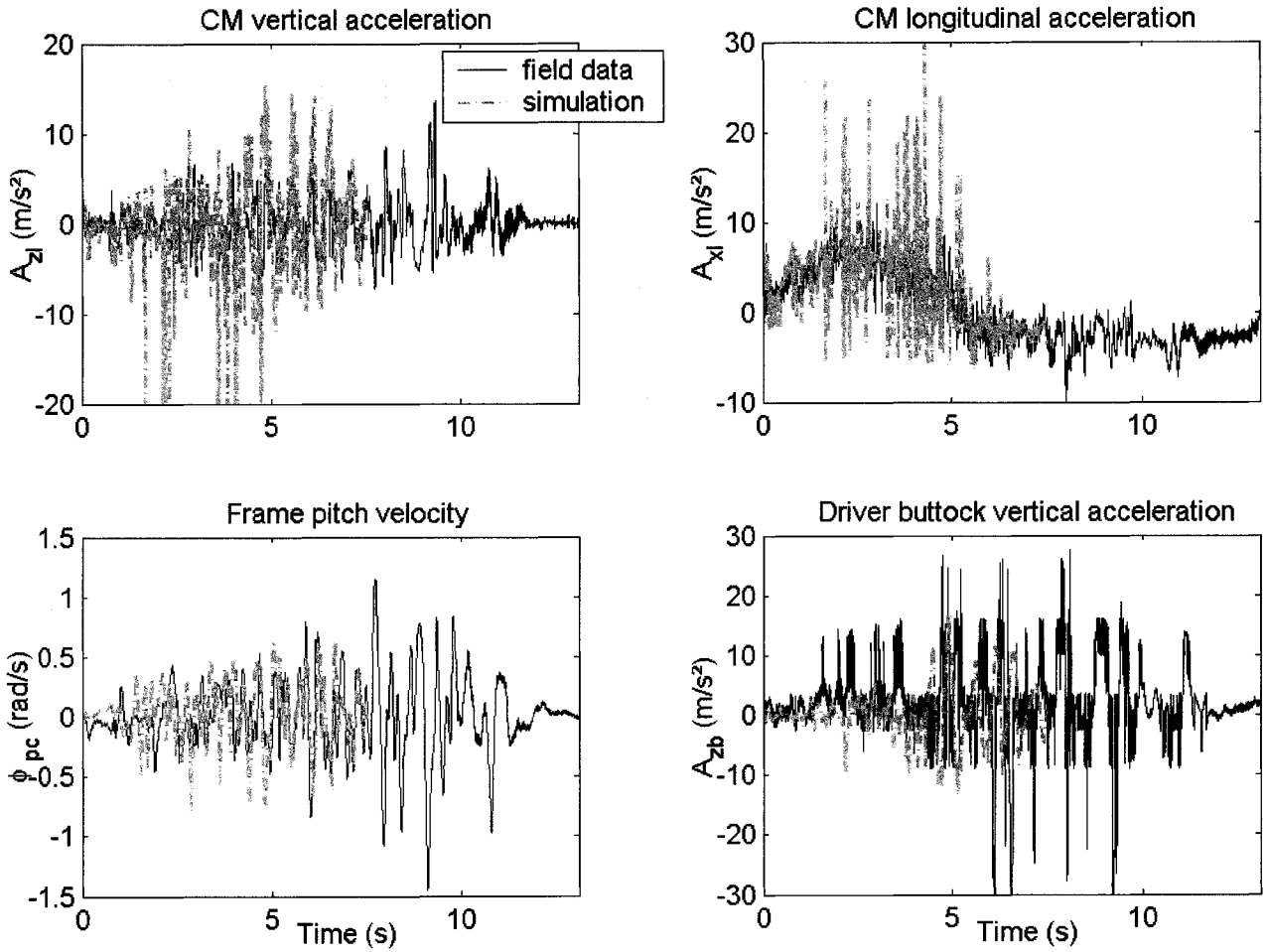

Figure 4.1: Comparison of measured frame and seat acceleration and frame pitch velocity responses with the model results (Trail segment: 2).

The agreements in the amplitudes of oscillations about the central tendency also differ from one signal to another and from one trail segment to another. The seat acceleration (A_{zb}) and pitch velocity (ϕ_{pc}) responses show reasonable agreements in the amplitude with those measured over segment 2. Similar agreements were also observed for segment 3, while peak responses were consistently lower than the measured data over segments 1 and 4. Over segment 2 (Figure 4.1), the model's vertical acceleration (A_{zl}) tends to be higher than that measured on the prototype. Results for segment 3, however, reveal better agreement, while the model response is considerably low over segment 4. The longitudinal acceleration (A_{xl}) of the model also shows trends similar to the measured data. The lower responses over segment 4 were attributed to the deficiencies in the track profile reconstruction, which was obtained using the frame acceleration signals instead of the skis accelerations, as already mentioned at the end of section 2.4.2. The A_{xl} response under excitations from segment 4 again resulted in significantly lower amplitudes of motions when compared to the measured data.

With the exception of ϕ_{pc}, the vertical (A_{zl} and A_{zb}) and longitudinal (A_{xl}) acceleration responses show sharp peaks of relatively high magnitudes, as evident in Figure 4.1. The magnitudes of such peaks were observed to be considerably smaller over segments 1 and 3, and nearly absent for segment 4. The results shown in Figure 4.1 thus represent the worst case of signal noise, which is mostly attributed to numerical phenomena, such as integrator restarts triggered by reaching an Euler angle singularity in one of the rigid bodies. Another major cause of the noise is the rail to ground contact, which yields abrupt variations in the instantaneous normal force, following harsh variations in the rail to terrain penetration and penetration velocity. Secondly, the force

centroid tends to oscillate along the rail, as the pressure distribution between the rail and ground vary under interactions with the bumps. Apart from these, the contact elements, such as the two rear pivot arm stops, also induce some noise in situations when the rear stop is put to work while the vehicle is airborne. In this case, the ground contact and track friction are not available to damp the rail's motion. It should be noted that A_{xl} and A_{zl} are highly coupled, in part by their intimate dependence on rail-to-ground contact, directly influencing A_{xl} through the traction model, and also by the weight transfer and front arm reaction force (see Figure 2.2).

The frequency contents of the vast majority of the noise observed in the responses are well above the terrain profile frequency contents. This was verified by first performing the simulations under excitation arising from the original ground profiles, and then by repeating the process using low-pass filtered ground profiles. The results attained from both excitations revealed similar degrees of response peaks. However, the simulation results clearly showed that such response peaks (noise) arise under excitations from the rough or "bumpy" parts of the trail segments. Segment 1 is the roughest segment of all and its noise levels are very similar to those attained over segment 2, which is the next rougher. The smooth segment 4 on the other hand displayed the least noise. This is consistent with the noise generating mechanisms described above, as they are triggered either by variations in the contact geometry between the rail and the ground or by large motions of the rigid bodies, particularly those of the rear suspension mechanism. Signals ϕ_{pc} and A_{zb} present none and relatively lower magnitudes of noise, respectively. It is filtered out by the integration process in the first case and by the non-linear spring-damper representing the seat in the second case.

The relatively lower amplitudes of oscillations in A_{xl} on all but segment 3 is partly attributed to the absence of the undamped stiffness of the drive axle and the track belt. Strain gages were installed between the driven end of the drive axle and the first of four toothed pulleys driving the track. The drive axle torsion and track belt stretching were thus not measured and are not incorporated in the model, thus eliminating a source of low to medium amplitude, and high frequency oscillations.

The central tendency of signal A_{zl} from segments 2 and 3 replicated very well the experimental data. However, that of signal A_{zb} is accurate over segment 3 but falls under target on all the other segments. This is partly attributed to the fact that A_{zb} is not measured in the same way in the simulator as it was in the experimental setup. An instrumented rubber pad was secured to the seat surface for field recordings, while the simulator model provides the acceleration of the driver's buttock along the Z axis of the frame. The seat pad effectively becomes a very light mass on the seat surface when the driver loses contact with the seat, while traversing a bumpy or rough part of the terrain. Provided that the seat is still partly compressed when the driver loses contact, as upon hitting a sudden bump, the seat pad sees a high positive acceleration due to the seat rapid expansion and a high negative acceleration if the seat reaches full expansion before the driver lands back on it. No similar reduction of effective seat surface mass arises during compression. Even the landing of the driver on the seat does not produce comparable acceleration amplitude, partly because the driver slows his descent with his legs.

Once the traction model had been developed using a combination of measurements from the four trail segments, the track-to-rail and ski-to-ground friction characteristics were tuned to match the longitudinal behaviour over the longest and

smoothest segment, where their effects are expected to be the highest. Consequently, the central tendency in A_{xl} over segment 4 was observed to be close to the expected behaviour. This also provided reasonably good agreements over segment 3, while the simulations over segment 2 and especially segment 1 resulted in considerably higher longitudinal accelerations. The origin of this is thought to be simply the large changes in the friction and available traction of the snow cover from morning to noon to late afternoon. Indeed, over the three days of field experiments, the snow cover went from moderately soft snow on a hard packed crust to freshly fallen fluffy snow, and later to wet sticky and grainy snow. After the initial friction tuning over segment 4, a second iteration was performed to achieve better agreement on the other segments. Further improvements could be achieved through refinements of the structure of the traction and snow friction models.

All segments display rather good agreement in central tendency of the ϕ_{pc} response except for segment 1, which resulted in higher mean values since the terrain profile did not produce pronounced negative excursions as observed for other segments. Most of this can be attributed to relatively higher front suspension deflection when climbing over moguls, thereby inducing lower negative pitch velocity. Again, this is a consequence of the excessive longitudinal velocity over segment 1.

The fidelity of the four frame response signals is also evaluated in the frequency domain by analyzing the power spectral density (PSD) of the signal, which are also compared with those of the measured data. For this purpose, only the "coasting" part of the signals is used, removing the initial acceleration and strong transients, so as to satisfy to the extent possible the stationary condition requirement of the frequency domain

computations. Furthermore, sub-segments from the field and the model results have been matched so that they correspond to the exact same part of the trail profile, ensuring that the ground excitation be the same in each case. The longitudinal velocity response of model typically differed slightly from the experimental one so that corresponding signal sub-segments do not have the same duration and number of points, hence requiring a matching procedure. The agreement of the spectra of the measured data and model results were assessed using two qualitative characteristics: (i) the shift in the frequency, if any, of the dominant peaks; and (ii) the amplitude ratio of those peaks, evaluated by comparing the model results with the experimental data.

Figure 4.2 presents the sample results comparing the PSD's of the model results with those of the measured data, again from run C2P3. The figures show the results attained from two simulations under original (sim_orig) and low-pass filtered profiles (sim_LP). Filtering was carried out using a numeric Butterworth kernel with 25 Hz pass band upper frequency, 40 Hz stop band lower frequency, 1 dB pass band ripple and 45 dB minimal stop band attenuation. In order to apply this time based filter to the space based trail profiles, these were converted to time base by dividing them by the average longitudinal velocity over the part of the corresponding experimental runs that were retained for frequency domain analysis.

The model results show trends similar to those observed in the measured data, although considerable differences exist. The longitudinal acceleration response (A_{xl}) displays the poorest agreement with the measured data. This may in part be attributed to the fact that its energy is spread out over a large frequency band, from almost DC to 40 Hz, beyond which the signal was strongly attenuated by the data logger's filter.

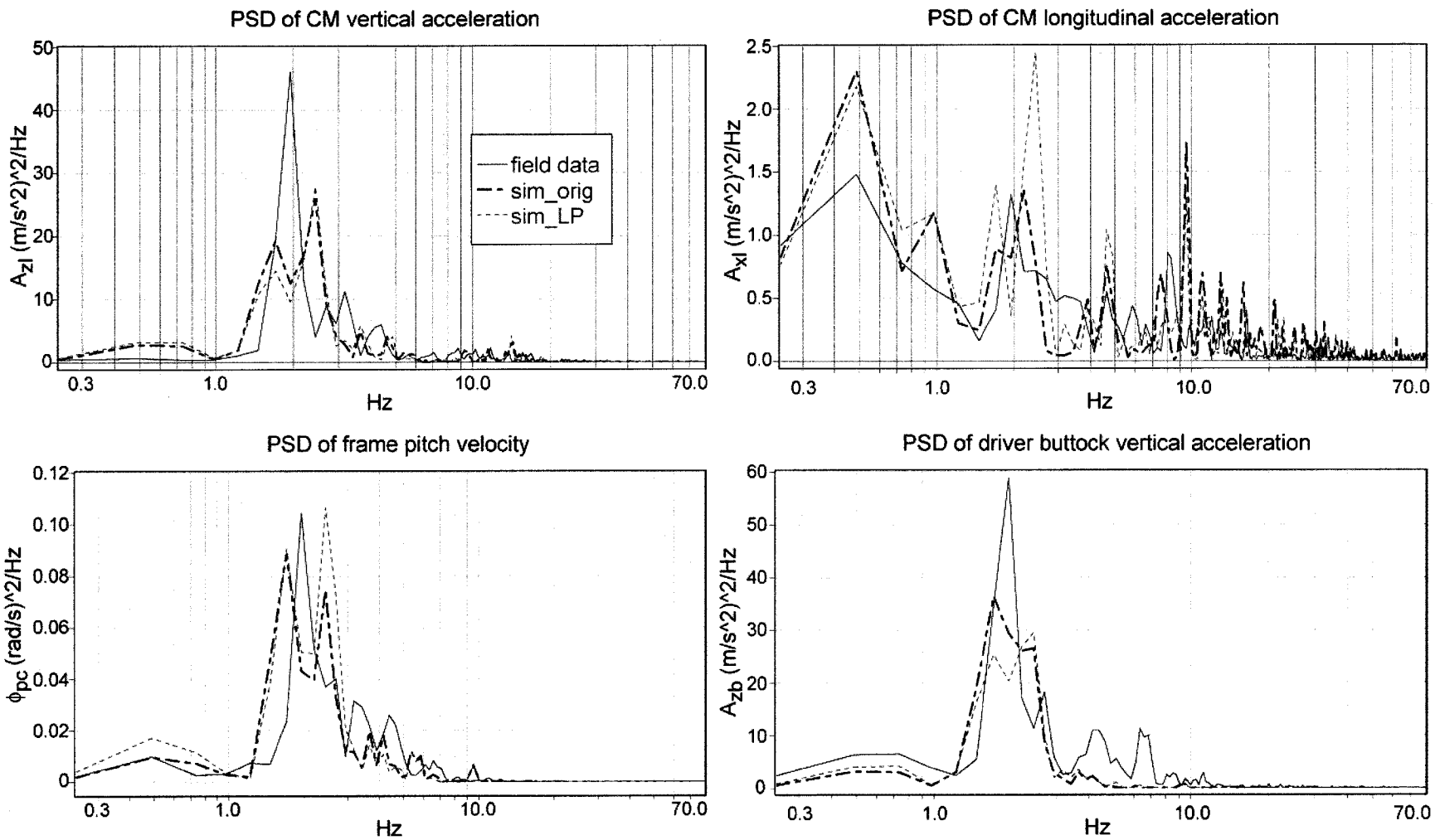

Figure 4.2: Comparison of PSD's of the measured data and the model results in terms of frame and seat responses (Trail segment: 2).

The results, however, show good agreements in terms of frequencies corresponding to the peak values, which occur near 0.5, 2, 4.5 and 8-9 Hz.

Except for A_{xl}, the dominant peaks in the measured vertical accelerations and pitch velocity occur in the frequency range of 0.89 to 1.24 Hz. This range was consistently observed from the data acquired from all the runs. This range is considered to be small and is attributable to the system's non-linearities and couplings, making the apparent vertical stiffness a function of the suspension deflection and the longitudinal velocity. However, it was interesting to note that the excessive longitudinal velocity under segments 1 and 2 did not induce a proportional increase in the corresponding frequencies of the dominant peaks. This suggests that the dominant peaks occur near the system's natural modes, although the frequency contents of the response are sensitive to specific excitation (e.g. choice of trail profile sub-segment).

While the frequencies of the dominant peaks in the measured data may be considered to be in the vicinity of those in the model results, the magnitudes of dominant peaks' differ considerably. The results shown for segment 2 (Figure 4.2) generally reveal that the peak PSD magnitudes of measured vertical acceleration responses are higher than those of the model responses, irrespective of the excitation used (sim_orig and sim_LP). The model validity in view of the spectra was evaluated by computing the ratio of the amplitude of dominant peaks from the simulation results to the magnitudes of corresponding peaks in the measured data. In cases where the two peaks were quite close, the average of the ratios of the two peaks was used. The reasoning behind this being that the energy within the considered limited frequency band is more representative of the system's response than the energy at any specific center frequency. The computed

amplitude ratio revealed a lower bound of 0.07, unsurprisingly attained over segment 4 for A_{zl}, while the upper bound attained for segment 2 approached a value of 2.5 in signal A_{xl}. The next highest ratio of 1.7 was obtained in A_{zl} for the run C2P3 (Figure 4.2). For the results attained for segment 2 alone, the amplitude ratios range from 0.92 to 1.7 (up to 2.5 for A_{xl}). The extreme differences in the dominant peaks can partly be attributed to the differences in the simulated and measured longitudinal velocities. The model velocity was nearly 1.3 times the measured velocity, which can be attributed to the traction model representing only one "average" snow condition, thereby being unable to reproduce the variations in traction observed on the different trail segments.

The quality of the model is finally examined by comparing different statistics of the responses and the measured signals. These include the overall rms values, peak values corresponding to 99% probability, and crest factors (ratio of peak to rms values). Table 4.3 presents comparisons of the model responses to the measured data under segment 2 excitation. It contains the model results attained under both the original and low-pass filtered terrain profiles. The results show that all the acceleration measures attained under the original profile are higher than those attained under the filtered profile. The opposite trend, however, can be observed in the pitch velocity response measures.

The model validity is further assessed in terms of the ratios of the model response to the measured values for the three metrics. The mean values of the two simulation results are considered for evaluating the ratios. For trail segment 2, Table 4.3 suggests that, for rms acceleration, this ratio ranges from a low value of 0.65 for the seat acceleration to a high of 1.04 for the longitudinal acceleration. Considering all segments,

the data analysis revealed that the overall lower bound of 0.37 comes from the rms vertical acceleration over segment 4. Excluding segment 4, the lower bound would be

Table 4.3: Basic statistics of the frame and seat signals for trail segment 2.

Run:	C2P3	Series:	Field	Sim_orig	Sim_LP
A_{zl}	RMS	(m/s^2)	6.57	5.92	5.55
	Peak@99%	(m/s^2)	18	14.4	13.32
	Crest factor	-	2.74	2.43	2.4
A_{xl}	RMS	(m/s^2)	2.74	2.98	2.71
	Peak@99%	(m/s^2)	8.2	10.15	9.34
	Crest factor	-	3.0	3.41	3.44
Φ_{pc}	RMS	(rad/s)	0.4	0.32	0.33
	Peak@99%	(rad/s)	1.21	0.77	0.83
	Crest factor	-	3.05	2.39	2.51
A_{zb}	RMS	(m/s^2)	8.45	5.48	5.54
	Peak@99%	(m/s^2)	29.6	14.6	14
	Crest factor	-	3.5	2.66	2.53

0.59 for ϕ_{pc} over segment 1, for an overall range in rms values of 0.59 to 1.04. This is consistent with the evaluations performed in the time domain and is considered acceptable in a first trail modeling effort given that the rebuilt trail profiles can at best be as rough as the experimental ones, more likely being somewhat smoother. The current traction model limitations also tend to slightly reduce the fluctuations in the longitudinal acceleration.

Peak values cover a more symmetric, although not narrower, range around the target values with a lower bound of 0.42 (in A_{zb}, segment 4) and an upper bound of 1.37 (in A_{xl}, segment 2). These ratios are not expected to be greatly affected by the occasional numerical spikes, since the peaks are derived over 99% probability, and labeled as

"Peak@99%". These peak values, however, are more sensitive to isolated features than the rms or mean values. The observed ranges are thus considered acceptable, given the noise induced by the contact elements, namely the rail to ground contact.

The crest factors of the responses directly follow from the previous results and their range goes from 0.67 (in ϕ_{pc}, segment 2) to 1.3 (in A_{xl}, segment 2). Being as narrow and more centered than the two previous metrics, they are considered to demonstrate a good match between the model and the experimental results.

Figure 4.3 further illustrates comparisons of the instantaneous velocity responses of the frame along the local X and Z axes (V_{xl} and V_{zl}), and the drive axle angular velocity relative to the frame (ϕ_{pb}) with the corresponding measured data attained for segment 2. The results show reasonably good agreements in the velocity responses except for some deviations in ϕ_{pb} during the initial acceleration phase. Analyses of the data for the remaining segments revealed good agreements in V_{xl} for all the runs.

The forward velocity generally increases in a very smooth fashion and gradually decreases after 5 s, following well the experimental trend. The model quality was assessed in terms of the initial slope ratio, defined as the approximate ratio of the model V_{xl} response slope to that of the experimental data. This slope ratio ranged from about 0.98 for segment 4 to 2 for segment 1, and was nearly 1.2 over segment 2, as seen in Figure 4.3. This large range is due to the deficiencies in the traction model, and the ski and track friction models, to account for the significantly different friction and shear resistance characteristics of different snow types. Furthermore, multiplying the traction model output (i.e. the propulsive force) by a simple coefficient lower than 1 is barely beneficial. It is not effective at slowing the vehicle down because the initial reduction in

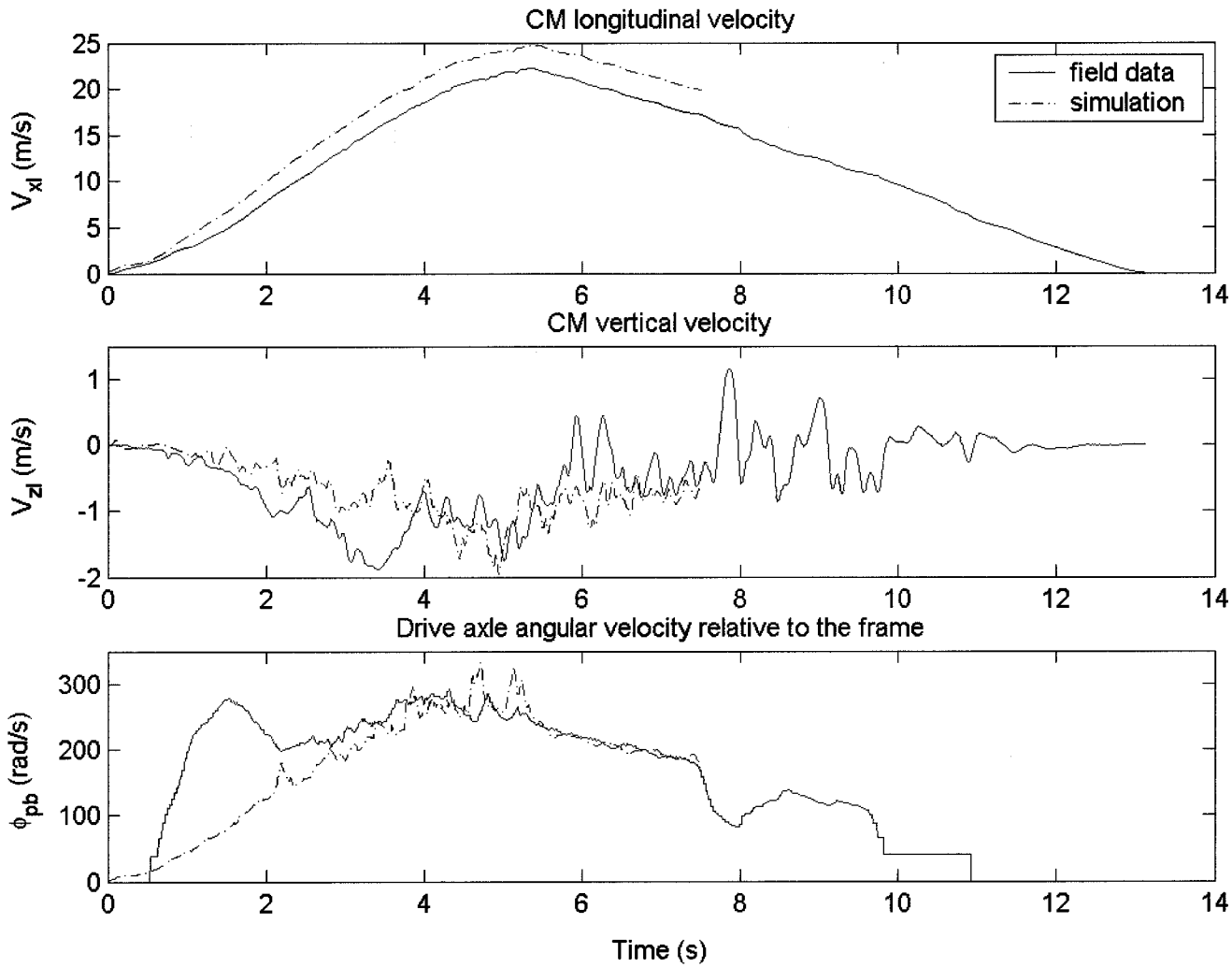

Figure 4.3: Comparison of measured and simulated CM and drive axle velocity signals (Trail segment: 2).

propulsive force unloads the drive axle to which the applied driving torque has not been reduced. Consequently, the drive axle accelerates and the slip ratio goes up, thus increasing the propulsive force. Results of simulations using such a downscaled traction force (not reproduced here) displayed very little reduction in longitudinal acceleration and velocity while the good match of the drive axle angular velocity was lost. Improving upon the current results will require refining the very form of the current traction model.

Unlike the longitudinal velocity response, the vertical and pitch velocity responses exhibit oscillations. The model responses in both, V_{zl} and ϕ_{pb}, show good central tendency for segment 2, which was also evident for most of the trail segments. The peak magnitudes in V_{zl} and ϕ_{pb} are also comparable, while the magnitudes of V_{zl} response over segment 4 were significantly lower, as discussed earlier. The comparisons in ϕ_{pb} suggest that the current traction model cannot reproduce the gross slippage occurring during the hard initial acceleration. The results attained for the other segments displayed similar discrepancies in the measured and model results. The model simulator, however, yields relatively higher longitudinal acceleration and velocity on most segments, as evident in Figure 4.3 for segment 2.

Despite the lower slip ratio, the traction model yields higher propulsive force than the prototype vehicle. This implies that past a certain unknown high slip ratio value, the real traction force drops abruptly in a non-linear way. Further experimental work at high slip ratio would be needed to characterize this behaviour. Such a phenomenon is most likely caused by the snow intrinsically behaving as a shear thinning fluid, where the rate of increase of its shear stress decreases with increase in the shear strain. Apart from the

gross slip, the simulator generally produces very good central tendency in ϕ_{pb} except for segment 1, where the amplitude ratio approached 1.5 at its worst.

Figure 4.4 further illustrates comparisons of the model and measured velocity responses over segment 3, which involves a different type of manoeuvre. The results again show reasonably good agreements in velocity responses of the model and the prototype vehicle, although considerable deviations in the velocity magnitudes could be observed.

The coordinates of the vehicle CM and the frame pitch angle relative to the inertial coordinate system, as derived from the model are finally compared with the measured data in Figure 4.5. As a direct consequence of the generally higher longitudinal acceleration and velocity responses of the model, its longitudinal position (X_g) response is greater than that shown in the experimental data. The amplitude ratio is the same as that seen for V_{xl}. Clearly, the longitudinal position progresses monotonically, while the magnitudes of oscillations are significantly smaller than the central tendency.

The amplitude ratios in the vertical coordinate (Z_g) of the model for the different runs are also very close to those obtained for V_{xl}. The results suggest that the model simply traverses the trail profile faster than the prototype vehicle. This holds true for all but segment 4, which yields significantly larger error in the CM path. For this segment, the vertical position central tendency ratio was obtained near 0.18.

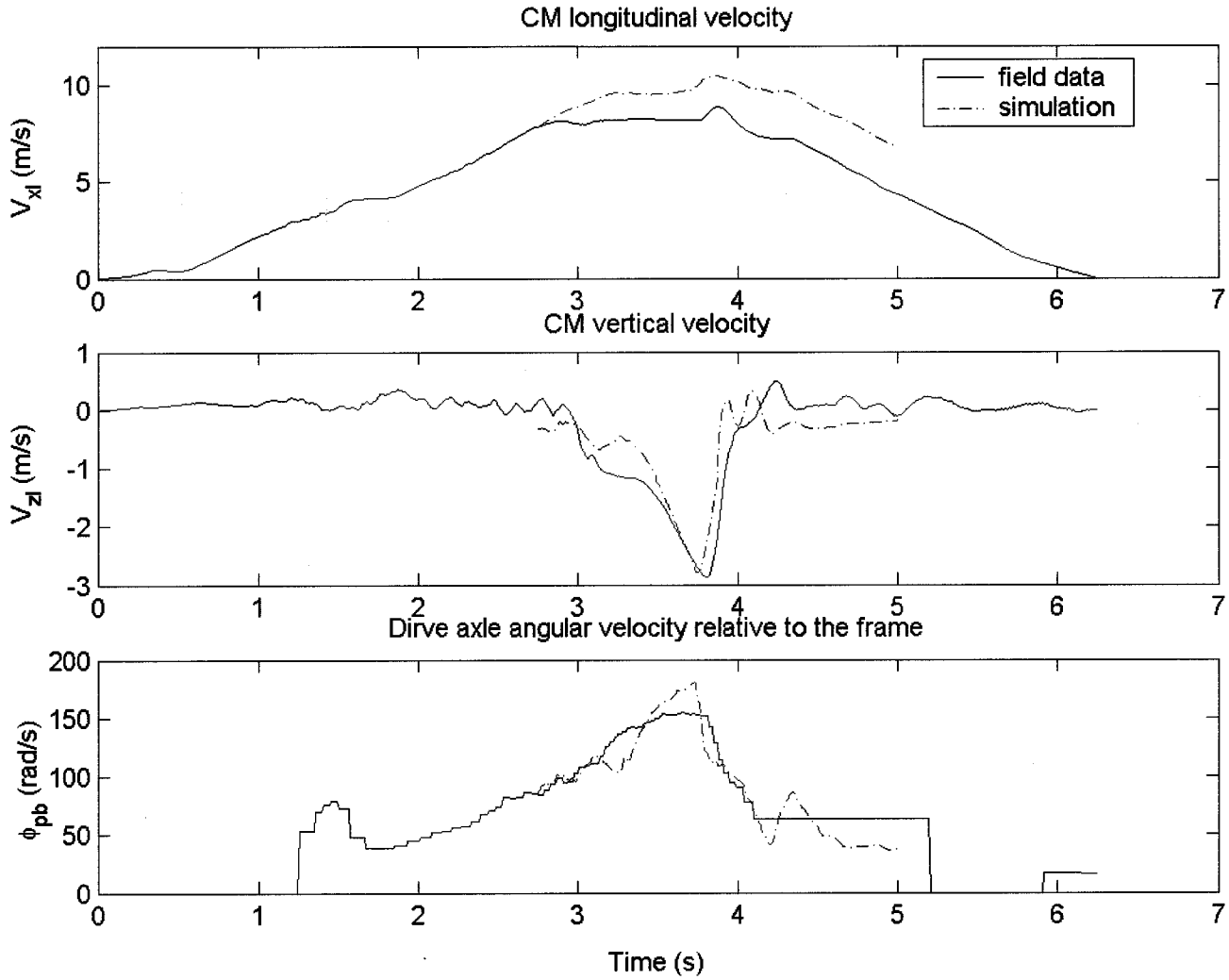

Figure 4.4: Comparison of measured and simulated CM and drive axle velocity signals of run C3P2.

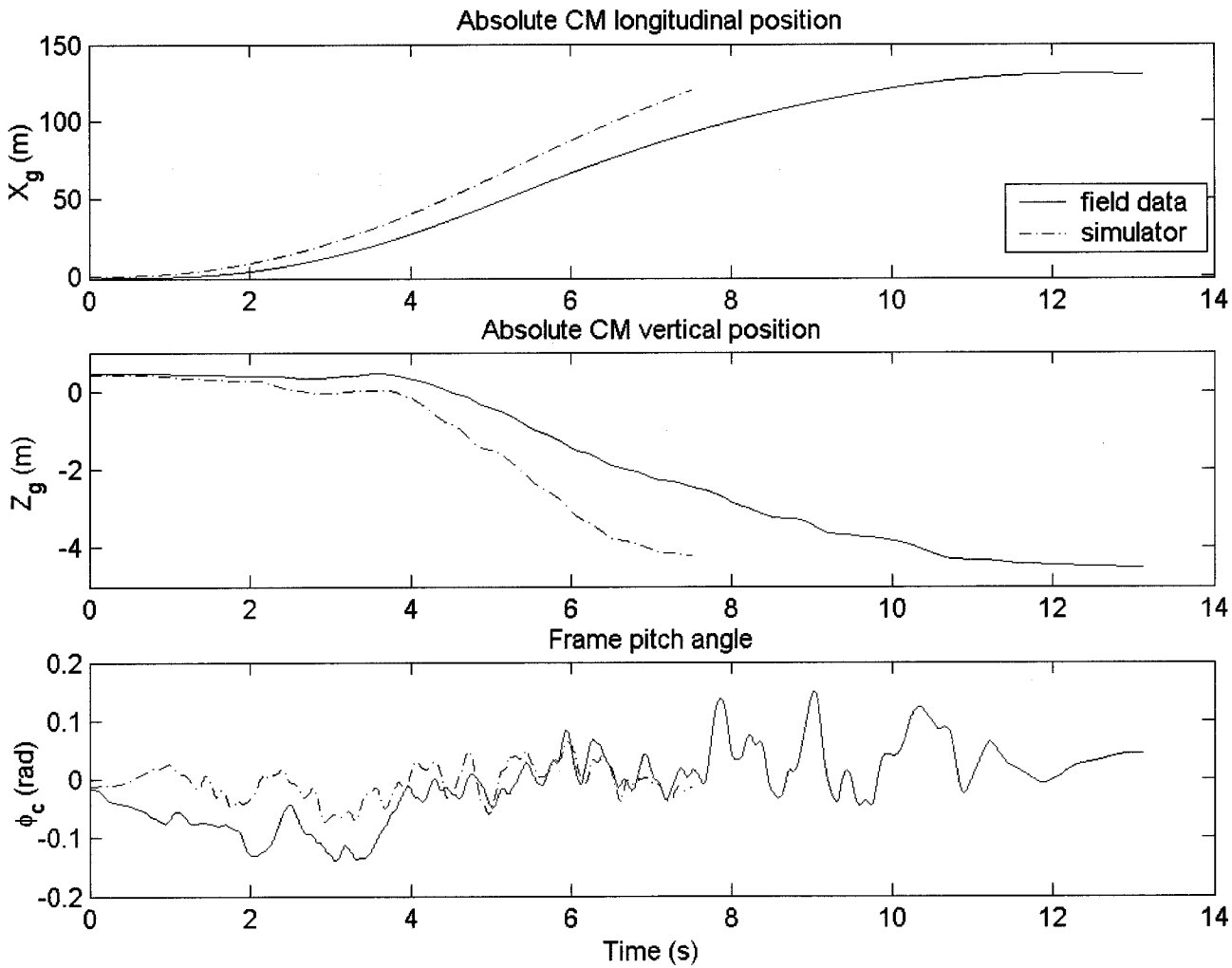

Figure 4.5: Comparison of measured and simulated absolute CM position and pitch angle (Trail segment: 2)

Contrary to the X_g response, the Z_g coordinate response exhibits oscillations about its central tendency. The oscillation amplitude ratio (model vs experiments) ranges from 0.5 over segment 1 to 1.5 over segment 2. Paradoxically, both extremes are attributed to different effects of the same cause, the excessive longitudinal velocity. In the first case, the extreme profile roughness and high speeds force the model suspended mass to "glide" over the deepest parts of the dips, thereby reducing vertical oscillation amplitude considerably. In the second case, somewhat smoother profile allowed the simulator's suspended mass to accurately follow the profile though at a higher pace than that of the prototype.

The pitch angle (ϕ_c) response of the model reveals similar degree of agreement with the measured data. Both the mean and the average slope are very close to those of the measured data for the segment considered. Similar trends were also observed for the other segments. The models results attained for segment 1 revealed a higher mean pitch angle due to gliding of the model vehicle over the bottom of the dips. The prototype vehicle, on the other hand, revealed better adaptation, where a strong negative (nose up) pitch angle permitted the vehicle to climb out of the dips. Over segment 4, the slope of the pitch response was significantly too low due to the rebuilt profile erroneous inclination. Neglecting the responses over segment 4, the ratio of oscillation amplitudes ranged from 0.6 on segment 1 to almost 1 on segment 2, as shown in Figure 4.5.

Figure 4.6 presents an overplot of the path traveled by the CM for the prototype and the model together with the hand-measured and the rebuilt ground profiles. Clearly, the model follws the rebuilt ground profile very closely, which is supplied as input in ADAMS. This emphasizes the fact that a significant part of the difference between the

prototype and the model simulator responses arise from the limited accuracy of the trail profile and the prototype motion rebuilding algorithms, as shown by the difference between the hand measured and rebuilt ground profiles. All the runs displayed similar levels of fidelity between the rebuilt profile and simulated CM motion.

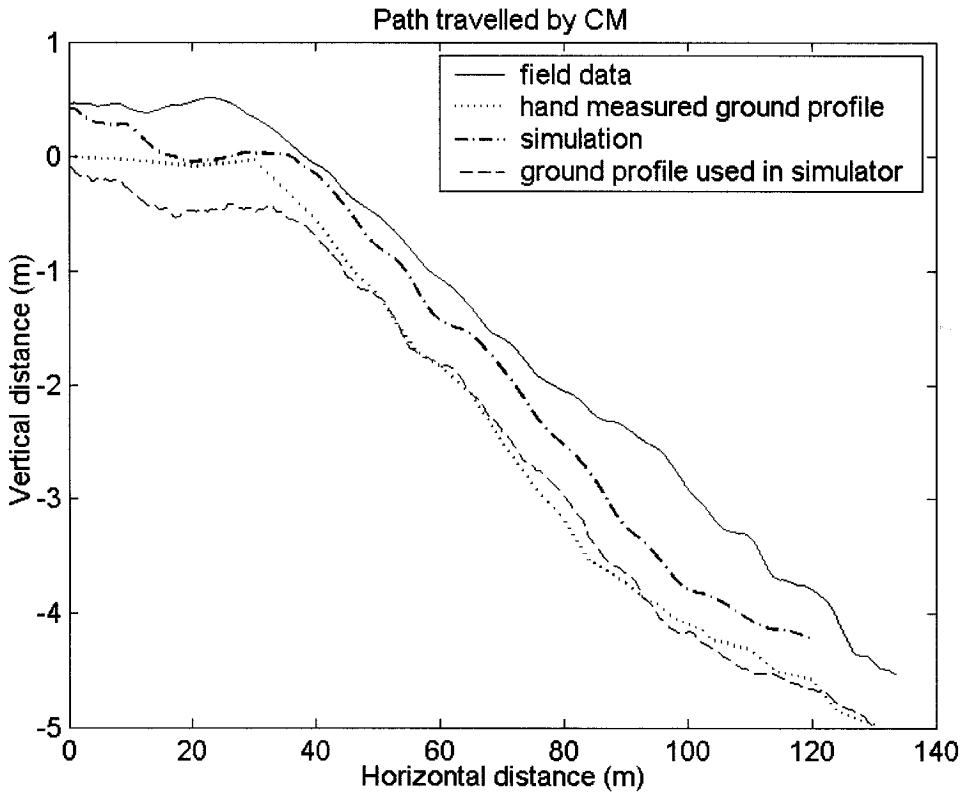

Figure 4.6: Comparisons of measured and simulated path travelled by CM (Trail segment: 2).

4.3.2 Suspension Deflections

Following the model evaluation in terms of frame signals, the model validity is examined in terms of deflection responses of the central, front-left and front-right springs, and the rear pivot arm potentiometer position. The signals are initially analyzed to derive their elementary statistical properties, before the corresponding velocities are computed.

Figure 4.7 illustrates comparisons of the model results and measured data in suspension deflections for run C2P3 (segment 2), as an example.

For springs, the correspondences are evaluated based on three criteria: the central tendency's apparent mean, its slope and the oscillation amplitudes about the central tendency. Since the rear pivot arm usually rests against its rear stop under acceleration and moderate "road load" cruising, its contact ratio and amplitude of motion were used to evaluate the quality of the potentiometer signal. The results are thus evaluated using nine different measures involving 3 springs and 3 criterion for each spring. It is important to note that the model results attained for segments 1 and 4 showed considerable deviations from the measured data, as it was expected for reasons discussed in the previous section. The oscillation amplitude ratio displayed the best match of all metrics, if segment 4 results are not considered. The amplitude ratios ranged from about 0.5 (center spring, segment 1) to 1.2 (front left, segment 3 and front right, segment 1). The poor agreements for segment 1 are attributed to its excessive propulsive force generation that excessively stiffened the rear suspension through the track tension coupling. Considering segments 2 and 3 only, the range reduced to 0.75 to 1.2, which is considered to be quite good given the level of accuracy of the trail profile rebuilding algorithm and generally excessive longitudinal velocity.

In section 4.2, the static response characteristics of the model generally showed slightly higher front springs compression and slightly lower center spring compression when compared to those of the prototype springs. This tendency is more pronounced in the dynamic responses, again especially on segment 4, although considerably less on

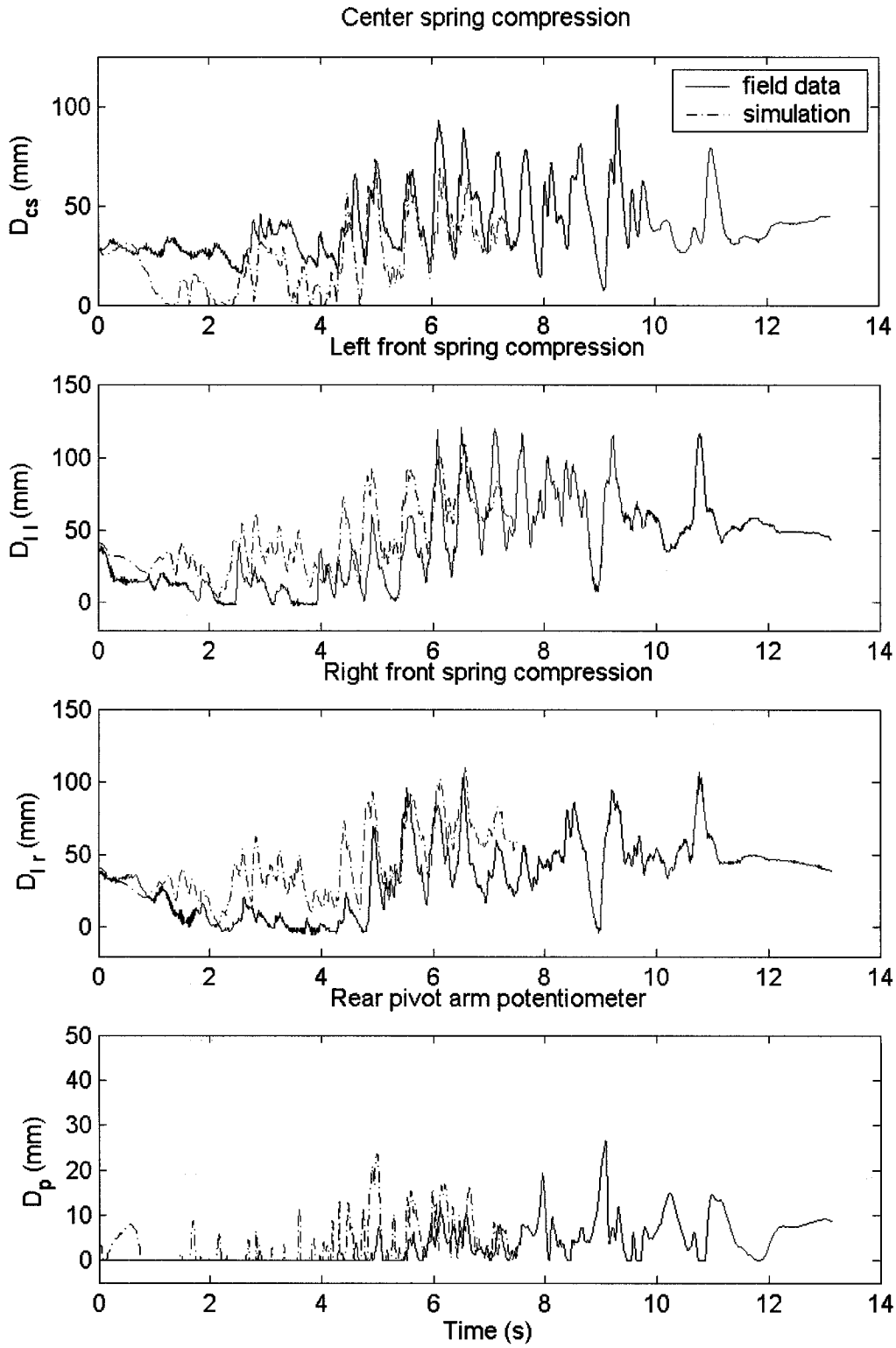

Figure 4.7: Comparisons of suspension deflection responses of the model with the measured data (Trail segment: 2).

segment 1. This would be acceptable for segment 1, given the deformed excitation to the model arising from its excessive longitudinal velocity. Over segments 2 and 3, the model results in terms of mean compression of all the springs showed very good agreements with the measured data. The slopes of the spring compression responses also revealed close agreements with those of the measured data, except for segment 1. Over this segment, the simulator's center spring tends to extend slightly more than the prototype vehicle spring, while the right front spring revealed the opposite behaviour. This is again caused by the higher velocity on this segment leading to the simulator tracking the ground profile differently than the prototype, as discussed previously.

The deflection response of the rear pivot (D_p), shown in Figure 4.7, suggest that the pivot stays against its rear stop during most of the acceleration phase and only starts moving in the moguls, when the acceleration is negligible. Typically, the simulator shows too low a contact ratio, with segment 2 presenting the largest excess of rear pivot arm motion. Moreover, the amplitude of motion is significantly high; its ratio ranges from 1.4 over segment 3 to 2 over segment 2, while it is quite comparable for segment 1 and significantly too low over segment 4. These strong discrepancies can be due to two factors. First, the generally higher motions are attributable to lack of consideration of the suspension dry friction ("stiction"), and accompanying hysteresis. The results attained from laboratory experiments (not shown here) revealed high level of dry friction in the mechanism (section 4.3.3). In this experiment, all the dampers were completely drained to eliminate the presence of viscous damping. The frame was then pulled down to a known suspension compression and suddenly released, while the free oscillations of the sprung mass were recorded. The measured data revealed rapid decay of the frame motion,

which did not even complete a single full cycle. These results suggested the presence of significant Coulomb friction within the suspension and the pivot.

The second factor concerns the relatively higher amplitudes of motions derived from the model. During the field measurements, a scalar coefficient was introduced, directly in the data logger's interface software, in order to scale down the potentiometer signal so as to approximate the rear pivot arm head displacement. It should be noted that the potentiometer was mounted above the upper pivot axis (head axis) of the rear pivot arm. This scaling factor was determined experimentally, following common field instrumentation practice, during the measurement setup. This scale factor is believed to be close to the ratio of the distance separating the potentiometer spherical joint from the rear pivot arm lower pivot axis to the effective rear pivot arm length (axis to axis). That ratio was measured as 1.29, whereas the ratio of the highest pivot displacement (D_p) responses of the model to the measured data was 1.58, when the rear pivot arm hit its front stop during the "flight" on segment 3 as seen in Figure 4.8, segment 3. The model thus yields an overestimate of the rear pivot arm motion, although to a lesser extent than evident in the figure, since the model position responses signals need to be divided by approximately 1.29. This step was not undertaken, since the exact value of the coefficient used in the data logger was unknown.

Figure 4.8 highlights one other important information about springs stiffness. Following the take off, the model's front coils rate of extension is significantly lower while that of the center spring is considerably higher. This could arise either from erroneous damping curves or coil stiffness, since all the masses are in good agreement with the measured values. It is essential to add that the damping curves of all the four

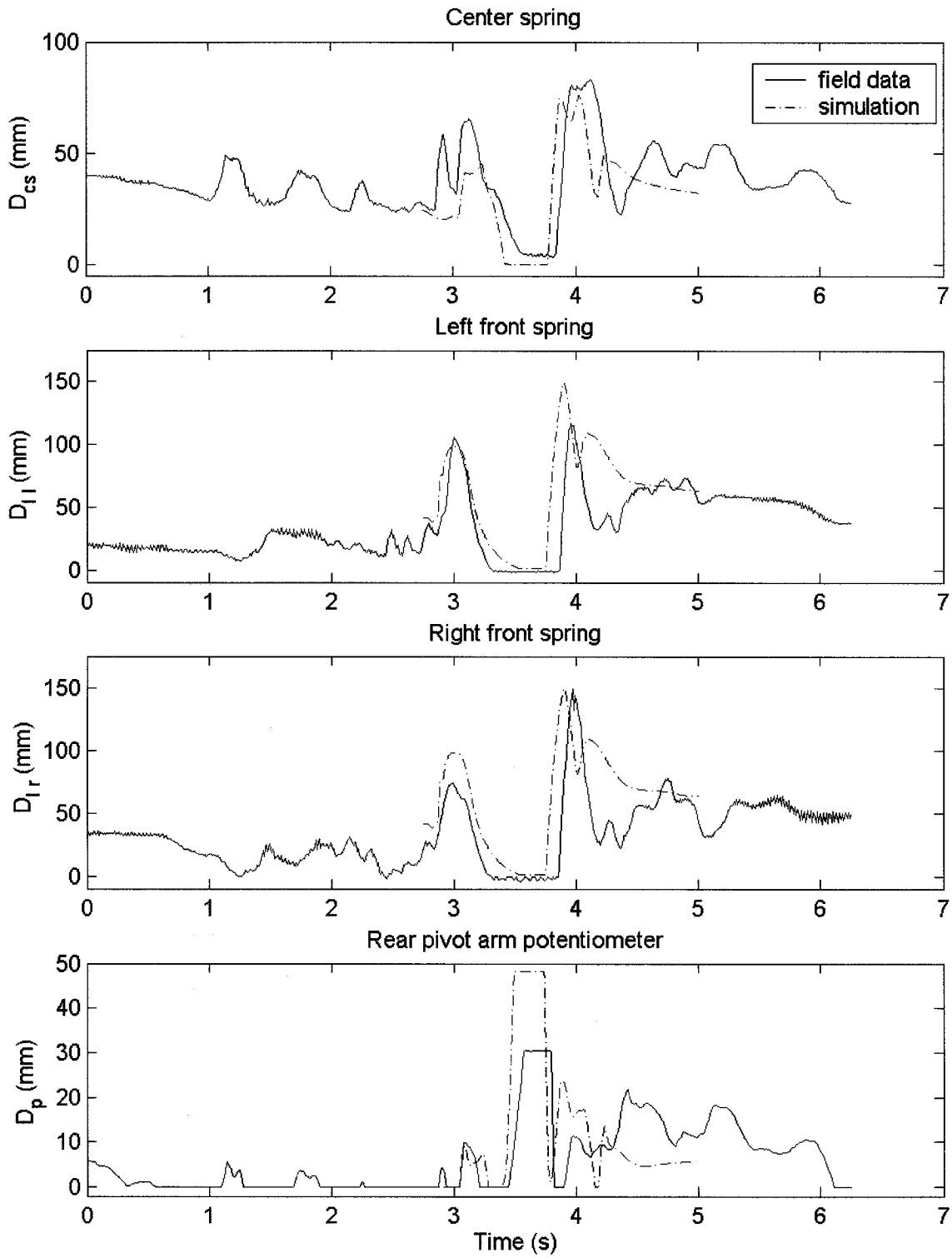

Figure 4.8: Comparisons of suspension deflections of the model with the measured data (Trail segment: 3, run: C3P2).

dampers were recorded on a dynamometer prior to their installation in the prototype vehicle. The majority of the error is thus believed to be caused by the erroneous stiffness values that were not verified through measurements. The model, instead, employed the nominal values and tolerance range, as described in section 4.2. Moreover, the damping is moderately temperature dependant. Hence, the damping properties of the front dampers, directly exposed to cool air flow and snow projection, may contribute to discrepancies in the results. The majority of error, however, is attributable to apparently too soft front springs and too stiff central springs. This trend was also observed from the static responses, where the front and central springs showed too high and too low static deflections, respectively.

The suspension deflection responses of the model are further evaluated in terms of mean deflection, standard deviation of the mean, and peak deflection about the mean value based upon 99% of the events (peak@99%@mean). The computed values for the suspension springs and arm pivot are compared with those of the measured data, where the data attained for segment 3 was excluded. The model responses are evaluated for both the original and filtered track profiles, as shown in Table 4.4 for the sample run on segment 2.

The results generally show that mean deflections of the model center spring are considerably too low, while that of the left front spring are significantly too high, as expected. The mean compression of the central coil ranged from 0.37 to 0.68 and that of the front coils varied from 1.18 to 1.63. The central coil deflection standard deviation is quite close to that of the measured data (range: 0.73 to 1.06), while its greatest excursions about the mean are smaller (range: 0.68 to 0.82). For the front springs, the peak

Table 4.4: Comparisons of mean, standard deviation and peak suspension deflection responses of the model with corresponding measured data (segment 2).

Run: C2P3	Series:		Field	Sim_orig	Sim_LP
Center spring	Mean	(mm)	40.5	27.33	27.69
	Standard deviation	(mm)	17.3	17.61	16.82
	Peak@99%@Mean	(mm)	46.6	39.8	34.3
Left front spring	Mean	(mm)	34.3	49.63	50.13
	Standard deviation	(mm)	32.6	25.37	23.4
	Peak@99%@Mean	(mm)	82.1	52.16	47.98
Rear pivot arm Potentiometer	Mean	(mm)	2.19	4.29	4.32
	Standard deviation	(mm)	3.33	5.4	4.76
	Peak@99%@Mean	(mm)	12.2	16.5	11.85

amplitudes are considerably lower (range: 0.58 to 0.68), which also affects the standard deviation (range: 0.47 to 0.89). These numbers indicate somewhat better match than the previous section's observations of the full signals, meaning that simulated suspension response is more accurate when not exposed to strong transients like high longitudinal acceleration.

The results further show that the model greatly overestimates the mean rear pivot deflection. Moreover, the standard deviation and peak values of model response are also significantly higher than the measured data. The ratios of model to field values are more scattered than any results presented up to this point. The ratio of standard deviation ratio ranges from 1.5 to 3.3. Again, this is most likely due to the high hysteresis of the prototype's suspension.

The velocity responses of the suspensions are further derived through numerical differentiation of the displacement signals. The numerical differentiation, however,

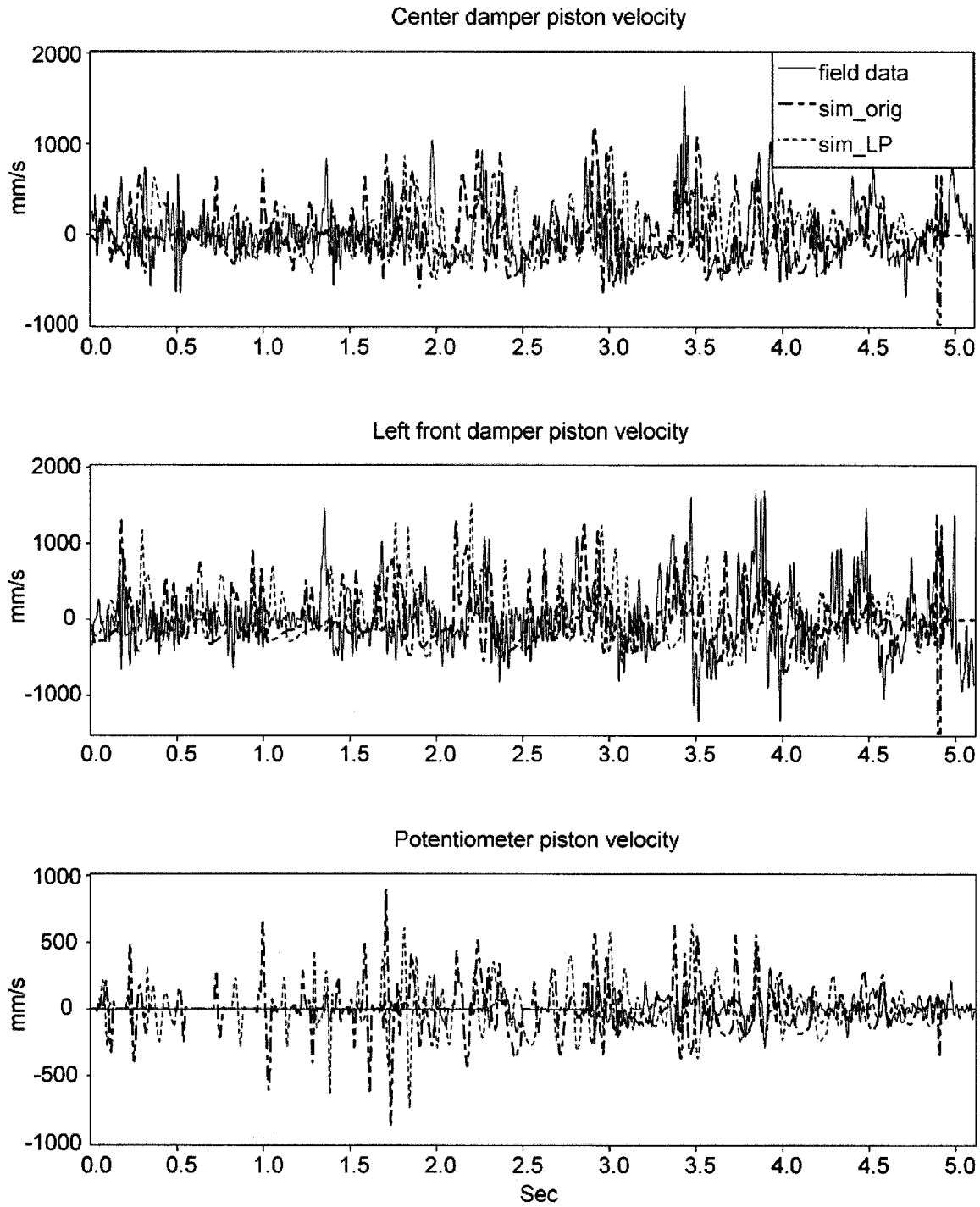

Figure 4.9: Comparisons of suspension velocities of the model with the measured data (Trail segment: 2).

resulted in excessive velocities due to presence of discontinuities in the displacement signals, particularly for segments 1 and 3. Figure 4.9, as an example illustrates

comparisons of derivatives of the central and front left springs as well as potentiometer signals, as obtained from the model results and the measured data. The results show moderate agreements in central tendencies of the spring velocities over $2.0 \leq t \leq 3.5$ s. The nature of the oscillations in the springs velocity responses are also comparable with the measured data for segment 2. The rear pivot arm velocity responses of the model for both excitations, however, are significantly larger than the measured data. This again is attributed to the scaling error previously mentioned and, to a lesser extent, to errors caused by numerical differentiation.

The model responses agreement was also examined through the histograms of the front and center suspension velocities. These histograms are compared with those of the measured data in Figure 4.10, as an example for segment 2. The similarity of the two histograms are evaluated using three criteria: dispersion span, apparent shift of their "center of mass" relative to the experimental results (not relative to zero velocity) and point of maximum occurrence.

The results show a rather narrow dispersion span for segment 2, and it was observed to be even narrower for segment 4, as expected. The center of mass of the central spring histogram is slightly shifted toward the positive velocity over segment 2, as shown. The results attained for segment 4 showed the mass center even closer to zero. For the front spring, there is a slight shift toward the negative velocity over segment 2, while this shift remained slightly toward the positive velocity over segment 4. The shifts for segment 2 are probably due to observed discrepancies in the ratios of the rebound damping constant to spring stiffness. This ratio seems too low for the center coil-over-shock unit and too high for the left front unit. In most simulations, the point of maximum

occurrence was clearly evident near zero velocity. The experimental data, however, suggests considerably lower concentration in the low speed range. This is due to the

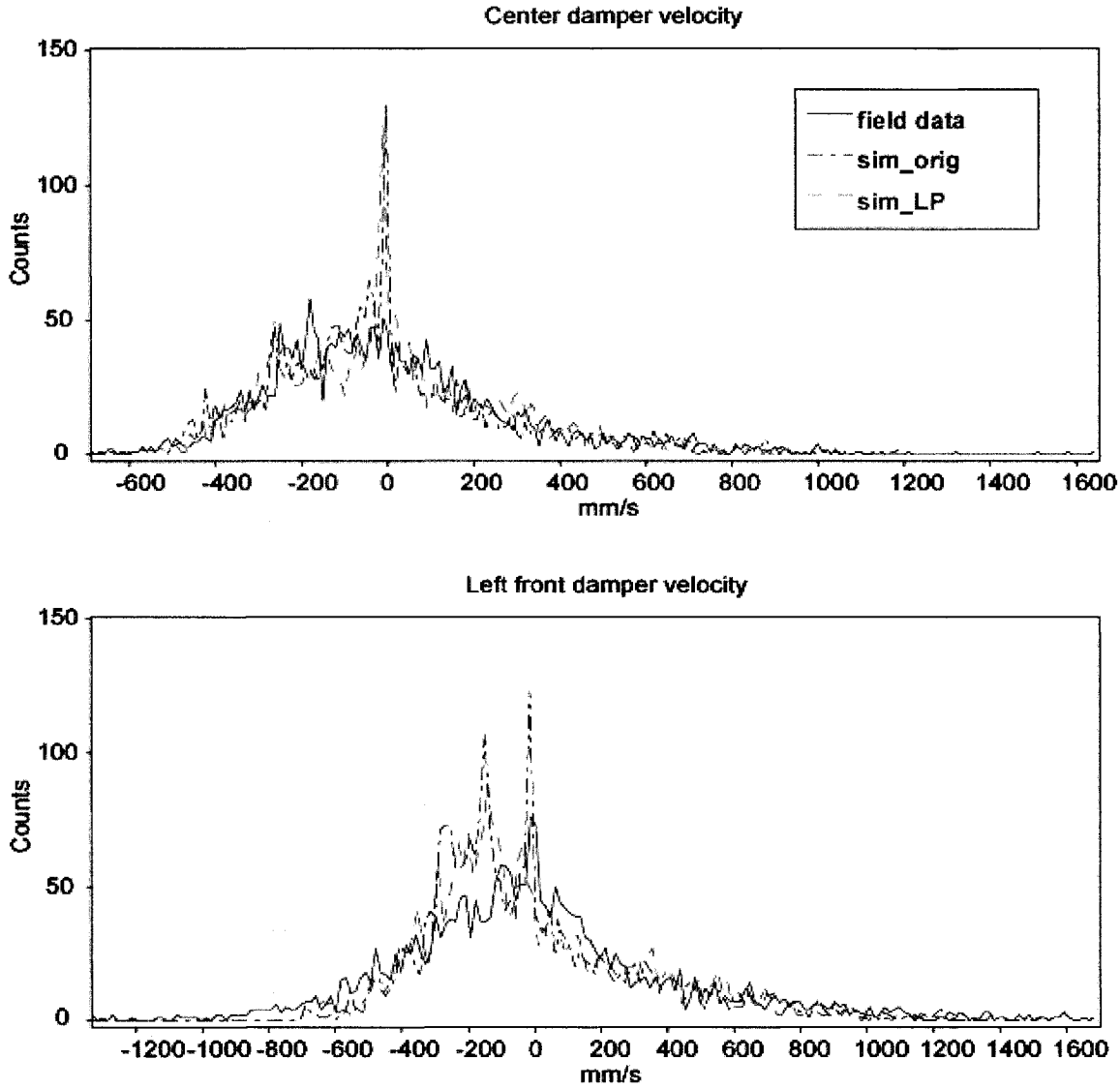

Figure 4.10: Comparisons of suspension velocity histograms of the model with the measured data (Trail segment: 2).

fact that the trail profile used in ADAMS is a sampled version of the rebuilt profile, which itself is constructed from signals sampled in the time domain. The true terrain profile is thus effectively low pass filtered three times through sampling of the ski's acceleration signals at 500 Hz, double integration of acceleration signal, and finally

through sampling of the result every 10 cm. The high frequency, and low amplitude content of the true profile, which causes the damper piston to move at varying velocities, is thus not reproduced in the profile used for simulation. This partly explains the presence of peaks close to zero in the histograms of the model results. It also partly explains the reason for the experimental signals to dominate at higher velocities.

4.3.3 Fundamental Bounce and Pitch Frequencies

The model validity can be further examined in terms of fundamental bounce and pitch mode resonant frequency, which affect the dynamic responses in a highly significant manner. For this purpose, a 2-DOF linear model of the vehicle is formulated. The parameters equivalent to those of the full vehicle model are applied to obtain estimates of the two dominant undamped chassis modes. Figure 4.11 shows the simple model structure and Table 4.5 summarizes the model parameters.

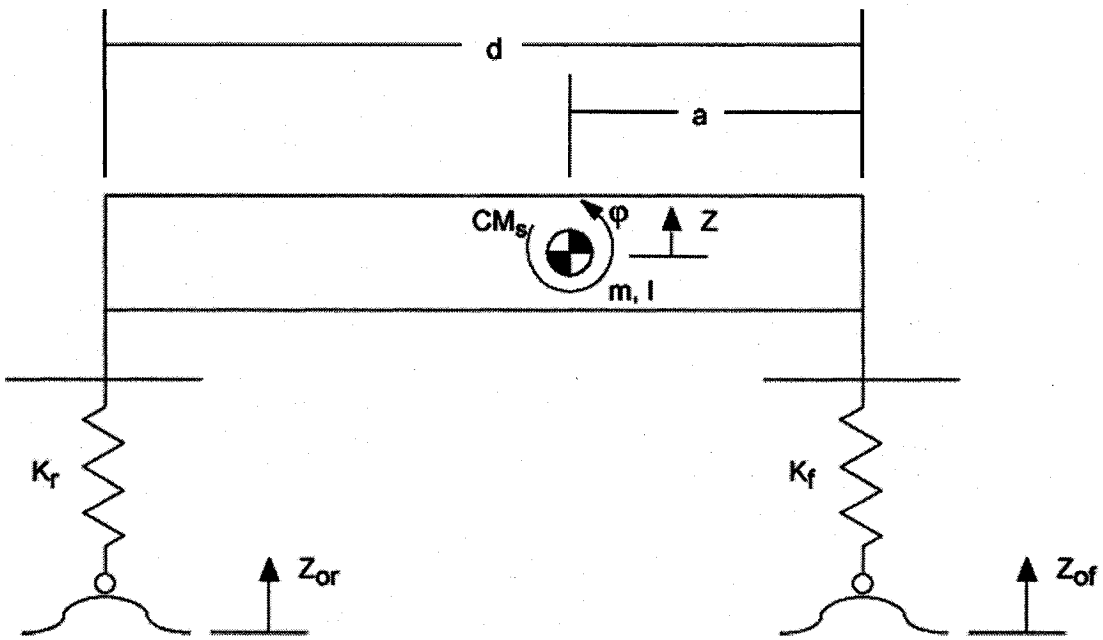

Figure 4.11: Linear pitch-bounce model diagram.

Assuming free vibration, the equations of motions of the linear model can be written in matrix form as:

$$\begin{bmatrix} Kf + Kr - m\varpi^2 & aKf - (d-a)Kr \\ aKf - (d-a)Kr & a^2Kf + (d-a)^2Kr - I\omega^2 \end{bmatrix} \begin{Bmatrix} Z \\ \varphi \end{Bmatrix} = 0 \qquad (4.1)$$

Table 4.5: Parameter values for the linear pitch-bounce model.

Parameter description	Symbol	Value	Units
Front suspension vertical stiffness at ground	Kf	10658	N/m
Rear suspension vertical stiffness at ground, horizontal rail	Kr	14141	N/m
Horizontal distance between ski pivot and rail center of pressure i.e. "equivalent wheelbase"	d	1.6319	m
Horizontal distance between ski pivot and sprung mass CM	a	1.0506	m
Sprung mass	m	307.46	kg
Sprung mass pitch inertia measured at its CM	I	108.78	kg*m²

An eigenvalue problem is formulated and solved to determine the natural frequencies, the associated mode shapes and the corresponding pitch center position relative to the sprung mass CM. The results suggested that the dominantly pitch mode occurs at a higher frequency than the dominantly bounce mode. This would be expected since the ratio of the square of the candidate vehicle's pitch radius of gyration (k) to the product of dimensions a and b (wheelbase = d and b = d-a), is about 0.61. This is considerably lower than unity, the figure for which both modes are identical and come out at the same frequency [29, 47]. Table 4.6 summarizes the natural frequencies, the dominant deflection modes and the pitch center coordinates.

Table 4.6: Natural frequencies and mode shape of the linear pitch-bounce model

Mode	Description	Natural frequency (rad/s), [Hz]	Mode shape (m/rad)	Pitch center, from CM (m)
1	Dominant bounce mode	8.782 [1.398]	-2.74	-1.759
2	Dominant pitch mode	12.47 [1.985]	0.129	0.0828

These results are compared with those derived from the simulator's two first natural modes that are evaluated from the frame frequency response functions (FRF) to ground inputs. The responses in terms of vertical motion of the sprung mass CM and the frame pitch angle to vertical displacement inputs applied at the ski pivot and at the rail, are particularly examined. The responses are evaluated under impulsive excitation of 0.001 s duration, which are applied simultaneously at the front and rear to obtain pure bounce excitation and inverted to obtain a pure pitch excitation. The influence of excitation magnitude is also investigated by varying the peak magnitude from 0.2 to 40 mm.

After rigidly locking the driver to the vehicle frame, the ADAMS model was analyzed to obtain its impulse response by first setting it to its static equilibrium, thereby defining its initial conditions. The impulsive input centered at t=0.1 s was then applied and the simulations were performed for a 5 s duration. For each run, corresponding to a specific combination of excitation type (pitch or bounce) and amplitude, the responses were exported to Matlab for evaluating the FRFs. For this purpose, a Hamming window was applied to each data series, with amplitude compensation, which was subsequently zero padded to obtain a series length of 32768 points. The input signals (excitation impulses) were also treated in a similar manner though with a rectangular weighting

window. The FFT technique was applied to derive the spectra of input and response variables, and the FRFs.

Figure 4.12 and Figure 4.13 illustrate the magnitude of vertical and pitch transfer functions, respectively, under in-phase and out-of-phase 10 mm impulse excitations. The vertical (H_z) and pitch (H_ϕ) transfer functions are derived from:

$$|H_Z| = \left|\frac{Z_{cm}(f)}{Z_o(f)}\right|; \quad \text{and} \quad |H_\phi| = \left|\frac{\phi(f)}{Z_o(f)}\right| \tag{4.2}$$

Figure 4.12 also illustrates the spectra of the vertical frame motion (Z_{cm}) and the input (Z_o). Similarly, Figure 4.13 illustrates the spectra of the pitch motion. One thing that should be noted is the form of the input spectrum magnitude that is quite different from the perfectly constant value expected of a theoretical impulse. Part of this comes from the use of smoothened, rather than triangular, impulses in order to avoid derivative discontinuities in the excitation, thereby preventing the associated numerical problems. Loading effects, or back effects, also contribute to deforming the inputs, inducing a very low amplitude sinusoidal oscillation in the parts of the time domain signals that should be identically nil. Such a phenomenon comes from the motion generators being treated as constraints by the solving algorithm and hence being subjected to optimization algorithms, effectively allowing slight violations of the constraints through a high but finite stiffness. Hence, even though the output spectrum is an "impulse response" it must be divided by the input spectrum to get a valid FRF approximation.

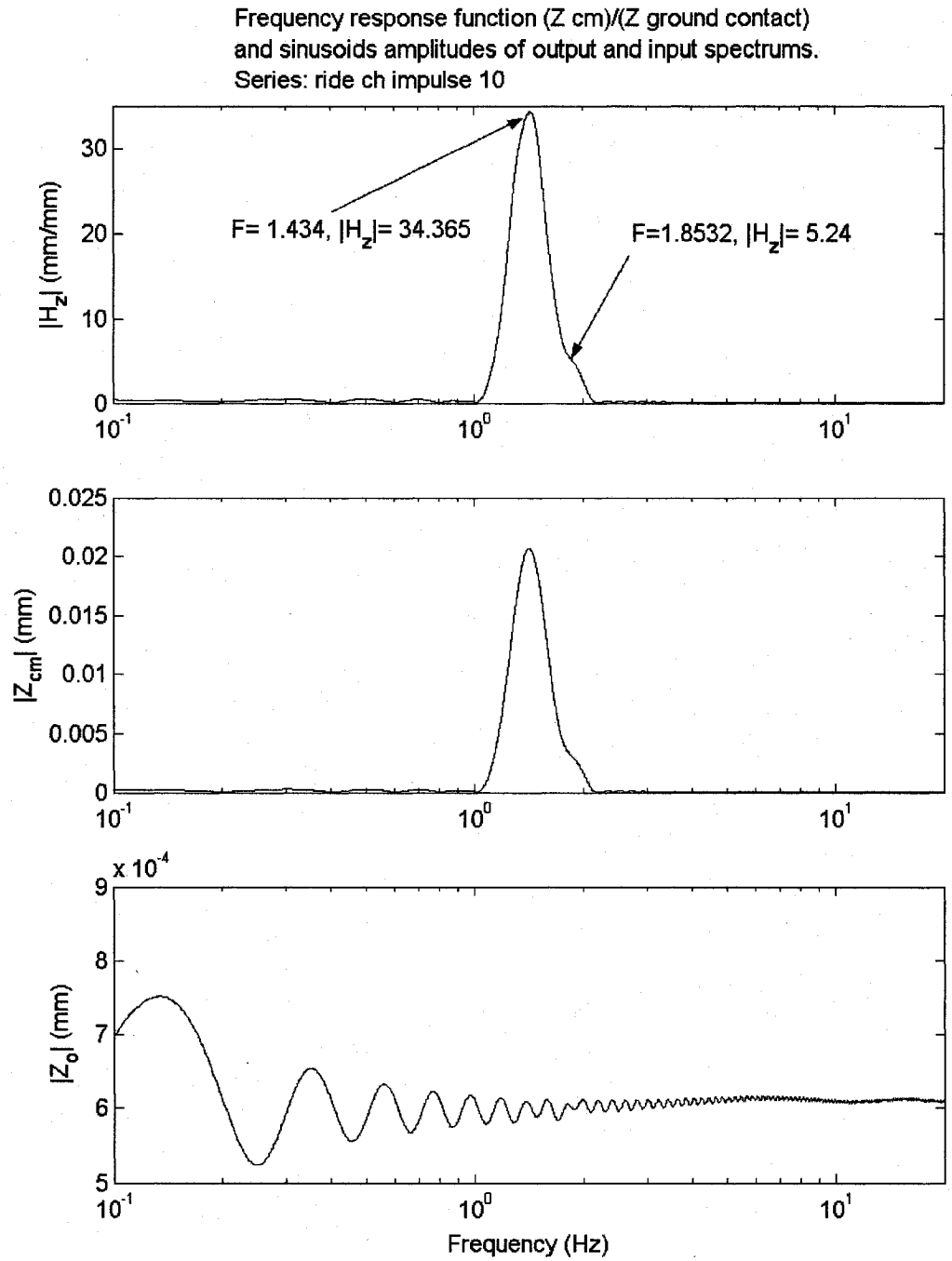

Figure 4.12: The frame vertical FRF, and spectra of the response and excitation derived from the ADAMS simulator (pure vertical excitation).

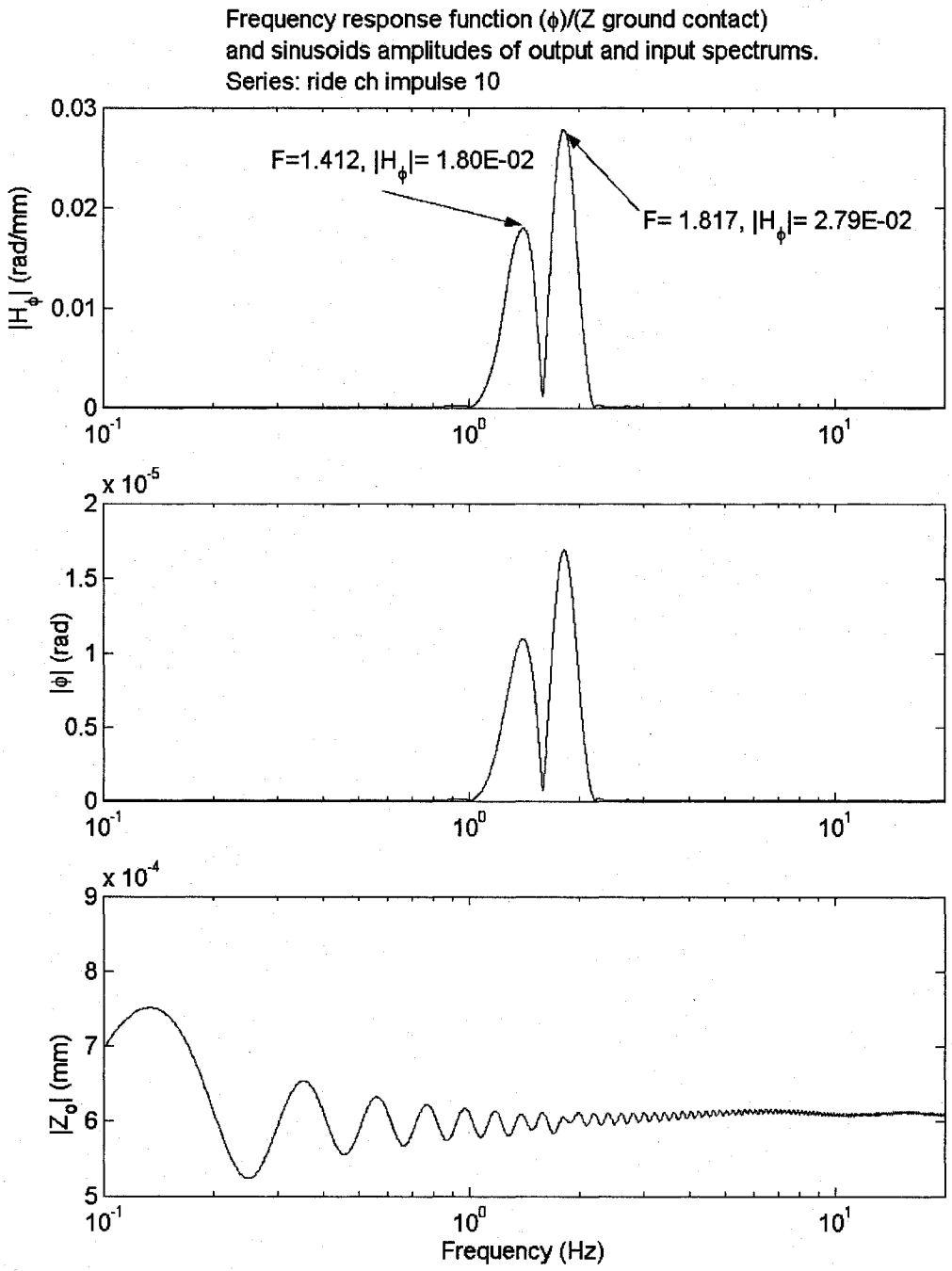

Figure 4.13: The frame pitch FRF, and spectra of the response and excitation derived from the ADAMS simulator (dominant pitch excitation).

The FRF's exhibit two distinct peaks, particularly in the pitch response, which are also evident in the frame vertical and pitch displacement spectra. These peaks occur near 1.42 and 1.83 Hz corresponding to the vertical and the pitch modes, respectively. These frequencies are also close to those of the simplified 2-DOF model, which have been presented in Table 4.6. The mode shapes can also be derived from the ratios of the vertical FRF magnitude to the pitch FRF magnitude corresponding to each mode. The analyses resulted in mode shapes of 1.91 m/rad and 0.187 m/rad, respectively, for the two modes, which are considerably different from those derived for the simplified 2-DOF model. The corresponding coordinates of the pitch center, summarized in Table 4.7, also differ from those identified from the simplified model. These differences can be attributed to the nonlinearities present in the ADAMS model, which may further reveal differences in the frequency responses with varying amplitudes of excitation.

Table 4.7: Natural frequencies and shape of the simulator's 2 first modes.

Mode	Description	Natural frequency (rad/s), [Hz]	Mode shape (m/rad)	Pitch center, from CM (m)
1	Dominant bounce motion	8.991 [1.431]	-1.902	-1.221
2	Dominant pitch motion	11.54 [1.837]	0.1869	0.120

The influence of peak excitation displacements on the frequencies and mode shapes are thus investigated by varying the peak pulse displacement from 0.2 to 55 mm. Figure 4.14 illustrates the variations in the two frequencies, and the corresponding mode shapes, when the pulse displacement is varied from 0.2 to 40 mm, while the corresponding variations in the pitch displacement range from 2.4×10^{-4} to 0.047 rad.

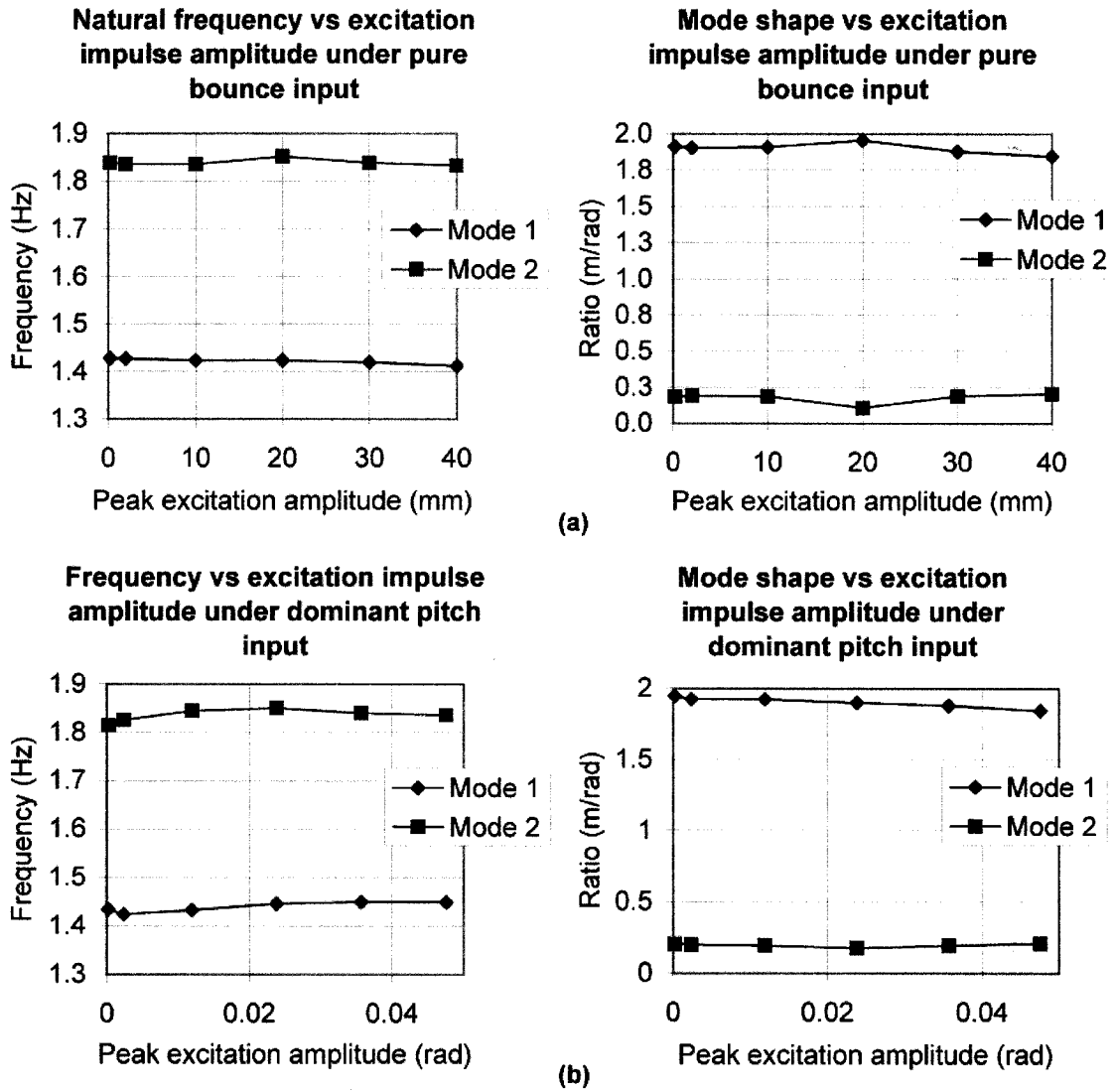

Figure 4.14: Effect of excitation amplitude on the first two natural modes of the non-linear vehicle model: (a) pure vertical input; and (b) dominant pitch input.

The results suggest that the frequencies and the mode shapes do not vary much with excitation amplitude variations. The separation between the two frequencies and mode shapes, however, increases slightly near 20 mm pure bounce impulse excitation. Such slight variations observed under both bounce and pitch excitations plots are mostly attributed to the non-linear nature of the model. The pitch mode frequency tends to

decrease with increasing excitation magnitude. Under extreme input of 55 mm bounce excitation, and the corresponding 0.065 rad pitch excitation, the models' FRF displayed a third peak near 2.7 Hz, while the pitch mode frequency decreased considerably. Hints to both changes are already perceptible on the 40 mm and 0.048 rad excitation plots. As the tendency clearly strengthens between 40 and 55 mm, investigation of higher amplitude was not judged worthwhile, the highest excitation amplitude for which the system responds in the same way as it does around its normal operating point being about 40mm.

A comparison of the mode shape of the linear 2-DOF model with those of the non-linear model suggest that the first mode shape of the latter is 30.6% lower, while the second mode ratio is 44.9% higher than that of the linear model. These differences could be due to from several causes. Firstly, the sprung mass may be low relative to the vertical stiffness, while the pitch mass moment of inertia may be high relative to the effective pitch stiffness. Both the front and rear suspension mechanisms are designed so that the skis and rail move backward as well as upward upon hitting a bump, hence causing suspension deflection to induce longitudinal movements. This effectively increases effective unsprung mass and pitch mass moment of inertia compared to static measurements. Besides, the stiffness constants used in the linear model are considered sufficiently accurate since they were taken directly from the full model. Therefore, this first factor can only play a minor role in explaining the discrepancies.

A second possible cause for deviations may be a stronger coupling of the two modes in the non-linear model. When perfect static coupling exists, the system has a double eigenvalue, and its two modes come out at the same frequency and have the same shape. The excessive separation of the simulator's mode shapes compared with those of

the 2-DOF model thus suggest that the simulator actually exhibits less, and not more, coupling. This second factor is thus also ineffective at explaining the discrepancy. In fact, linear theory appears unable to explain the observed behaviour.

Therefore, the cause must come from modeling and measurement imprecision, solving algorithm errors and non-linear effects. Simulation experiments intended to verify ADAMS accuracy for the pure 2-DOF system, the results of which follow on next page, have shown that errors on equivalent wheelbase (parameter "d") and even more on sprung CM position ("a") have a significant influence on the measured bounce motion and, with it, on both mode shape values. It should also be noted that the coupling of frame vertical motion to skis and rail longitudinal motion always induces fluctuations of "a", though of small magnitude.

Table 4.8 presents the results of several configurations of the 2-DOF model (shown in Figure 4.11) simulated in ADAMS and post-treated with the protocol used for the full model. As evidenced, the full procedure systematically underestimates the natural frequencies, by 2.5% on average. Mode shapes agreement is even poorer, although the mean error is only 0.81% for configurations having significant static coupling, like that of the full non-linear model (labeled "original"), that having $k^2/ab=1$ and the last one (a=1.25 m, $k^2/ab=0.51$). Uncoupled configurations, those having a/d = Kf/Ktot, produce very large mode shape errors, tending to infinity in two out of four cases, the others averaging 94% error. In these cases, it has been noted that the type and shape of excitation impulse (pure bounce or pitch or mixed) strongly influences the computed mode shape. Even so, the "original" configuration being significantly coupled, the procedure is judged to have acceptable accuracy for this study.

Table 4.8: Natural modes of various configurations of the 2-DOF model simulated in ADAMS compared with linear theory results.

		ADAMS		Linear theory		Error vs theory	
2 DOF model configuration	Mode	Nat. F. (Hz)	Mode sh. (m/rad)	Nat. F. (Hz)	Mode sh. (m/rad)	Nat. F (%)	Mode sh. (%) *
Original	1	1.358	-2.752	1.398	-2.74	-2.9	+0.44
	2	1.9379	0.1253	1.985	0.129	-2.4	-2.9
a/d = Kf/Ktot	1	1.4038	20.934	1.429	∞	-1.8	+100
	2	1.8921	0.1832	1.9413	0	-2.5	+ ∞
$k^2/ab = 1$	1	1.3123	-1.043	1.3452	-1.0506	-2.4	-0.72
	2	1.5159	0. 5828	1.570	0.5813	-3.4	-0.26
a/d = Kf/Ktot & $k^2/ab = 1$	1	1.3885	5.82E6	1.429	0.70	-2.8	+ ∞
	2	1.3885	-0.1126	1.429	-0.95454	-2.8	-88.2
a = 1.25 & k^2/ab= 0.511	1	1.2665	-1.7332	1.2914	-1.7391	-1.9	-0.34
	2	2.533	0.1405	2.5877	0.14026	-2.1	-0.17

* : (|simulated| - |theoretical|) / |theoretical|

Consequently, the best part of the difference between the natural frequencies and the mode shapes computed from linear theory and from full non-linear simulation results is attributed to the real system's non-linear nature and, in a lesser way, to imprecision in the identification of the 2-DOF model's parameters. For example, approximating the sprung mass using a slightly different configuration than that used to fill Table 4.5, the sprung CM is found 2.97 mm behind the point currently used for vertical displacement measurement. Considering that the pitch center of the linear model's second mode is 82.8 millimetres ahead of the sprung CM (see Table 4.6), a mere 2.97 mm error on sprung CM position would induce a 3.6% error on vertical movement amplitude.

In final analysis, natural frequencies present good agreement with a maximum error of 7.5%. Given this, the excessive separation of the simulator's mode shape

indicates that it is more loosely coupled than its "equivalent" 2-DOF linear version. Most of this is attributed to the non-linear behaviour of the 5-link rear suspension mechanism.

When subjected to an impulse excitation, the frame movement amplitude remains low, under the millimetre even for the 55 mm impulse excitation. In these conditions, with driver rigidly fixed to the frame, the full model predictions on natural frequencies about static equilibrium are close to those of linear theory and so it is assumed that it would be the same around other operating points within the normal range of motion. Thus, the simulator is considered reliable enough to submit it to forced oscillation and produce large amplitude transmissibility plots as a function of excitation frequency.

4.3.4 Forced Excitation Transmissibility

The analysis of transmission of ride vibration to the driver's location on the vehicle is one of the primary goals of the simulator development. The vertical motion of the rider's trunk is thus evaluated relative to the frame in order to study the ground-to-buttock vibration transmissibility under representative excitations. The results presented in the previous section focussed on a simplified model, where the contributions due to large frame motion, damping, track tension, ground contact characteristics and rolling resistance, were entirely ignored. Owing to the important effects of these factors, the ADAMS model incorporating these components is used for evaluation of the vibration transmissibility. The responses are evaluated in terms of frame bounce, frame pitch and driver trunk bounce transmissibility magnitudes.

In order to excite the vehicle in pure bounce, it was initially set-up to travel at constant speed on a sinusoidal profile track of wavelength equal to its wheelbase (1632

mm). This procedure, however, was considered inadequate since the rail tended to bridge over the dips, which caused high magnitude peaks in the rail normal load and the ground penetration. This effectively altered the intended input excitation. In an attempt to eliminate the bridging effect, a PD controller was formulated to regulate the torque applied to the drive axle in order to keep the vehicle speed constant at 4 m/s on a perfectly flat track, to which a motion generator imposed a vertical sinusoidal excitation. The simulation were performed under two different amplitudes of displacement excitation (Z_g), namely 0.5 and 10 mm, at different frequencies in the 0.1 to 20 Hz range. The driver buttock acceleration (A_{Zb}), the frame CM displacement (Z_c) and the frame pitch angle (ϕ_c), were evaluated, and the corresponding transmissibility ratios (normalized with respect to Z_g and ground movement acceleration A_{Zg}) are illustrated in Figure 4.15. It should be noted that the transmissibility ratios were computed from the rms values of the responses and the excitation, such that:

$$H_b(f) = \frac{\overline{A}_{Zb}(f)}{\overline{A}_{Zg}(f)}; \qquad H_{Zc}(f) = \frac{\overline{Z}_c(f)}{\overline{Z}_g(f)}; \qquad H_{\phi c} = \frac{\overline{\phi}_c(f)}{\overline{Z}_g(f)} \tag{4.3}$$

where H_b, H_{Zc} and $H_{\phi c}$ are the driver buttock acceleration, frame vertical displacement and frame pitch displacement transmissibility ratios, respectively. $\overline{Z}_g$, $\overline{Z}_c$ and $\overline{\phi}_c$ are the rms displacements due to excitation, and vertical and pitch motions of the frame. $\overline{A}_{Zg}$ and $\overline{A}_{Zb}$ are the rms values of accelerations due to ground excitation and response at the driver's location, respectively.

Figure 4.15 shows the transmissibility ratios derived under two different magnitudes of excitation magnitude. The results show relatively small influence of the excitation magnitude on the driver acceleration transmissibility (H_b), while the frame

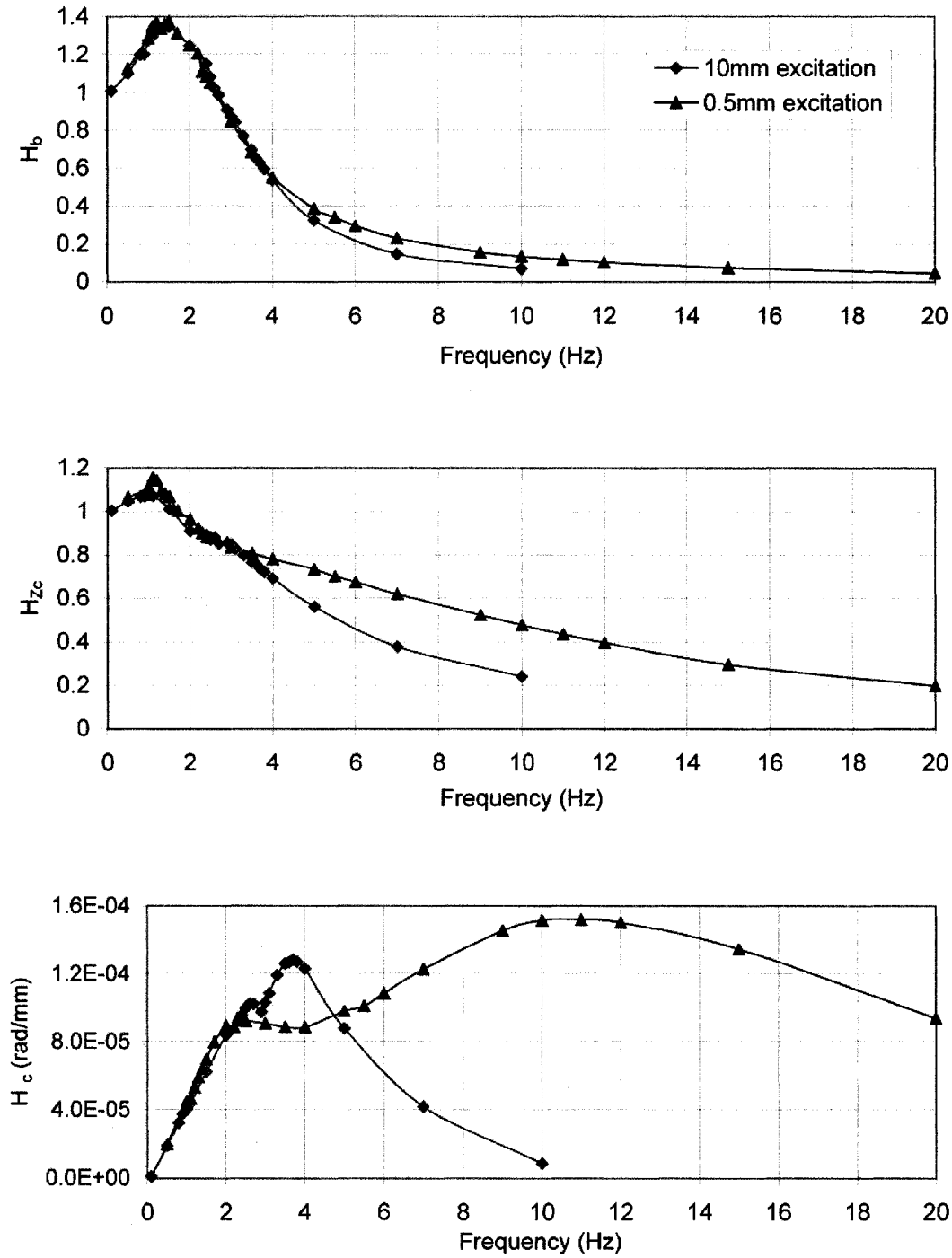

Figure 4.15: Influence of excitation magnitude on the vibration transmissibility responses of the vehicle under pure vertical excitation.

responses (H_{Zc} and $H_{\phi c}$) are strongly affected at frequencies above 3 and 2 Hz, respectively.

Under 10mm excitation, the driver bounce response peaks near 1.5 Hz, while the frame bounce and pitch responses peak near 1.1 and 3.8 Hz, respectively. The pitch response also reveals a lower amplitude peak near 2.6Hz. A closer examination of the results reveals that all three transmissibility responses present subtle local inflexions, if not clear local summits, at all these frequencies. The vehicle simulator is thus considered to exhibit three dominant modes, while a fourth relatively smaller mode is evident in the pitch plot.

The results also show that the frame bounce resonance frequency is lower than the bounce mode undamped natural frequency of the 2-DOF model, while the driver bounce resonance frequency is slightly higher. An augmented version of the 2-DOF simulator, comprising a single-DOF driver and seat representation was further analyzed and revealed resonant frequencies of 1.3, 1.46 and 2.6 Hz. The corresponding FRF responses, not shown here, clearly indicated that the frame pitch and the driver bounce motions are strongly coupled, particularly at 2.6Hz. The lower frame bounce mode frequency of the full model (1.1 Hz) is partly due to the addition of damping. The 3.8 Hz pitch peak, under 10 mm excitation, is significantly different from that obtained under the 0.5mm excitation (11 Hz).

These variations are attributed to the ground contact algorithm, which yields strongly non-linear variations in the penetration depth in certain situations. A sudden variation in the penetration in the order of a fraction of a millimetre will alter the 0.5 mm excitation pitch-transmissibility response significantly more than the 10mm one. Both

the 3.8 Hz and 11 Hz peaks in the pitch response are thus considered to be caused by the ground contact algorithm, and may not represent the pitch modes of the vehicle. The vertical transmissibility responses of the driver and the frame, however, are reasonably close under both excitations, especially below 3Hz. This suggests that the system behaviour does not vary much from very low up to moderate amplitude of motion i.e. 10 to 13mm.

4.4 Summary

Comparisons of numerous simulation results to corresponding experimental measurements are presented in this chapter in order to demonstrate the degree of accuracy of the snowmobile simulator. Static responses of the vehicle model revealed good agreements with the measured data in terms of displacements and weight distributions. The relative errors were below 6%. The results, however, suggested that relatively higher weight is supported by the front suspension and the rear pivot arm resulting in higher displacement of the front suspension, while the center spring lacked compression, due to relatively lighter load.

The dynamic response analyses revealed varying degrees of model validity under excitations arising from different trail segments. The general validity of the model could not be established over all different trails. The results obtained over segments 2 and 3 generally displayed fair to very good agreements with the corresponding measured data. Relatively poor agreements were observed for the longitudinal acceleration and velocity amplitudes, irrespective of the trail segment considered, though their general form agrees well with measured data. The relative excess in longitudinal velocity response of the

model was attributed to the inability of the current traction and ground friction models to reproduce different snow conditions.

Owing to the strong coupling effects, the discrepancies in longitudinal responses resulted in deviations in the vertical and pitch responses. The results further revealed that the rms and peak values of model responses were generally lower than those of the measured data, with the exception of the longitudinal acceleration. This was attributed to the ground rebuilding algorithm inherently low pass filtering the original profile and to the ground contact algorithm, which roughly approximated the load bearing and sinkage behaviour. The severe lack of roughness and general infidelity of the rebuilt profile was particularly noted for segment 4.

The suspension deflection responses also revealed reasonably good agreements over segments 2 and 3. The simulator, however, tended to overestimate the front springs compression and underestimate that of the center spring. The rear pivot arm motion displayed the largest deviations due to lack of consideration of dry friction in the model. The fundamental bounce and pitch frequencies of the undamped model were close to those of a simplified 2-DOF linear model. The mode shapes, however, showed larger discrepancies. Given its non-linear nature, the full vehicle model is considered to display a credible vibratory behaviour about its equilibrium point. The forced excitation transmissibility under large amplitude excitations revealed 3 dominant modes, which were close to those predicted by an equivalent linear 3-DOF simulator.

In final analysis, the simulator presents fair to good overall agreement with the real system, particularly over medium rough trail profiles where its output typically falls within ±50% of the experimental values. For a first modeling effort starting from scratch

and with limited experimental setups and data collection opportunities, this level of accuracy is judged to be good and sufficient to render a parametric analysis worthwhile, especially for demonstrating the investigation capabilities of a full non-linear snowmobile model.

CHAPTER 5

PARAMETRIC ANALYSIS

5.1 Introduction

The vehicle model or simulator, when adequately validated, can be effectively applied for deriving the design guidance to meet specific design targets. A thorough parametric sensitivity analyses could provide the essential design guidance, particularly when system non-linearity together with several design parameters are involved. Owing to the large number of design parameters associated with geometry, suspension properties and mass distributions, a method based on response surface methodology (RSM) may be applied to identify desirable design parameters in an efficient manner [48,49].

The RSM method is composed of two systematic steps. The initial step involves the identification of a goal, or set of goals, and its mathematical formulation in terms of desired response variables characteristics. Owing to the large magnitudes of low frequency vibration transmitted to the rider, the primary goal in this study is to control the level of vibration transmitted at the rider-seat interface. The second step involves three systematic phases. The initial phase, referred to as screening phase or 'Phase 0', aims at identifying the most significant parameters. This phase helps to reduce the number of design parameters for subsequent parametric studies. The 'Phase 1' involves identification of parameters values leading towards optimal design to achieve the defined goals. In this phase, a linear model is fitted to the significant parameters identified during 'Phase 0'. A gradient method is then applied to shift the significant parameters towards the region of optimal response. In the final phase, 'Phase 2', further sensitivity analyses

are performed within the optimal region to fit a higher order model and identify the optimal response point in the multi-dimensional space of the significant parameters.

In this chapter, the RSM method is applied to the vehicle model/simulator to identify the most significant parameters and their near optimal values. The response variable to be minimized is chosen as the vertical vibration transmitted to the driver-seat interface.

5.2 Metrics, Parameters and Test Protocol

As discussed in the literature review, an objective assessment of the driver comfort is a complex task. Moreover, the comfort assessments are mostly performed through different subjective and objective measures either in the field or in the laboratory [29,31]. Satisfactory simulation models for comfort assessments do not yet exist. Furthermore, the comfort performance of a vehicle may be related to an array of design environmental factors, apart from the individual factors, such as temperature, air flow, seat geometry, noise and vibration. The vibration-related comfort performance, which is the subject of concern in this dissertation, involves measurements of vibration along all the translational and rotational axes at the driver seat interface (generally, seat cushion-buttock interface and seat backrest-upper body interface) [30,32]. Although a number of seat and driver models have been developed, the validity of such models has not yet been proven to accurately predict interactions of the highly complex biological systems with the seat [35]. Considering that the vibration transmitted along the vertical axis are generally greater than those along the horizontal and rotational axes, the ride vibration analysis, as a minimum, should include the vertical-DOF of the driver. For assessing the ride vibration performance of the snowmobile simulator, the vibration-related driver

comfort metric can be simply taken as the rms vertical acceleration at the driver's buttock, $\overline{A}_{Zb}$. The selection of this response parameter fulfils the requirement for the initial step of the RSM analyses.

In the following step, a set of nine (9) parameters expected to influence the selected metric are initially identified. These parameters are summarized in Table 5.1. In the initial phase of this step, 'Phase 0', a preliminary parametric study is conducted to identify a subset of parameters that significantly influence the selected metric. For this purpose, response sensitivity to variations in the selected parameters is investigated. The lower and upper bounds of the parameters employed in Phase 0 are summarized in Table 5.1. It should be noted that the first parameter is simply the longitudinal position of the overall driver-vehicle system CM, measured backward from the ski pivot axis on the ski leg. That axis is taken to be the effective front axle. The other eight parameters are "amplifiers" of the various non-linear force-deflection and force-velocity curves of the

Table 5.1: Parameters suspected to influence driver comfort and retained for screening.

Symbol	Description	Nominal value	Lower bound (%)	Upper bound (%)
a	Horizontal distance from ski's pivot to CM (mm)	1062.26	-10	+10
K_f	Front coil-over-shock stiffness curve scaling	1.0	-20	+20
D_f	Front dampers curve scaling	1.0	-20	+20
K_{ct}	Center coil-over-shock stiffness curve scaling	1.0	-20	+20
D_{ct}	Central damper curve scaling	1.0	-20	+20
K_r	Rear suspension stiffness curve scaling	1.0	-20	+20
D_r	Rear damper curve scaling	1.0	-20	+20
K_s	Seat stiffness curve scaling	1.0	-20	+20
D_s	Seat damping curve scaling	1.0	-20	+20

springs and dampers, respectively. The variations are performed about their nominal values. All springs preload, however, are held constant, irrespective of the stiffness changes to ensure that the vehicle's original static configuration remains unaffected.

The simulation test run is performed to identify significant parameters. The significance refers to relatively strong effect of the parameter on the comfort measure under representative trails and riding conditions. The simulation protocol also has to be usable in a design context, implying that it has to ensure reasonable computation time and robustness of the test run. The protocol should be fast enough to run a typical DOE (about 30 runs) in less than 4 hours, and robust and stable so that all the runs will be completed successfully without crashes. These requirements are achieved for the virtual vehicle runs over medium roughness profile (segment 2) for a span of 33 m, which represents the first quarter of the measured segment. All of the runs were thus performed over the same trail sub-segment, while the simulation time is kept around 260 s per run. Starting at the desired steady state longitudinal velocity of 15.0 m/s and maintaining it almost constant via a proportional controller on the drive-axle torque, transients are minimizes throughout the run, making the whole process suitable for ride evaluation. Prior to launching the actual dynamic analysis, an initial condition (IC) analysis is always performed to ensure consistent ICs for all rigid bodies.

Finally, the data files from A/View are exported to the external ADAMS C++ solver, instead of being processed by the internal Fortran solver, thus greatly increasing robustness and execution speed. The C++ solver also greatly reduces the occurrence and intensity of the numerical spikes. The presence of such numerically induced peaks could significantly alter the rms acceleration response, thereby distorting the apparent response

surface. An ADAMS macro was thus written to smoothen the response. The macro is designed to identify the localized response peak values and compare them to the neighboring values to determine if the identified peak forms an outlier. When it does, an averaging is performed using the neighboring data points. The algorithm helped to effectively eliminate the single point peaks, while the medium duration, high amplitude features, such as those observed when the rear suspension bottoms out, remained unaffected. Figure 5.1, as an example, presents an overlay of the smoothened response and the original signal, which has a single numerical spike at 0.088 s and a contact-induced peak at 0.433 s. Only the spikes are eliminated, leaving the post-contact rebound and all other features intact. It should be noted that millimetres were chosen as units of length in ADAMS in order to simplify the model building process, resulting in acceleration here being given in mm/s^2.

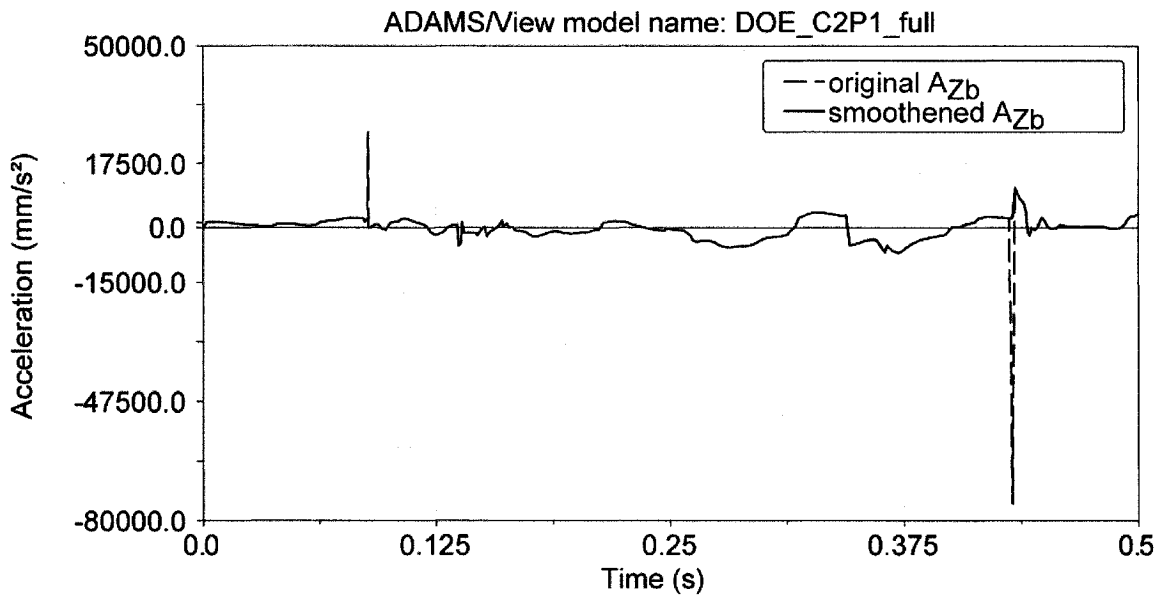

Figure 5.1: Comparison of smoothened and original acceleration response history.

surface. An ADAMS macro was thus written to smoothen the response. The macro is designed to identify the localized response peak values and compare them to the neighboring values to determine if the identified peak forms an outlier. When it does, an averaging is performed using the neighboring data points. The algorithm helped to effectively eliminate the single point peaks, while the medium duration, high amplitude features, such as those observed when the rear suspension bottoms out, remained unaffected. Figure 5.1, as an example, presents an overlay of the smoothened response and the original signal, which has a single numerical spike at 0.088 s and a contact-induced peak at 0.433 s. Only the spikes are eliminated, leaving the post-contact rebound and all other features intact. It should be noted that millimetres were chosen as units of length in ADAMS in order to simplify the model building process, resulting in acceleration here being given in mm/s².

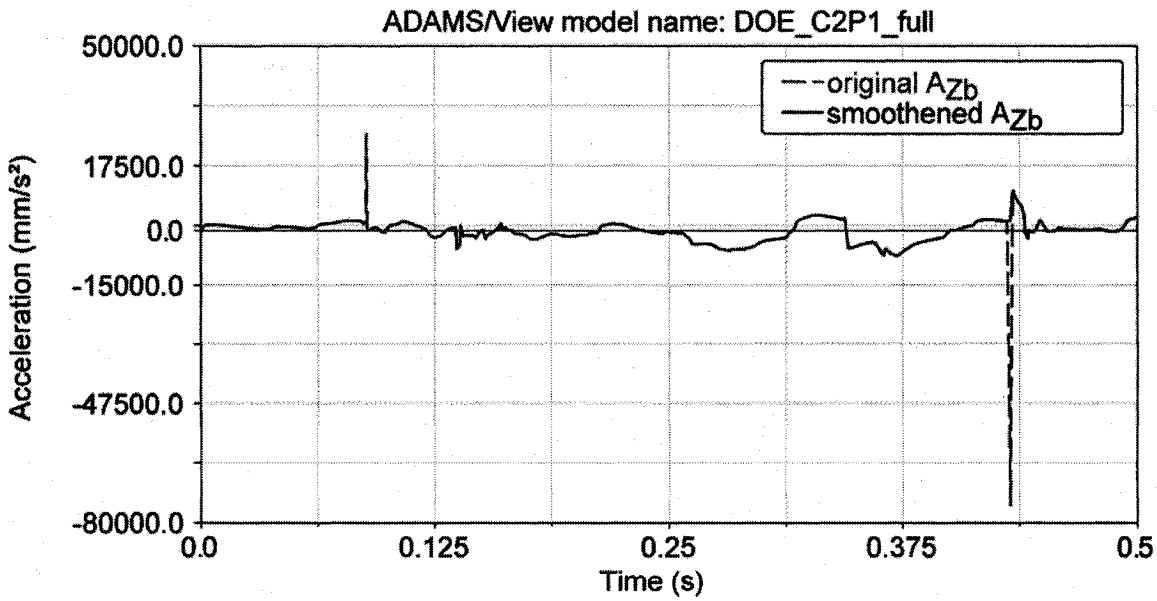

Figure 5.1: Comparison of smoothened and original acceleration response history.

5.3 Response Surface Methodology

When dealing with a simple, well-understood mechanical system it may be possible to formulate and manipulate its constitutive equations so as to identify the set of parameter values optimizing one or more response quantities of interest. The vast majority of mechanical systems, however, exhibit non-linearities, and thereby the direct manipulations of their equations of motions could be an overwhelming task. The optimization of a response variable y for such systems could be realized by building a simulation matrix in order to identify the parameters x_i that have a significant influence on the response. A simplified polynomial model describing the evolution of the response in terms of the significant parameters may then be formulated. In case of two or more significant parameters, the resulting model would be of the general form $y = f(x_1, x_2) + \varepsilon$, with ε representing the error between the system and the model outputs. A plot of the response y against x_1 and x_2 would yield a surface approximating the system response over the concerned parameter range, hence the "response surface methodology" name [48].

The application of the RSM requires the nominal or reference response, which is used to judge the relative improvements, if any, attained from a particular parameter variation. In this study, the reference signal is derived using the default or nominal values of the selected 9 parameters, while operating on segment 2 at a forward speed of 15 m/s. Figure 5.2 illustrates the seat acceleration response, A_{Zb}, for the reference test run, obtained using the parameters' nominal values. The reference signal is free from numerically-induced peaks, and the rms acceleration was obtained as 4143 mm/s^2. An examination of the frame responses and the graphical animation revealed that the average

frame pitch angle is negative and that the driver's predominant motion occurs along the vertical axis. The reference simulation did not show any interaction with the suspension bump or the rebound stop, suggesting that part of the suspension travel is left unused.

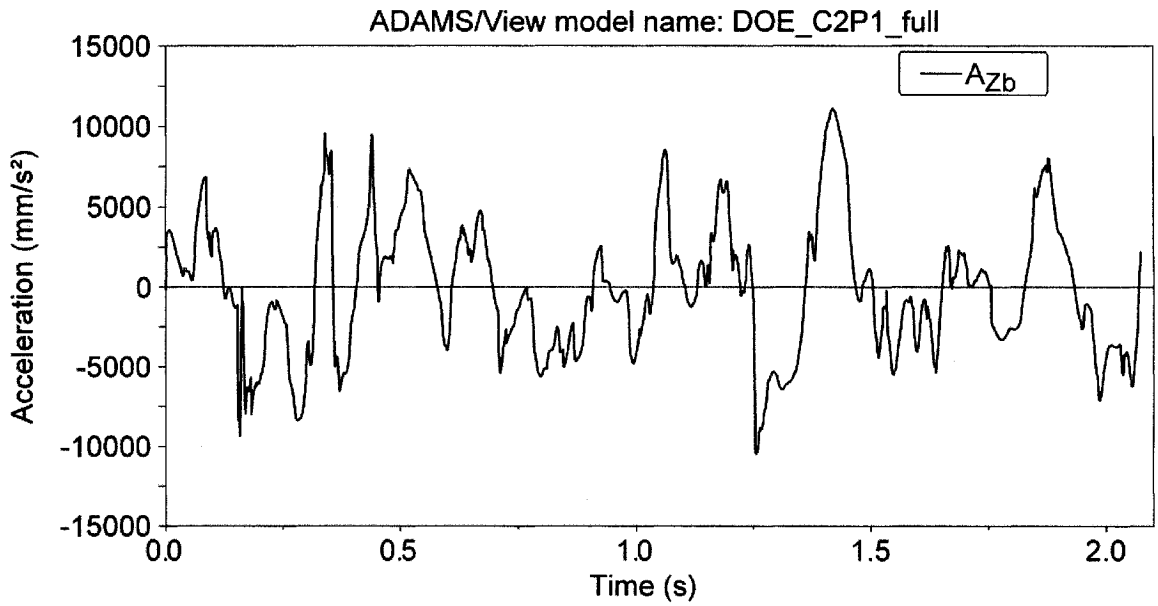

Figure 5.2: Reference acceleration response at the seat-buttock interface (Trail segment: 2; speed: 15 m/s)

Two different tools are used to perform the RSM. The first one is the ADAMS/Insight DOE module, integrated within ADAMS. It partially automates the elaboration of the parameters design matrix, and performs all its runs in a batch mode, automatically compiling the results in the augmented design matrix. Since this module offers only limited analysis capabilities, Design-Expert 7 (DX7), a dedicated design and analysis of experiment software from Stat-Ease Inc. [48], is used to derive the regression models. While both software returned identical fitted models, DX7 was considered preferable since it provides the user with significantly more evaluation tools. Several DOE graphical results presented over the next pages come from it.

5.3.1 Phase 0: Screening Experiment

Screening aims at identifying which of the proposed parameters, called "factors" in DOE, have a significant effect on the response and must consequently be retained for the following phases. This step is therefore decisive for the RSM analysis. The influence of each factor is assessed by assigning them two levels, a "low" and a "high", using the bounds defined in Table 5.1. Various combinations of the factor levels are used sequentially and the value of the response variable is recorded for each trial. The resulting set of response values is then used to approximate the factors' effects. An experiment involving the "full factorial" design, would require 2^9or 512 trials. This would offer the highest possible resolution, not only on the effect of each parameter (main effect), but also on their interactions and even on the second or higher order effects (i.e. response dependence on the square of a factor value, etc.) The screening, however, is generally performed with primary focus on the main effects, so unnecessary resolution is traded for fewer trials. In physical experiments, as opposed to virtual ones, some random variability is expected in all measurements as well as in the system behaviour itself so some or all trials are normally replicated (i.e. ran several times) thus allowing approximation of pure random error magnitude. Multi-body simulation environments, being entirely deterministic, exhibit no random error whatsoever, rendering replication useless.

From here on, some DOE specific vocabulary and concepts will be used when appropriate without being defined and explained at length, such information being available from statistical textbooks and/or RSM manuals [49, 48].

Given the peculiarities of screening a virtual model, an unreplicate, 2^{9-3} fractional factorial design having 64 different trials (i.e. $2^{9-3} = 2^6 = 64$) was selected. It is of resolution IV, thus preventing the main effects from being aliased among themselves and with any two factors interaction terms. They can however be aliased with three factors interaction terms while two factors interaction terms may be aliased among themselves.

The screening results suggested that five factors significantly influence the response. In order of decreasing significance, these are the seat damping (D_s), the rear damping (D_r), the seat stiffness (K_s), the rear stiffness (K_r) and the front stiffness (K_f). The influences of the various factors were evaluated using four different techniques, which invariably led to the same conclusions. Firstly, a linear model was fitted to the results. Its terms, each corresponding to a factor, were then sorted in order of increasing P-value (the probability that the factor's real effect on the response be nil given the effect approximation obtained from the experiment). The terms were also sorted in decreasing order of absolute value of the beta coefficients (β), which are a measure of the factors effect in the coded variable space, or a standardized measure of factors relative influence [48]. Table 5.2 presents the P-values and β in the ascending and descending orders, respectively, and the corresponding term. The results show that both rankings follow identical order of the terms, except for the constant term, which is simply the average of all the observations.

The third technique used is known as half-normal probability plot. The one produced by Design-Expert is reproduced in Figure 5.3. When a random sample from a normal population is plotted on normal probability paper, the points tend to fall on a straight line. Conversely, there must be some strong influence estranged to the

Table 5.2: Screened factors ranked by increasing P-values and decreasing β coefficients.

Rank	P-value		Absolute beta	
	P-value	Term	abs(beta)	Term
1	3.10E-38	D_s	0.80538	D_s
2	1.11E-31	constant	0.48003	D_r
3	5.46E-27	D_r	0.2536	K_r
4	4.98E-15	K_r	0.13763	K_f
5	3.15E-07	K_f	0.068363	K_s
6	0.00542	K_s	0.044595	D_f
7	0.064091	D_f	0.028497	K_{ct}
8	0.23234	K_{ct}	0.01087	D_{ct}
9	0.64681	D_{ct}	0.005521	A
10	0.81585	A	3.21^{E}-15	Constant

hypothetical normal population to send a point far off from the line [48, 49]. An outlier to the linear regression line would thus characterize a truly influent term.

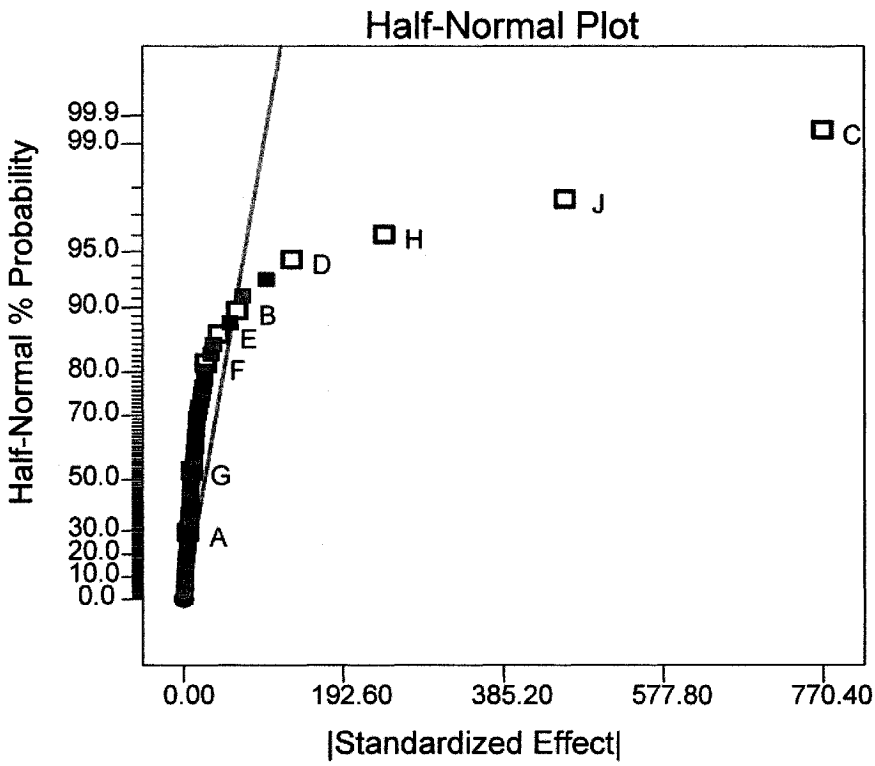

Figure 5.3: Half-normal probability of the effects of the screened factors.

In Figure 5.3, the letters A to J are the "coded variables" of the nine factors considered. The coding simply means centering and scaling all natural variables ξ_i independently using the following relationship to obtain a set of new "coded variables" x_i :

$$x_i = \frac{\xi_i - [\max(\xi_i) + \min(\xi_i)]/2}{[\max(\xi_i) - \min(\xi_i)]/2} \tag{5.1}$$

The above variables have nil central value and unit range, making them directly comparable. Table 5.3 presents the coded variables and the corresponding physical variables.

Table 5.3: Coded to normal variables equivalency as used for screening.

Coded variable	A	B	C	D	E	F	G	H	J
Normal variable	a	K_s	D_s	K_f	D_f	K_{ct}	D_{ct}	K_r	D_r

Figure 5.3 presents all the terms that can be estimated using the selected experiment design, which in this case includes most of the two-factors and some three-factors interactions along with the main effects. Factors C (D_s), J (D_r), H (K_r) and D (K_f) clearly dictate most of the response, followed by the interaction terms EJ and EF, respectively (not labelled on the graph). These interaction terms precede term B (K_s), the last main effect term right of the regression line. That line is automatically updated each time a term is excluded (i.e. highlighted) from the assumed normal sample, and is thereby included in the fitted linear model. Term E (D_f) was not identified as a significant variable, in spite of strong interactions EJ and EF dominating term B, partly because it

fell left of the regression line and partly because of the desire to limit the following RSM phases to 5 factors, if at all possible, due to time and resources requirements issues.

Variation of factor "a" by ±10% clearly produced the lowest main effect, almost nil, on the response while ±20% variations of C (D_s) and J (D_r) dictated strong response variations. None of the central coil-over-shock factors, F (K_{ct}) and G (D_{ct}), showed a significant effect. This suggests that the driver's vertical motion is primarily generated by two phenomena: the pitch motion induced in part by the front suspension excitation, and the vertical excitation arising directly underneath the driver. The central damper does not see much excitation from pure chassis pitch but is highly excited under strong rail pitch motion relative to the frame. For instance, this may occur when a sudden harsh bump or short mogul is encountered.

Design-Expert graphical presentation of the factor's effect makes the conclusions especially clear and easy to interpret. The fourth and surely most striking evaluation technique is that of the main effect plots, presented in Figure 5.4. The I-beam drawn at both low and high level points are least significant difference bars. They represent the 95% confidence interval on the average response value for the plotted factor's low and high values with all other factors set at their central value. If the I-beams overlap horizontally, the factor's effect cannot be said to be significant. Once again, the five significant factors stand out. These include: C (D_s), J (D_r), H (K_r), D (K_f) and B (K_s). Since all the four evaluation techniques point to the same factors, the subsequent RSM phases can be undertaken confidently knowing that the remaining factors will not affect the response considerably.

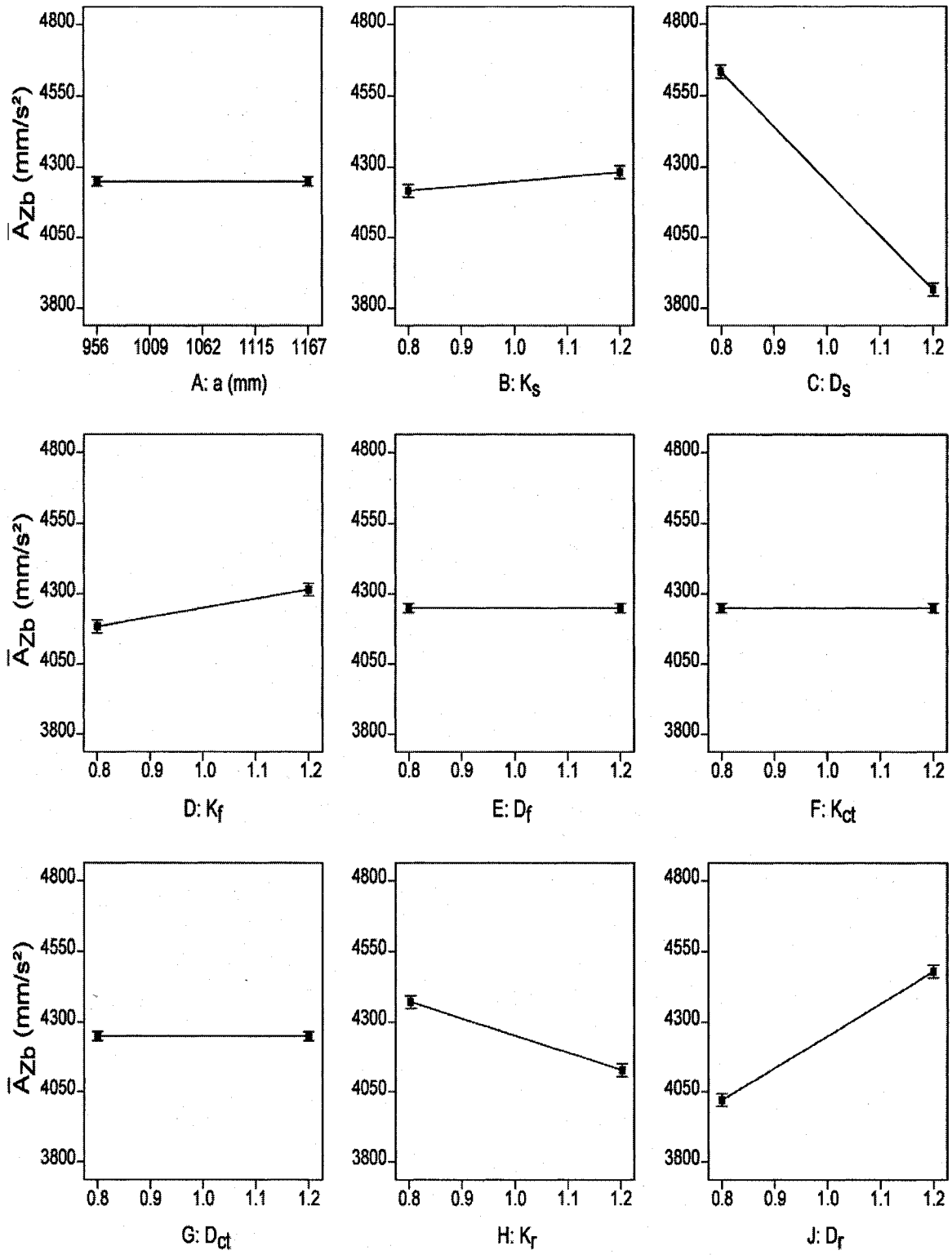

Figure 5.4: Main effects of the selected variables used for screening.

5.3.2 Phase 1: Identification of an Optimum Response Region

The identification of the optimum response region involves a 2 level fractional factorial experiment. A linear regression model is then used to describe the results and several trials are performed using sets of factor values corresponding to successive increments along the model's gradient until the response reaches its minimum. This is known as the method of steepest descent [48].

First, a 2^{5-1}, resolution V experiment is performed on the five significant factors around their default values using the same variation ranges as in Phase 0 (Table 5.1). The results and the corresponding regression models are slightly different from those identified in the screening phase due to the absence of the weak but finite effects of the excluded factors. The obtained linear regression model is as follows:

$$\overline{A}_{Zb} = 4910.8 - 1891.91D_s + 1139.84D_r - 472.41K_r + 369.48K_f + 149.03K_s \quad (5.2)$$

The increments along the first gradient are chosen as listed in Table 5.4, and are applied to each factor in order to move it one step along the negative direction of the gradient, so as to decrease its response. Both equation 5.2 and Table 5.4 are expressed in natural variable units. Simulations are performed at successive intervals and the response is monitored to identify its minimum value.

Table 5.4: Increments along the first gradient.

Term	D_s	D_r	K_r	K_f	K_s
Increment	0.2	-0.1205	0.04994	-0.03906	-0.01575

Figure 5.5 illustrates the variation in the target response ($\overline{A}_{Zb}$) with the number of increments along the first gradient. The results suggest rapid decrease in $\overline{A}_{Zb}$ with increasing increments.

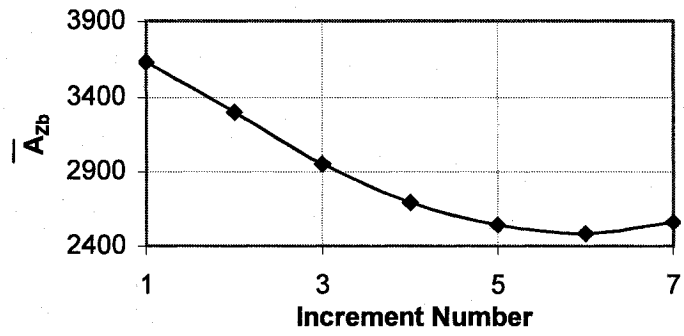

Figure 5.5: Variations in the rms acceleration response with number of increments along the first gradient.

The initial rate of change, however, fades as the parameter values move farther from the region used to fit the linear model and as the response approaches its minima. A second steepest descent sequence was further performed, where the central point is taken as the sixth increment point of the first sequence. This process led to a point expected to be close to the overall region of optimality.

A more refined experiment, using the so-called D-optimal design and involving 4 levels per factor and 64 runs, was then performed around the identified point. This allowed fitting either a linear, linear with interactions, quadratic or cubic model, whichever fit best. Due to significant curvature the cubic model turned out to be ideal but the studied region (called the "region of interest") still did not contain a local minimum, contrary to expectations. A linear model was therefore fitted to the data and the method

of steepest descent was used once more to move to a point presenting an even lower response. This point served as the new central point.

In an effort to limit the computation time, the experiment performed about this new point was of central composite design (CCD) type, involving 5 levels per factors but requiring only 28 runs. This design allows for deriving regression model up to second order (without aliasing the main effects), which in this case provided the best fit. However, the region of interest once again did not include a local minimum. Consequently a linear model was used to perform a final steepest descent sequence. At this point, defined by factor values $D_s = 15.6$, $D_r = 0.43$, $K_r = 1.12$, $K_f = 0.73$, $K_s = 0.91$, the response value was 738 mm/s^2, less than 1/5 of its original reference value.

Although the identified near optimum point could yield significantly lower transmitted vibration than the original setting, the benefits could not be fully realized in practice since using those parameter values would significantly alter the vehicle's behaviour, rendering it unusable over trails harsher than that used in the test run. The results of Phase 1, however, gave the experimenter a good understanding of the effect of each factor and an idea of their ideal value. The optimal seat damping (D_s), which is the most significant factor, would most likely tend to "lock" the driver to the chassis. Setting the D_s value sufficiently high, the system starts to move like one single large mass oscillating on its suspension, rather than like two masses oscillating relative to each other as well as to the ground. Up to 25 times the original seat damping has been tried. Any further increase in D_s resulted in even lower value of the response, which suggests that a practical optimum value for seat damping most likely does not exist. A high value of seat damping constant, however, clearly seems desirable.

The rear suspension stiffness K_r converged to approximately 1.14 times its nominal value, ensuring that the chassis typically operates around a point a little above half its suspension travel. The severity and frequency of impacts against both the compression and extension stops is thus minimized. This value can consequently be considered as the practically realizable optimal value. Its slight increase (+0.14) over the default setting is attributed to the presence of the data acquisition hardware adding 18 kg to the rear of the vehicle.

Lowering K_f reduces pitch velocity and amplitude, thereby reducing vertical acceleration of the driver's buttock since the driver is seated some distance aft of the pitch center. As for D_s, the response keeps on decreasing with any further reduction of front stiffness up to unreasonably soft levels. K_f should therefore be set to the lowest value preventing excessive bottoming in "harsh" conditions.

Lowering D_r up to very low levels simply reduces the ground to frame vibration transmissibility (while operating away from natural frequencies), as predicted from the widely-reported linear 2-DOF quarter car models [19,41,47]. A lower value of D_r, however, causes larger frame motion amplitude and potential for impact against the end stops, particularly the compression ones. These contacts induce harsh vertical shocks directly transmitted to the driver, especially when a higher seat damping (D_s) is selected. The optimal rear suspension damping would thus present the lowest value that allows for the use of most of the suspension range, while preventing impacts against the limit stops.

Lastly, the seat stiffness (K_s) only had a marginal effect on the response. After its initial reduction during the first steepest descent sequence, the second experiment in Phase 1 revealed that its effect was more than five orders of magnitude weaker than that

of the next weakest main effect. K_s was consequently left out of subsequent experiments, its value being kept constant at 0.91.

5.3.3 Phase 2: Optimum Response Point

As discussed above, only two of the five studied factors may have an optimum value while allowing the system to retain its normal configuration. Even though "ballpark" values have already been identified in phase 1 for these two factors, phase 2 is performed in an attempt to isolate a point of clear optimal response, thereby completing the full RSM procedure.

This requires assuming realistic values for the three factors left out. For this purpose, the seat damping was increased four fold (D_s = 4.0), which could perhaps be obtained by using alternate polyurethane foams. The front suspension stiffness was lowered to 60% of its original value (K_f = 0.6). Any further reduction in K_f would result in unreasonable lowering of the nose and significant reduction in the available front compression travel. The seat stiffness parameter is retained at its Phase 1 level (K_s = 0.91).

A D-optimal experiment is performed on the rear suspension stiffness and damping, around K_r = 1.14 and D_r = 0.3, which are believed to be close to the optimum values based on the Phase 1 analysis. Fitting a cubic model to the results revealed a point of minimum response near K_r = 1.133 and D_r = 0.265, as shown in Figure 5.6. The surrounding optimum region is bounded by four design points (simulated test run results, indicated by small circles/dots) with the hypothetical optimum point close to the middle and hence relatively far from any design point.

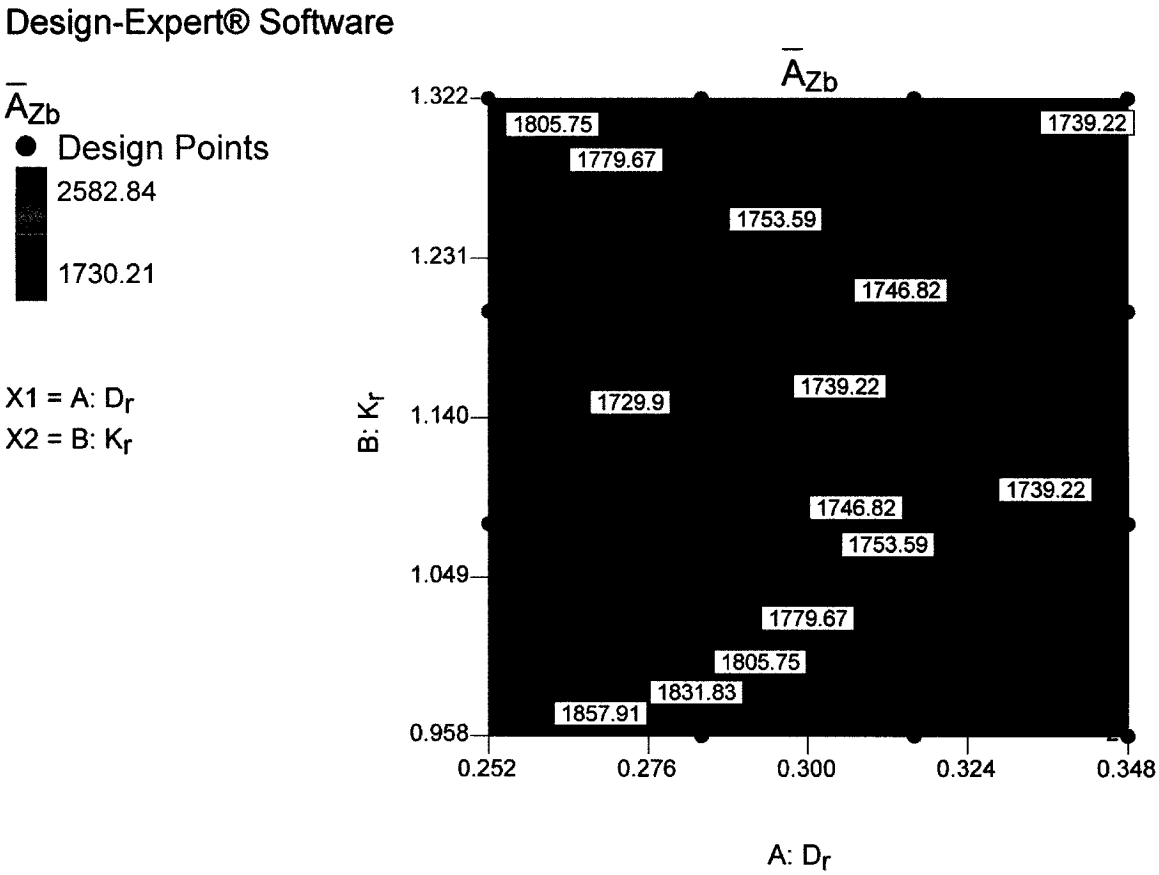

Figure 5.6: Surface contours of the response ($\bar{A}_{Zb}$) with varying values of K_r and D_r.

In order to confirm the existence and shape of the optimum region, a higher resolution result set is needed. Another experiment, using the Face Centered Cubic (FCC) design, is therefore performed in the region defined by $1.065 < K_r < 1.202$, and $0.250 < D_r < 0.282$. Figure 5.7 shows the resulting quadratic response surface approximation. The upper and lower left hand corner points are close neighbors to the corresponding points in Figure 5.6, and exhibit nearly identical response, while the other points are new and increase the resolution considerably. As can be seen, due to its lower resolution, the previous experiment failed to detect the ridge of increasing response going from the middle right to the top left portion of the region of interest. Clearly, the expected optimum point does not exist and the response surface significantly differs from the

previous approximation even though its range of response (1731 to 1757) is quite comparable to that expected from Figure 5.6.

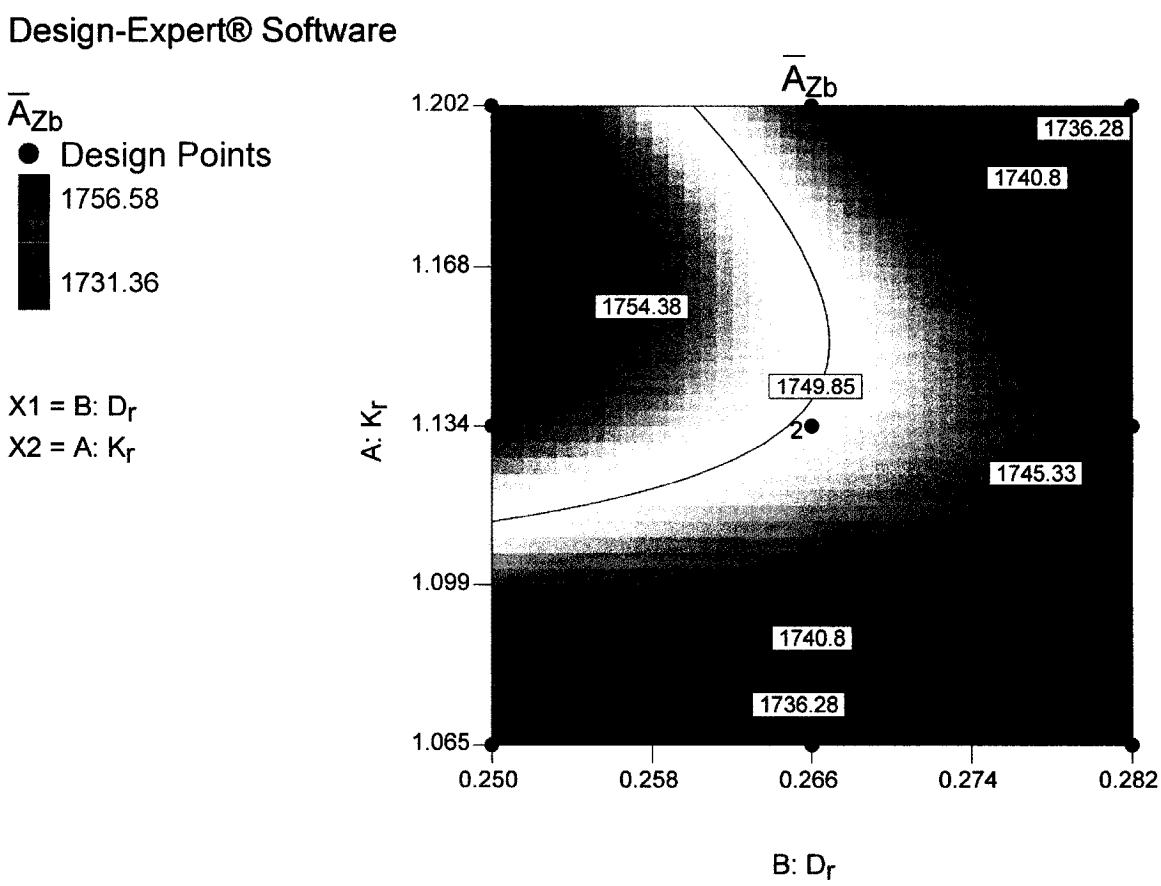

Figure 5.7: Focussed high resolution experiment refuting the existence of an optimum region.

In an attempt to clearly understand the system behaviour, a final experiment is performed on a larger region using a "space filling" type of design, a Latin hypercube with 30 trials. Figure 5.8 shows that the response remains almost constant over a large region of the upper right corner. As a guideline, all points in the experiment's region of interest falling above the line passing through $[D_r, K_r] = [0.22, 1.084]$ to $[D_r, K_r] = [0.329, 0.95]$, that is the line defined by $K_r = -1.229\ D_r + 1.354$ and drawn in light tint in Figure 5.8, can be considered equally good. Not only does the fitted cubic model predicts

little response variation over that region but the response values of its design points are rather constant, ranging from 1714 to 1768 mm/s² for a total variation of about 3 percent.

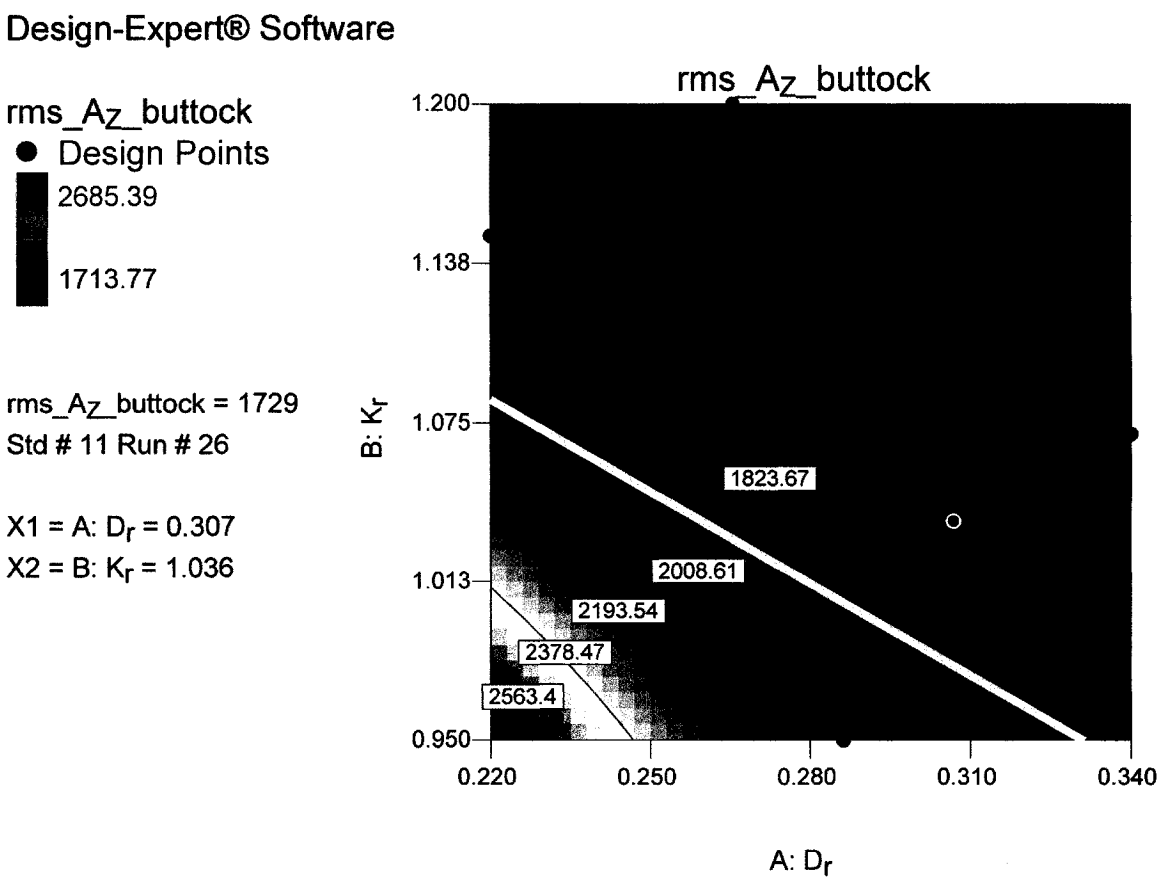

Figure 5.8: Space filling experiment showing a large region of constant low response.

The results from the last three experiments suggest the absence of a clearly identifiable unique optimum point, while a region of low and almost constant response is clearly evident. Moreover, none of the three fitted models could be used to accurately predict the response. The only model fitting its design points reasonably well is that from the first experiment, which provided high coefficient of determination R^2 of 0.9885 (adjusted R^2 of 0.9678 and prediction R^2 of 0.7970). The shape of its fitted surface, however, has clearly been proved erroneous by the second experiment design points.

Although it failed to identify an optimal point, the Phase 2 analyses highlighted two important characteristics of the system behaviour.

Firstly, it revealed where in the D_r, K_r space does the rear suspension starts to impact against its bump stops. This happens in the region below the light tint line dividing Figure 5.8. Observation of the response value vs the increment curves of Phase 1 (equivalent to Figure 5.5 but for the third and fourth steepest descents), together with the design points of the lower region of Figure 5.8, reveals that the response value increases suddenly with the occurrence of the first contact, when D_r is decreased beyond a certain value. Subsequent reductions in D_r initially reduce the response somewhat from its newly increased level before leading to the advent of a second contact, itself increasing the response another step. Such step-like behaviour obviously cannot be accurately described by a relatively low order (<4) polynomial. Although it fails to capture the stepwise behaviour, the cubic model of Figure 5.8 shows an exponential increase in the response when operating at low K_r and D_r values.

A second characteristic revealed by the last experiment of Phase 2 is evident from the amount of variability between the neighboring points, that is points close to one another in the factor space (K_r, D_r). Such variability can be observed even for points lying in the upper-right region of almost-constant response. The largest response difference observed is that of the highlighted point in Figure 5.8 (encircled point near K_r=1.03 and D_r=0.305) and its two neighbors, respectively having $\overline{A}_Zb$ = 1729, 1757 and 1759 mm/s². Not only is this a large difference for such close points but it is particularly remarkable given that the highlighted point is actually in between its two high-response neighbors, along both axes. These local differences may appear as random variations in

the analysis of variance (ANOVA) and to the corresponding fitted cubic model. However, they are of a different nature than the usual physical experiment's "random errors" since the test set-up used here is a deterministic numerical model.

Part of the variability is attributed to small, yet unexplained, response differences ($< 2mm/s^2$) observed when performing a given test run along with several others in batch mode as opposed to running it alone directly in A/View without using A/Insight. Repeating a given single test run in A/View several times always returned the identical same results, as does running several times a full DOE in batch mode using A/Insight. The root cause of the occasional slight discrepancies between single and batch modes has not been identified, but the operating system's (in this case Microsoft Windows XP Professional) way of attributing priorities to the different running processes is suspected.

The best part of the variability must hence come from the solver idiosyncrasies and, of course, from the behaviour of the model itself. Executing the highlighted run of Figure 5.8 once more and, separately, executing one of its two neighbors and over-plotting their time domain A_{Zb} signals, as well as the corresponding macro-processed signals, reveals several things. First, the macro does not alter the signals in any way, which is consistent with the fact that none of the original signals present spikes. The macro hence does not contribute to the difference in response of the two runs. Second, the two signals present two types of differences: there are occasional small temporary offsets and there are discrete features, like small single-point spikes, which appear here and there, once in one signal and then in the other. Being of low amplitude compared to the signal's major oscillations, the discrete features can only have a marginal effect on the rms value. So, most of the response difference between treatments must come from

the local offsets, pointing to real differences in the overall system response. Indeed, the slight changes in parameter values affect the forces developed and thus modify the path taken by the rigid bodies while moving over the trail. For instance, over-plotting the signals from the two runs shows that at 1.038 s into the test run, or about halfway, the vehicle's CM in the run corresponding to the highlighted design point of Figure 5.8 is 3mm in front of that of the other run. Overlaying both animations confirms this and reveals other similarly low magnitude differences. Consequently, most of the response variability between neighbor points is attributed to actual differences in the system behavior due to the small parameter value changes. This illustrates how complex the system is, which leads to the conclusion that finding a clear unique optimum point through RSM with this kind of numerical model is unlikely, regardless of the response variable to optimize.

Even so, arbitrarily choosing a point in the upper-right region of Figure 5.8 and performing the test run will return a significant buttock acceleration reduction over its original value. Selecting a point near the middle of the upper region, for instance D_r= 0.29 and K_r=1.12, and performing the test run returned response $\overline{A}_{Zb}$ = 1752.5 mm/s², which is 42 % of the reference value. Figure 5.9 illustrates a comparison of the A_{Zb} signal corresponding to the selected point (referred to as optimal) with the reference response. Most of the gain comes from the strong amplitude reduction of long-duration features, while the low-amplitude and higher frequency oscillations remain almost the same. These results are obtained with all seven other factors set to their Phase 2 level, that is: K_s= 0.905, D_s=4.0, K_f=0.6, D_f=1.0, K_{ct}=1.0, D_{ct}=1.0, a=1062.26 mm. The reduction in the response was further confirmed by the graphical animations of the driver's motion.

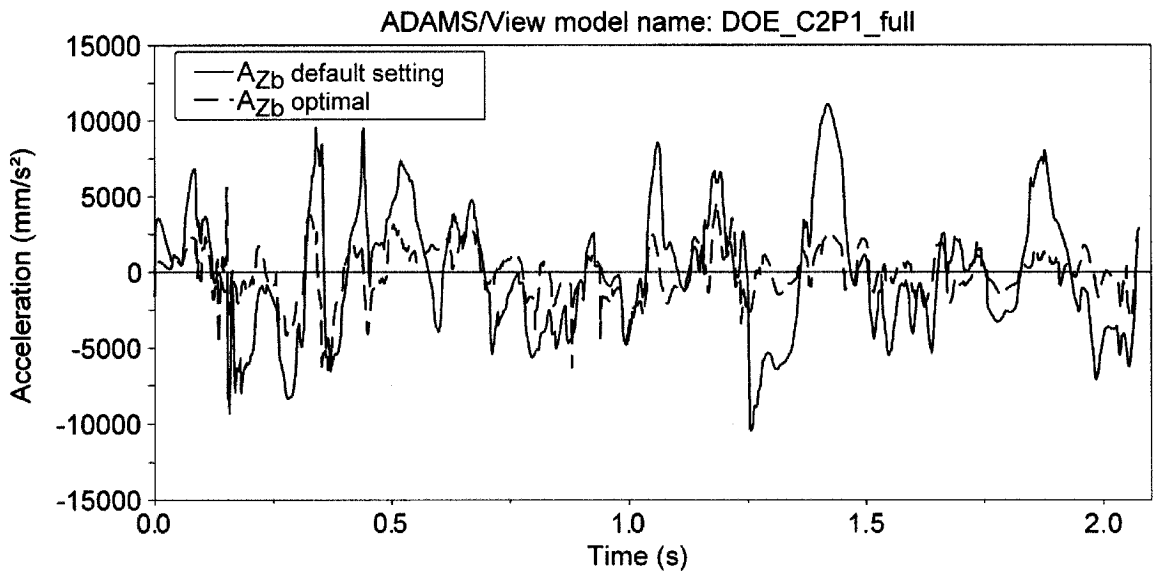

Figure 5.9: Comparison of optimal A_{Zb} response with the reference response.

5.4 Summary

The response surface methodology (RSM) is employed to identify near optimal values of several design parameters of the vehicle. The rms value of the driver's buttock acceleration along the vehicle's frame vertical axis is used as the basic comfort metric, thus becoming the response variable to be minimized. Using a typical RSM procedure, three consecutive phases are performed with the goal of identifying an optimal combination of parameter values. Phase 0 consisted in the screening of the nine potentially influencing parameters, leading to the retention of five on the basis of the sensitivity analyses using 4 different methods of interpreting the results. In Phase 1, four successive sequences of the steepest descent method indicated that a region of optimum response does not exist for the problem at hand, since some of the factors display asymptotic behavior. However, when imposing realizable values on three of the parameters, analysis of accumulated data and common suspension system theory led to the conclusion that the remaining two parameters should have an optimum region. Phase

2 was therefore undertaken to try to isolate an optimum point in the region of low response. Three different experiments, of three different design types, were then performed leading to the final conclusion that the system does have a relatively broad optimum region but no uniquely identifiable optimum point. The process further revealed that the system's complex non-linear nature leads to small yet significant and hard-to-predict response variations triggered by relatively small parameter changes. The model is thus considered to exhibit more than sufficient sensitivity to enable effective use of RSM for optimization of various aspects of its dynamic response, leading at least to the identification of an optimum region if not always a unique optimum point.

CHAPTER 6

CONCLUSION AND RECOMMENDATIONS FOR FUTURE WORK

6.1 Major Highlights of this Investigation

Very few studies have been devoted to snowmobile dynamics, the last dating back to 1994. This dissertation research shares their primary goal, which in essence is to develop a snowmobile simulation model that vehicle dynamics engineers will embrace as a comprehensive and efficient design and analysis tool. An augmented model architecture was formulated along with a measurement protocol to fully characterize the dynamic response behavior of a prototype snowmobile developed by BRP. Actual construction of the model was then followed by its validation and application to study the ride vibration environment. The major highlights of this dissertation work are briefly summarized below.

1. A comprehensive multi-body dynamic model of the snowmobile is developed. The adopted model structure has 9 degrees of freedom, being the frame longitudinal, vertical and pitch motion, the front suspension deflection and ski pitch, the track guiding rail bounce and pitch, the driver bounce and the drive axle rotation.

2. Four different trail segments, covering the range of trail types typically encountered, were profiled using a purposely developed technique based on recording the ski's pitch velocity and longitudinal acceleration, while travelling at low speeds. Additional low-resolution manual measurements allowed for compensating for the drifts of the processed high-resolution signals. One segment was a single discrete bump on which the snowmobile jumped, entirely leaving the ground before landing, skis first. The other segments ranged from high speed and low amplitude "ripple" bumps to low speed and high amplitude "moguls". Elevation signals directly allowed for rebuilding the trail segments in the simulator, while extracting their spatial PSD's resulted in a first roughness

characterization of the snowmobile trails to be used in eventual random excitation simulations.

3. Response characteristics of the vehicle-driver system traversing each trail segment were recorded. Starting from rest, the driver quickly accelerated to the velocity typical of each trail type and tried to maintain it up to the braking zone. Three passes were recorded on each segment. All quantities required to fully determine the vehicle response were recorded except for the ski pitch angle, as this was judged unnecessary. Recordings of the frame vertical and longitudinal accelerations, along its local axes, as well as pitch velocity allowed for computing the vehicle velocity, position and pitch attitude over the trail. In order to gain a better qualitative understanding of the system responses, all the acquired signals were analysed in the time domain and the frame signals were also analyzed in the frequency domain.

4. A non-linear model of the total vehicle was implemented in the ADAMS software. All suspension components, parts of the drivetrain and a "lumped" frame representation were assembled as a set of rigid bodies connected by joints of various types, in order to reproduce the real vehicle topology. The effects of the track, especially the important coupling of rear suspension motion to drive-torque, were included by applying external forces to the rail, the frame and the drive axle. A simple and efficient model of the track was developed by treating the belt as eight different spans, which permitted for computation of the forces magnitude by applying D'Alembert's principle to each span. Combining the field recordings and rear suspension sub-model allowed for computing the ground normal load, enabling the construction of the first quasi-steady model of snowmobile propulsive force as a function of the track slip ratio and normal load. A simple driver representation was realized by linking a rigid torso to articulated limbs themselves attached to the handlebar and the foot wells. The torso sits on a non-linear spring and damper element with characteristics identified from laboratory tests of the production seats. The snow covered trails are represented as rigid bodies, their top surface being identical to the field-measured trail profiles. Non-linear stiffness and damping contact elements link them to skis and rail, achieving a realistic deformable snow behavior.

5. An extensive model validation effort was undertaken by comparing the static and dynamic responses of the model with the measured data in the time as well as frequency domains. Frame signals were treated separately from the suspension deflections. The undamped fundamental bounce and pitch frequencies of the model were also looked at prior to the investigation of its forced transmissibility responses.

6. As a first practical application of the full simulator, a parametric analysis was performed to identify the parameters effectively influencing the driver comfort and to try to identify their optimum values. This is carried out using the response surface methodology with the response variable being the driver's buttock vertical rms acceleration over the test run. Phase 0 screened the 9 parameters expected to

have some influence on the response. The results revealed that a total of 5 parameters have a significant influence on the response. The Phase 1 analyses led to the identification of a region of optimum response, while providing further insights into the system's behaviour. Phase 2 failed to reveal a unique optimum point but indicated more clearly the values past which suspension bottoming starts to occur.

6.2 Conclusions

In view of the analysis and experimentations detailed in this dissertation, the overall objective of this project can be considered achieved to an extent since it resulted in a reasonably accurate, efficient, user-friendly and easy to modify snowmobile simulation model amenable to routinely serve as a design and analysis tool. The following is a list of the other major conclusions reached throughout the course of this project:

1. In order to be accepted by designers as a valid tool, a snowmobile simulator must be reasonably validated and demonstrate good accuracy, be easy to use and efficient, and include a representative track model and deformable ground contact characteristics.

2. As modern snowmobiles experience large transient motion, the model must be able to simulate the transient response by considering track angular degree of freedom, and coupling between the drive-axle torque and rear suspension motion.

3. Trail profile measurement must be carried out using a dedicated set-up with its instrumented apparatus placed as close to ground excitation as possible. This is evidenced by comparing the average to very good results obtained from the instrumented ski recording with the totally erroneous results obtained from the frame instrumentation recordings.

4. Snowmobiles encounter a large range of trail roughness, about half as large as the difference between that of smooth roads and pasture fields. Moreover, at frequencies above 0.25 cycle/m, the snow trails energy content falls much faster than that of a typical dry road.

5. The direction and magnitude of longitudinal acceleration of the vehicle strongly affects the frequency content of the bounce and pitch responses, and tends to shift the PSD peaks on the frequency axis. An effective vehicle model therefore must consider the coupling between the longitudinal and vertical dynamics.

6. Although assuming infinite track tangential stiffness considerably simplifies the track model, making it faster to solve, it forces an approximation to be included in its development and thus prevents modelling the track's radial dynamics.

7. As slip ratio increases to very high positive values (>7) the propulsive force abruptly falls to lower values. Therefore, with its current traction model, the simulation cannot reproduce gross slip under hard accelerations.

8. The current deformable ground representation, although of a different nature than the traditional "plastic soil" ground models, provides reasonable to good agreements between the model responses and the measured data while being stable and computationally efficient.

9. The model displays reasonable agreements with the prototype data in view of the static as well as dynamic responses over medium roughness trail and over trails comprising discrete events. Relatively poor agreements are obtained over rough and low-speed trails.

10. Due to erroneous surface profile rebuilding, it is impossible to draw a definite conclusion on the dynamic response agreement over high-speed smooth trail profiles.

11. In free oscillation around its static equilibrium point, the model, with all damping removed and driver fixed to frame, displays good agreement with the natural frequencies of an equivalent 2-DOF linear model. The agreements in view of the mode shapes and coordinates of the pitch center, however, were judged to be poor. This discrepancy is attributed to the non-linear nature of the full model.

12. Responses to forced excitation revealed good agreements in terms of natural frequencies of the frame bounce and pitch, and driver bounce between the full model and a damped 3-DOF linear model. However, it also revealed an erratic behavior of the ground contact algorithm inducing sudden low amplitude ground penetration variations resulting in unexpected peaks at relatively high frequency in the transmissibility plots.

13. Performing a parametric analysis proved to be a viable, robust, stable and sufficiently fast method to gain further insight in the system behaviour and to identify critical values optimizing a response variable of interest. In this case, it allowed for identification of a group of parameter values minimizing driver buttock acceleration, while revealing the high sensitivity of the model.

14. Given the high sensitivity of the model, the probability of identifying a clear unique set of parameter values optimizing a given response variable while being usable in practice is low. In order to increase that probability, the test event (a single simulated maneuver or sequence of different maneuvers) should cover the full range of operating conditions. Particular attention should also be paid to the relative importance of each different operating condition among the test event.

6.3 Recommendations for Future Work

Given its current level of agreement to physical experiments, the model is considered sufficient for early prospective design work, dealing with significantly different competing designs, but needs further refinements to reach the accuracy level required for evaluation of small modifications and fine analysis. Performing the following work should produce most of the needed improvements:

1. Expanding the snowmobile trail profiles library will require that profiling instrumentation and algorithm be enhanced to eliminate drift altogether, fully automate profile rebuilding and eliminate the need for manual measurements. Algorithm improvements ought to be ported to vehicle motion rebuilding as this would result in net improvements in agreements between the model and prototype responses.

2. Vehicle instrumentation needs to be improved, particularly by using a threshold-free drive-axle speed sensor and by having an anti-aliasing filter on every sensor.

3. The vehicle bounce, pitch and driver bounce resonance frequencies would need to be measured through forced excitation in laboratory using hydraulic actuators.

4. Suspension hysteresis needs to be quantified, through a purposely-developed experiment, and integrated in the model.

5. Relaxing the assumption of track infinite tangential stiffness would allow for modelling the track radial dynamics, while staying far from the complexities of a chain-type track model.

6. Both traction and ground deformation models require additional dedicated experiments to characterize different types of snow and, in the first case, to get better raw data over larger normal load and slip ratio ranges.

7. Apparent ski and track friction on snow as well as track friction on rail should be quantified and modeled to improve the longitudinal behaviour agreement between the model and the prototype. The track's rotation hysteresis also needs to be investigated.

REFERENCES

1. Rehn, B., Nilsson, T., Olofsson, B., Lundström, R., *Whole-Body Vibration Exposure and Non-neutral Postures During Occupational Use of All-terrain Vehicles*, in Annals of Occupational Hygiene, 2005, Vol. 49, No. 3, pp. 267-275, Oxford University Press

2. Anttonen, H., Niskanen, J., *Whole body vibration and the snowmobile,* Arctic Med Res. 1994; Vol. 53, Suppl 3:24-8

3. Anttonen, H., Virokannas, H., *Hand-arm vibration in snowmobile drivers*, Arctic Med res. 1994; Vol. 53, Suppl 3: 19-23

4. Rauh, J., *Virtual Development of Ride and Handling Characteristics for Advanced Passenger Cars*, in Vehicle System Dynamics, 2003, Vol.40, Nos. 1-3, pp.135-155

5. Newman, J. A., Cheng, S.-C., Suri, V. K., *Hybrid Computer Simulation of the Recreational Snowmobile*, SAE Paper 720261, Society of Automotive Engineers, New York, NY, USA, 1972

6. Newman, J.A., and Beale, D.J., *The Snowmobile Suspension System – A High-Speed Motion Picture Study.*, SAE Paper 710667, Society of Automotive Engineers, New York, NY, USA, 1971

7. Prasad, K. K., *A Study of Snowmobile Drive Systems*, SAE papers 730782, Society of Automotive Engineers, New York, NY, USA, 1973

8. Haines, W. M., *New Approach to Positive Drive Snowmobile Tracks*, SAE paper 710231, Society of Automotive Engineers, New York, NY, USA, 1971

9. Kho, J. K. H., Newman, J. A., *Braking Characteristics of the Recreational Snowmobile*, SAE paper 730783, Society of Automotive Engineers, New York, NY, USA, 1973

10. Hollnagel, H. E., *Snowmobile Ski Suspensions*, SAE paper 740677, Society of Automotive Engineers, Warendale, PA, USA, 1974

11. Cline, R. C., *Shock Absorbers: An Integral Part of Recreational Vehicle Developments*, SAE paper 740678, Society of Automotive Engineers, New York, NY, USA, 1974

12. Alanoly, J, *Computerized Analysis and Design of Vehicle Multi-Body Systems*, Ph.D. thesis, Dept. of Mech. Eng., Concordia University, Montreal, Quebec, Canada, 1989

13. Sankar, S., Alanoly, J., Germain, D., Malette, B., *Snowmobile Suspension System Design Under University-Industry Collaboration*, SAE paper 890026, Society of Automotive Engineers, Warrendale, PA, 1989

14. Khan, Mustapha, *Logiciel de simulation dynamique de véhicules récréatif à chenilles. (Rapport Final)*, Département de génie mécanique, Université de Sherbrooke, Shebrooke, Quebec, Canada, 1994

15. *Working Model Helps Scorpion Snowmobiles Regain Its Sting*, MSC. Software 2005, 14 March 2005, <http://www.workingmodel.com/vn4d/success/ss_scorpion.html>.

16. Dhir, A., *Ride Dynamics of High Mobility Wheeled/Tracked Off-Road Vehicles: Computer Simulation with Field Validation*, Ph.D. thesis, Dept. of Mech. Eng., Concordia University, Montreal, Quebec, Canada, 1993

17. Sandu, C., *Tracked Vehicle Modeling*, Ph.D. thesis, Graduate College, The University of Iowa, Iowa City, Iowa, USA, 2000

18. Bekker, M.G., *Introduction to Terrain-Vehicle Systems*, The University of Michigan Press, Ann Arbor, MI, USA, 1969

19. Wong, J.Y., *Theory of Ground Vehicles*, 3rd. ed., John Wiley & Sons, 2001

20. Wong. J.Y., *Terramechanics and Off-Road Vehicles*, Elsevier, 1989

21. Bogdanoff, J.L., Kozin, F, Cote, L.J., *Atlas of Off-Road Ground Roughness P.S.D..s and Report on Data Acquisition Technique*, U.S. Army Tank Automotive Center, Report No. 9387 (LL 109), Warren, MI, USA, 1966

22. Mimuro, T., Maemura, T., Fujii, H., *Development and Application of the Road Profile Measuring System*, SAE paper 930257, Society of Automotive Engineers, Warrendale, PA, 1993

23. Laib, L., Analysis of the Vibration-Excitation Effect Caused by Deformable Soil Surfaces, in *Journal of Terramechanics*, Vol. 32, No. 3. pp.151-163, 1995

24. Ashmore, S.C., Hodges, H.C.,Jr., *Dynamic Force Measurement Vehicle (DFMV) and Its Application to Measuring end Monitoring Road Roughness*, Vehicle, Tire, Pavement Interface, ASTM STP 1164, J.J. Henry and J.C. Wambold, Eds., American Society of Testing and Materials, Philadelphia, 1992, pp.69-96

25. Rakheja, S., Wang, K., Bhat, R., Boileau, P.-É. 'Enhancement of ride vibration environment of tracked sidewalk snowplows', Int. J. of Vehicle Design, Vol. 30, No. 3, 2002

26. Shabana, A.A., *Computational Dynamics, Second Edition*, John Wiley & Sons, 2001

27. Ma, Z.D, Perkins, N.C., *A Track-Wheel-Terrain Interaction Model for Dynamic Simulation of Tracked Vehicles*, in Vehicle Systems Dynamics, 2002, Vol. 37, No. 6, pp. 401-421

28. Schanhals, L.R., Pershings, R.L., *Performance Testing and Criteria for Snowmobile Seat Cushions*, SAE paper 730770, Society of Automotive Engineers, New York, NY, USA, 1973

29. Bastow, D., Howard, G., Whitehead, J. P., *Car Suspension and Handling*, 4th edition, Society of Automotive Engineers, Warrendale, PA, USA, 2004

30. International Standard Organisation ISO 2631-1, *Mechanical Vibration and Shock-Evaluation of Human Exposure to Whole-Body Vibration*, Part 1: General Requirements, Second Edition, 1997, 30pp.

31. Els, P.S., The Applicability of Ride-Comfort Standards to Off-road Vehicles, in *Journal of Terramechanics*, vol. 42, 2005, pp.47-64

32. British Standard Guide to measurement and evaluation of human exposure to whole body mechanical vibration and repeated shock, BS 6841. British Standard Institution, 1987

33. Human exposure to mechanical vibrations whole-body vibration, Verein Deutcher Ingenieure, VDI 2057, September 2002

34. Pradko, F., Lee, RA, *Vibration comfort criteria*, SAE Technical Paper 660139, Society of Automotive Engineers, Warrendale, PA, USA, 1966

35. Tang, Tingsheng, *A Study of Ride Comfort Performance of Occupant on Car Seat Exposed to Whole-Body Vibration*, M.A.Sc. thesis, Dept. of Mech. Eng., Concordia University, Montreal, Quebec, Canada, 2002

36. Bombardier Inc., Ski-Doo promotional catalog 2004, part no. 484 800 085, Bombardier Inc., Canada, 2003

37. Personal communication with René Lemieux, engineer at BRP.

38. Kreysig, E., *Advanced Engineering Mathematics, Seventh Edition*, John Wiley & Sons, USA, 1993

39. *Matlab Help*, in Matlab 6.5 realease 13, The MathWorks Inc., MA, USA, 2002

40. Bombardier Recreation Products Inc. internal report on polyurethane seat characteristics, 2003

41. Thomson, W.T., Dahleh, M.D., *Theory of Vibration with Applications, Fifth Edition*, Prentice Hall, 1993

42. Pacejka, H. B., *Tire and Vehicle Dynamics*, Society of Automotive Engineers, Warrendale, PA, USA, 2002

43. MSC Software Corp., *ADAMS/Tire Help, Tire Models*, MSC Software Corp., 2004

44. MSC Software Corp., *ADAMS/Solver Help, Contact Statement*, MSC Software Corp., 2004

45. Negrut, D., Dyer, A., *ADAMS/Solver Primer*, Ann Arbor, MI, USA, 2004

46. Wells, D. A., *Theory and Problems of Lagrangian Dynamics*, Schaum's Outline, McGraw Hill, USA, 1967

47. Milliken, W.F., Milliken, D., *Chassis Design Principles and Analysis*, Society of Automotive Engineers, Warrendale, PA, USA, 2002

48. Myers, R.H., Montgomery, D.C., Response Surface Methodology, Process and Product Optimization Using Designed Experiments, Second Edition, John Wiley & Sons, 2002

49. Hines, W.W., Montgomery, D.C., *Probability and Statistics in Engineering and Management Science, Third Edition*, John Wiley & Sons, 1990